The amplitude and the phase or: Measuring directional and random motion with optical coherence tomography

The work described in this thesis was carried out in the department of *Biomedical Engineering and Physics* at the *Academic Medical Center* of the *University of Amsterdam*, in Amsterdam, the Netherlands. This work was financially supported by the IOP Photonic Devices program.

Printing: Off Page
ISBN: 978-94-6182-737-1

The amplitude and the phase or: Measuring directional and random motion with optical coherence tomography

ACADEMISCH PROEFSCHRIFT

ter verkrijging van de graad van doctor
aan de Universiteit van Amsterdam
op gezag van de Rector Magnificus
prof. dr. ir. K.I.J. Maex
ten overstaan van een door het College van Promoties ingestelde commissie,
in het openbaar te verdedigen in de Agnietenkapel
op dinsdag 29 november 2016, te 12:00 uur

door

Nicolas Mauricio Weiss

geboren te Montevideo, Uruguay

Promotiecommissie

Promotor:	
prof. dr. A.G.J.M. van Leeuwen	Universiteit van Amsterdam
Co-promotor:	
dr. J. Kalkman	Technische Universiteit Delft
Overige leden:	
prof. dr. ir. M.J.C. van Gemert	Universiteit van Amsterdam
prof. dr. J.M. ten Cate	Universiteit van Amsterdam
dr. R. Sprik	Universiteit van Amsterdam
prof. dr. D. Iannuzzi	Vrije Universiteit Amsterdam
prof. dr. G.W. 't Hooft	Universiteit Leiden

Faculteit der Geneeskunde

Table of contents

CHAPTER 1

General introduction

This general introduction discusses the technical background of this thesis and the interrelations between the chapters.

A note to the reader: this thesis should be regarded as a bundle of in peer-reviewed published and (yet) unpublished scientific material. In principle, every chapter in this thesis is self-contained and can be read independently from the rest.

A time-dependent complex-valued scalar signal $s(t)$ in its most general form can be written as the product of an amplitude term $A(t)$ and a phase term $\phi(t)$ as:

$$s(t) = A(t)e^{j\phi(t)} \ ,$$

where t is time and $j = \sqrt{-1}$ is the imaginary unit[1]. Interferometric signals, such as the signal measured by optical coherence tomography (OCT) can be described by the above mentioned mathematical relationship. Typically, OCT uses a low-coherence light source and a Michelson interferometer to measure path-length resolved backscatter profiles of samples with micrometer resolution and up to a few millimeters long [1]. A schematic of a basic OCT imaging geometry is shown in Fig. 1.1. Light from the low-coherence source is directed towards a reference mirror and a sample via a beam splitter. After reflection and scattering from the mirror and sample, respectively, light is recombined via de beam splitter in a detector. The measured interferometric signal is then further processed by a computer.

Two realizations of OCT exist: time-domain OCT and Fourier-domain OCT. In time-domain OCT the low-coherence interferometric signal is detected with a single photo-diode and the path-length resolved information of the scattering sample is obtained by scanning the reference arm of the interferometer. In Fourier-domain OCT, as the name already indicates, the path-length information is encoded in the spectrum of the interferometric signal. The OCT signal is calculated by means of a Fourier-transform of the interferometric signal, such that, the conjugate variables become wave-number and optical path-length. Two implementations are widely used: spectral-domain OCT and swept-source OCT. In both cases, the reference arm mirror is static and the path-length resolution is achieved by either spectrally resolving the interferometric signal with a diffraction grating (spectral-domain) or by spectrally resolving the interferometric signal in time using a wavelength swept laser (swept-source). Fourier-domain OCT has a signal-to-noise ratio advantage when compared to time-domain OCT and has therefore experienced wider application [2, 3]. In this thesis we will use the term OCT loosely and will refer, unless stated otherwise, to the swept-source OCT configuration.

[1] Electrical engineers, such as the author, use j to represent the imaginary unit, since i is usually reserved to denote current. It is left to the physicist readers to replace j by i, wherever they see fit.

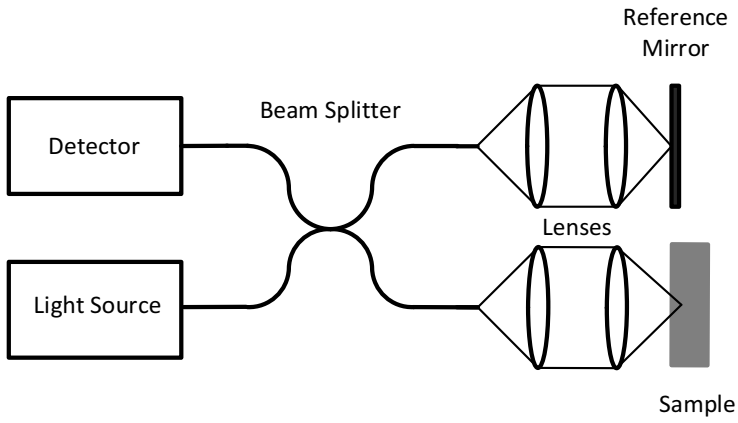

Figure 1.1: Schematic of a basic OCT measuring configuration.

The OCT amplitude $A(t)$ is typically used to generate images of the sample. An example of an OCT image of the author's thumb is shown in Fig. 1.2. Additionally, the amplitude and the phase of the OCT signal can be used to extract quantitative sample information. For example, the OCT amplitude has been used to measure static sample parameters such as layer thickness [4], refractive index [5], birefringence [6], scattering and absorption coefficients [7], and scattering anisotropy [8]. In the case of a dynamic sample, the fluctuations of $A(t)$ can be used to measure flow [9] and diffusion [10]. In the medical field, OCT has been applied, e.g., to measure blood flow in the retina [11] and to visualize tumors [12].

The phase of the OCT signal $\phi(t)$ of static samples can be used to measure layer thickness and refractive index with improved resolution when compared to using the OCT amplitude [13]. Most notably, in the case of dynamic samples, the OCT phase carries information about the Doppler shift which is directly proportional to the scatters velocity component in the propagation direction of the imaging beam [14, 15].

The emphasis of this thesis lies in exploiting the information carried by the time-dependent OCT amplitude and phase to measure the directional and random motion of a sample. One way of quantifying the rate of change of the signal $s(t)$ is by calculating its autocorrelation function [16]:

$$g(\tau) = \int_{-\infty}^{\infty} s(t+\tau)s^*(t)\,\mathrm{d}t \ ,$$

where τ is the time-lag of the autocorrelation function and * denotes the complex-conjugate operation. The autocorrelation function quantifies the resemblance of a signal with a time shifted copy from itself. Basically, each value of the autocorrelation function is calculated as a summation over t of products of the signal $s(t)$ with a time-shifted version of itself $s(t+\tau)$. For non-periodic signals, the autocorrelation function $g(\tau)$ will decrease in amplitude for increasing values of τ [17]. An example

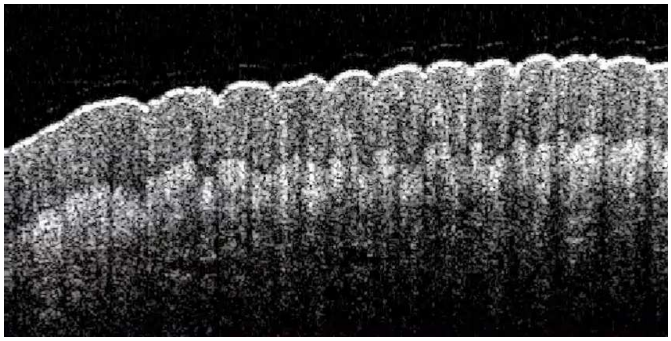

Figure 1.2: Two-dimensional image of the OCT amplitude of data from the author's thumb where the fingerprint ridges, the dermis, and the epidermis can be clearly seen.

of the variations of the OCT amplitude and its autocovariance[2] function is shown in Fig. 1.3 for a suspension of flowing polystyrene spheres. Figure 1.3(b) shows a faster decay rate for the black signal when compared to the red signal. The autocorrelation function for the red signal at a particular time point is larger than the autocorrelation function for the black signal. In this particular case, the measured amplitude fluctuations originate from the sample dynamics (flow and diffusion) inside the OCT imaging volume and measurement noise. The relation between the decay rate of the autocorrelation function and the sample dynamics will be treated later in this thesis.

Scope of this thesis

In this thesis we report on the development, validation, and application of a model based on the OCT autocorrelation function to extract information about the dynamic parameters of a sample from the time fluctuations of the OCT amplitude and phase. The work presented in this thesis, first, extends the understanding of dynamic fluctuations on the OCT amplitude and phase; and second, it opens up new opportunities and applications of OCT for the study of a range of rheological properties in complex dynamic geometries.

Outline of this thesis

The outline of the thesis is as follows: in Chapter 2 we report on a model for the measurement of flow and diffusion based on the OCT autocorrelation function. The model is validated with a simple flow system and shows that both the longitudinal and the transverse flow velocity components can be accurately measured at micrometer scale and in a single measurement. In Chapter 3 the results of the previous chapter are extended for the simultaneous measurement of flow and diffusion. We

[2]The difference between the autocovariance and the autocorrelation here is the subtraction of the mean of the signal $\int_{-\infty}^{\infty} (s(t+\tau)-\mu)(s^*(t)-\mu^*)\,\mathrm{d}t$, with μ the mean.

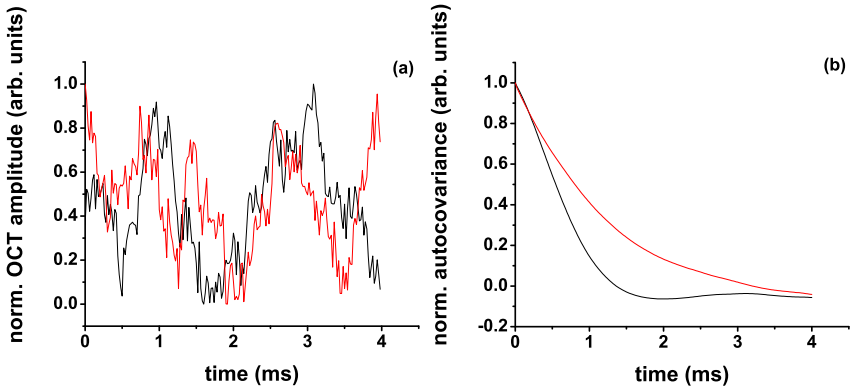

Figure 1.3: (a) Normalized OCT amplitude for a suspension of polystyrene spheres flowing at two different velocities; and (b) the corresponding autocovariance functions.

also report on the limitations of the model with respect to the accuracy and precision of the individually estimated dynamical parameters. Most interestingly, we show experimentally that the decay of the Gaussian transverse flow term in the OCT autocorrelation function depends only on the beam radius at the focus and not on the local Gaussian beam radius. Based on the understanding gathered in the previous two chapters, we present three applications. First, in Chapter 4 we apply the OCT autocorrelation analysis to the measurement of biofilm growth and local flow velocities in a microfludic channel. Second, in Chapter 5 we report on a method to correct for non-uniform lateral scanning of a sample in OCT. We show that based solely on the information carried by the phase of the OCT signal, the non-uniform trajectory of a sample can be reconstructed. We also demonstrate centimeters-long hand-held OCT imaging of the skin of the forearm. And third, in Chapter 6 we report on a method to measure the height profile of non-scattering soft (biological) samples in liquid environments using a combination of optical tweezers and OCT. We achieve this by using the phase of the OCT signal to measure the sub-micrometer displacements of an optically trapped sphere. Finally, in Chapter 7 we present the conclusions and in Chapter 8 we discuss possible future research directions.

In the Appendices of this thesis a collection of material is presented that deviates somewhat from the contents presented in the previous chapters[3]. In Appendices A-C we present three approaches to achieve a broader spectrum of applications of OCT by reducing the form factor and cost of OCT systems based on integrated optics. We designed, fabricated, and characterized an integrated-optics-based swept-source optical coherence tomography system in TriPleX, silicon, and silicon oxynitride technologies. An external 1300 nm swept source is coupled to the chip, which contains waveguide structures for interferometric path-length ranging. In all three technologies, we demonstrate cross-sectional OCT imaging of a multilayered tissue phantom.

[3]The results presented in the Appendices were obtained using the swept-source OCT system build by the author that was used in all the other chapters of this thesis.

CHAPTER 2

Localized measurement of longitudinal and transverse flow velocities in colloidal suspensions using optical coherence tomography

Abstract

We report on localized measurement of the longitudinal and transverse flow velocities in a colloidal suspension using optical coherence tomography. We present a model for the path-length resolved autocorrelation function including diffusion and flow, which we experimentally verify. For flow that is not perpendicular to the incident beam, the longitudinal velocity gradient over the coherence gate causes additional decorrelation, which is described by our model. We demonstrate simultaneous imaging of sample morphology and longitudinal and transverse flow at micrometer scale in a single measurement.

This chapter has been published as:

- N. Weiss, T.G. van Leeuwen, and J. Kalkman, "Localized measurement of longitudinal and transverse flow velocities in colloidal suspensions using optical coherence tomography," Phys. Rev. E **88**, 042312 (2013).

2.1 Introduction

Modern experiments to study mass transport phenomena in complex rheological systems such as microfluidics [18], polymer solutions [19], biofilms [20], blood microcirculation [21], and blood [22, 23] demand spatially and time resolved probing of concentration fields, pressure gradients, velocity profiles, wall shear stress, and diffusion coefficients. Optical techniques to measure fluid flow velocity are interesting because of their non-contact operation and high spatiotemporal resolution. Typically, optical techniques use a (coherent) light source to illuminate the sample and detect the fluctuations of the scattered light. Among conventionally used optical techniques are laser Doppler flowmetry (LDF) [24], laser speckle velocimetry (LSV) [25], and particle image velocimetry (PIV) [26]. In LDF, scattered light interferes with a local oscillator and the intensity fluctuations of the detected light are related to the Doppler shift generated by flow in the sample. In LSV, the velocity of the scatterers is quantified by the intensity fluctuations that originate from the movement of the scatterers through the probing field. In PIV, the flow velocity is estimated by tracking the position over time of tracer particles present in the fluid. In LDF, LSV, and PIV the exact path-length distribution of the scattered light is unknown, making it impossible to quantify the velocity distribution deep inside the sample, thereby providing only volumetrically averaged information of the sample dynamics.

Optical coherence tomography (OCT) is an imaging technique in which low coherence interferometry is used to produce path-length resolved complex-valued backscatter profiles of (biological) samples up to a few millimeters deep [1]. In OCT, the transverse and longitudinal localization accuracy is given by the focusing optics and by the coherence of the light source, respectively. Functional extensions of OCT allow for localized measurements of static properties, such as, layer thickness [4], birefringence [6], scattering and absorption coefficients [7], and scattering anisotropy [8], as well as sample dynamics, such as, longitudinal flow [14] and particle diffusion [10, 27]. Various studies have demonstrated that OCT can accurately determine the longitudinal component of the local flow velocity [28, 29]. Determination of the transverse flow velocity has been pursued by analyzing the spectral bandwidth of the Doppler frequency shift [30, 31, 32], by using two distinct wave vectors for the incident light [33], by an autocorrelation method [34], by extracting the Doppler angle from the sample morphology [35], and by dynamic light scattering [36]. However, up till now no accurate quantification of the local transverse flow has been achieved.

In this manuscript, we present a theory for the path-length resolved OCT signal and its normalized autocorrelation function for the case of arbitrarily oriented flow in the presence of diffusion. We validate the theory by measuring the transverse and longitudinal flow velocities locally in a colloidal suspension. We show that, sample morphology and flow velocity are determined simultaneously with high spatiotemporal resolution.

2.2 Model for the normalized autocorrelation of the OCT signal

We start by writing the signal at the detector following Ref. [37] as:

$$i(t) = \gamma\sqrt{P_r(t)P_s(t)}\mathrm{Re}\iiint_{-\infty}^{\infty} r(x-x_s, y-y_s, z-z_s) \\ h(x,y)e^{-j2k(t)z}\mathrm{d}x\,\mathrm{d}y\,\mathrm{d}z\ , \tag{2.1}$$

with γ the photon-to-electron conversion efficiency, $P_r(t)$ the reference arm power, $P_s(t)$ the maximum sample arm power, Re the real-part operator, $r(x,y,z)$ the backscattering amplitude of the sample, (x_s, y_s, z_s) the position of the scattering sample, $h(x,y)$ the profile of the transverse illuminating beam, and $k(t) = k_0 + k_1 t$ the time dependent wavenumber, with $k = 2\pi/\lambda$, $t \in [-T/2, T/2]$, with T the period of the swept laser. We assume that the characteristic time constant of the scattering dynamics is sufficiently smaller than T.

The transverse illuminating beam is assumed to be Gaussian:

$$h(x,y) = e^{-2\frac{x^2}{w_x^2}}e^{-2\frac{y^2}{w_y^2}}\ , \tag{2.2}$$

where w_x and w_y are the beam radii as the (1/e)-radius of the field and the factor of 2 in the exponent accounts for the coupling efficiency of a single-mode fiber [38]. Note that the effect of the longitudinal confocal gate is neglected, since for Fourier domain OCT systems the Rayleigh length is in general much larger than the coherence length (280 µm vs 8.1 µm for the swept-source OCT system used here).

By inverse Fourier transforming Eq. (2.1) and assuming a Gaussian spectral envelope, the OCT signal $a_{OCT}(\hat{z}, t)$ is written as [37]:

$$a_{OCT}(\hat{z}, t) \approx \iiint_{-\infty}^{\infty} r(x-x_s, y-y_s, z-z_s) \\ h(x,y)e^{-j2k_0 z}e^{-\frac{(\hat{z}-z)^2}{w_z^2}}\mathrm{d}x\,\mathrm{d}y\,\mathrm{d}z\ , \tag{2.3}$$

where w_z is the waist ((1/e)-radius) of the coherence function.

For simplicity we restrict the analysis to the (x,z) plane. Assuming that the reflection r consists of N point scatterers Eq. (2.3) is written as:

$$a_{OCT}(\hat{z}, t) \approx \iint_{-\infty}^{\infty}\sum_{\nu=1}^{N}\delta(x-x_\nu)\delta(z-z_\nu) \\ h(x)e^{-j2k_0 z}e^{-\frac{(\hat{z}-z)^2}{w_z^2}}\mathrm{d}x\,\mathrm{d}z\ , \tag{2.4}$$

with N the total number of scatterers in the probed volume and (x_ν, x_ν) the position of the ν-th scatterer. Now, solving the integrals we write the OCT signal as:

$$a_{OCT}(\hat{z}, t) \approx \sum_{\nu=1}^{N} e^{-2\frac{x_\nu^2}{w_x^2}}e^{-j2k_0 z_\nu}e^{-\frac{(\hat{z}-z_\nu)^2}{w_z^2}}\ . \tag{2.5}$$

Assuming stationarity, we write the normalized autocorrelation function as:

$$g(\hat{z},\tau) =< a_{OCT}(\hat{z},\tau)a^{*}_{OCT}(\hat{z},0) > , \tag{2.6}$$

where * indicates the complex-conjugate operation and the brackets an ensemble average.

For the application described here we write the position of the scatterers as a summation of a diffusive and a directional component [39]:

$$\begin{aligned} x_\nu(\tau) &= x'_\nu(\tau) + v_x\tau\,, \\ z_\nu(\tau) &= z'_\nu(\tau) + v_z\tau\,. \end{aligned} \tag{2.7}$$

Assuming the diffusive motion to be independent of the initial position of the scatterers, we separate the ensemble average as the product of a diffusional and a translational average [39, 40]:

$$\begin{aligned} g(\hat{z},\tau) = \sum_{\nu,\xi=1}^{N} &< e^{-j2k_0(z'_\nu(\tau)-z'_\xi(0))} > \\ &< e^{-2\frac{(x'_\nu(\tau)+v_x\tau)^2}{w_x^2}} e^{-2\frac{x'_\xi(0)^2}{w_x^2}} e^{-j2k_0v_z\tau} \\ &\quad e^{-\frac{(\hat{z}-(z'_\nu(\tau)+v_z\tau))^2}{w_z^2}} e^{-\frac{(\hat{z}-z'_\xi(0))^2}{w_z^2}} > \ . \end{aligned} \tag{2.8}$$

Now, assuming that the scatterers are randomly placed throughout the scattering volume all terms with $\nu \neq \xi$ in Eq. (2.8) are zero, since the diffusive phase terms average out. Further, the sum can be dropped since all scatterers are assumed identical and all constant terms depending on N are dropped. The diffusional average is known [41] and has been measured by OCT in Ref. [10]:

$$< e^{-j2k_0(z'(\tau)-z'(0))} >= e^{-Dq^2\tau}\ ,\ \tau \geq 0\ , \tag{2.9}$$

where D is the diffusion coefficient given by the Stokes-Einstein equation $D = k_BT_K/6\pi\eta r$, with k_B Boltzmann's constant, T_K the absolute temperature, η the viscosity, and r the hydrodynamic particle radius. The absolute value of the scattering vector is $q = 4\pi n \sin(\alpha/2)/\lambda$, with n the refractive index of the medium, λ the wavelength in vacuum, and α the scattering angle. Generally, OCT is performed in backscattering with low numerical aperture objectives. Further, we assume no number fluctuations, independence of particle concentration, and single scattering.

The translational average can be computed as the average over the initial position of the scatterers [40]:

$$\begin{aligned} <& e^{-2\frac{(x'_\nu(\tau)+v_x\tau)^2}{w_x^2}} e^{-2\frac{x'_\nu(0)^2}{w_x^2}} e^{-j2k_0v_z\tau} e^{-\frac{(\hat{z}-(z'_\nu(\tau)+v_z\tau))^2}{w_z^2}} \\ & e^{-\frac{(\hat{z}-z'_\nu(0))^2}{w_z^2}} >= \\ & \iint_{-\infty}^{\infty} e^{-2\frac{(x+v_x\tau)^2}{w_x^2}} e^{-2\frac{x^2}{w_x^2}} e^{-j2k_0v_z\tau} \\ & \qquad e^{-\frac{(\hat{z}-(z+v_z\tau))^2}{w_z^2}} e^{-\frac{(\hat{z}-z)^2}{w_z^2}}\, \mathrm{d}x\, \mathrm{d}z\ , \end{aligned} \tag{2.10}$$

where we have neglected the influence of diffusion on the amplitude terms. The transverse contribution is similar to that known in speckle velocimetry [25] and is calculated as:

$$\int_{-\infty}^{\infty} e^{-2\frac{(x+v_x\tau)^2}{w_x^2}} e^{-2\frac{x^2}{w_x^2}} \,\mathrm{d}x = e^{-\frac{(v_x\tau)^2}{w_x^2}} \,, \tag{2.11}$$

where the spread of v_x over the coherence gate is neglected.

Finally, the normalized autocorrelation function of the complex valued OCT signal is written as:

$$\begin{aligned} g(\hat{z},\tau) =& e^{-Dq^2\tau} e^{-\frac{(v_x\tau)^2}{w_x^2}} \\ & \int_{-\infty}^{\infty} e^{-j2k_0 v_z\tau} e^{-\frac{(\hat{z}-(z+v_z\tau))^2}{w_z^2}} e^{-\frac{(\hat{z}-z)^2}{w_z^2}} \,\mathrm{d}z \;,\; \tau \geq 0 \;, \end{aligned} \tag{2.12}$$

where the exponential term describes the longitudinal diffusive dynamics, the Gaussian term in front of the integral describes the transverse directional dynamics, and the integral describes the longitudinal directional dynamics as a convolution of the Doppler phase term with the coherence detection gate. The normalization was taken with respect of $g(\hat{z},0)$. Note that this equation is similar to the one previously derived by Edwards et al. in the context of laser Doppler flowmetry [40]. The main difference here is that we have included the coherence detection gate in the derivation.

2.3 Materials and methods

2.3.1 Optical coherence tomography system

The experiments are performed with a home built fiber-based swept-source OCT system. The system operates at a center wavelength of 1312 nm with a bandwidth of 92 nm and a sweep frequency of 50 kHz (Axsun Technologies). The average output power is 20.9 mW and the duty cycle is 59.4%. Data is sampled (ATS9350, AlazarTech) with an interferometrically derived external clock signal at equidistant wavenumber intervals. To ensure phase stability each sweep is triggered by the signal of a fiber Bragg grating centered at 1266 nm (OE Land) [42]. The interferometric signal is detected with a 150 MHz balanced photodetector (PDB450C, Thorlabs) and a 80 MHz low-pass filter (VLF-80+, Mini-Circuits). The trigger signal is detected with a 125 MHz photodetector (1811, New Focus). The optics of the sample and reference arms are composed of a collimating lens (PAF-X-18-C, Thorlabs) and an achromatic doublet focusing lens (AC254-040-C, Thorlabs) with a numerical aperture of 0.04. The power ratio of the sample and reference arms is 90/10. We measured $w_x = 10.8 \pm 0.2$ µm and $w_z = 8.1 \pm 0.3$ µm in air with a mirror reflector. For our OCT set-up, the spread of q over the bandwidth is small, therefore we set $q = q_c$ at the center wavelength and $\alpha = 180°$ [10]. A schematic of the experimental set-up is shown in Fig. 2.1.

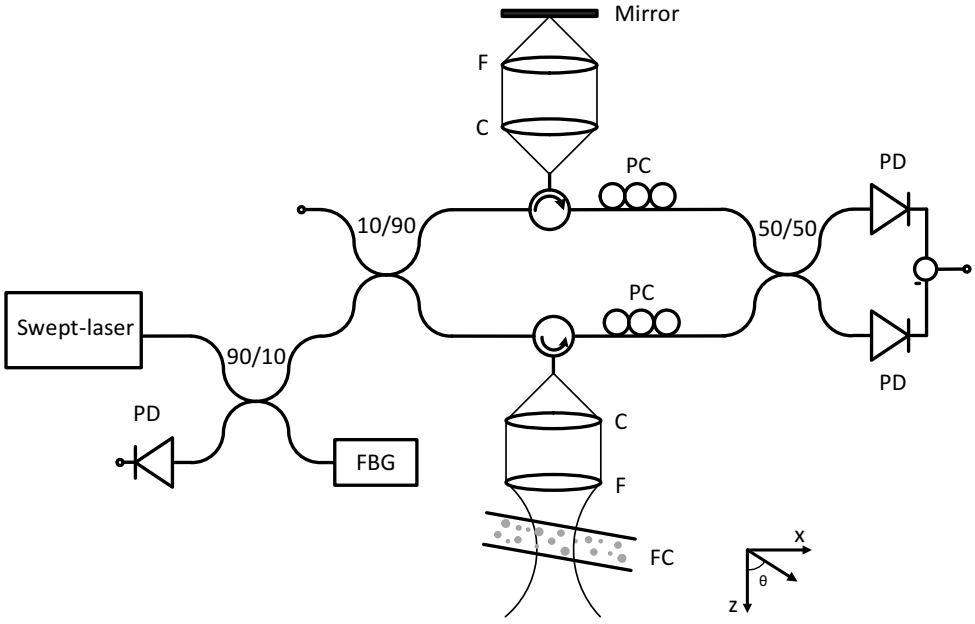

Figure 2.1: Schematic of the experimental swept-source OCT set-up. PD: photodetector, FBG: fiber Bragg grating, PC: polarization controllers, C: collimating lens, F: focusing lens, and FC: flow capillary. Gravity is in the z-direction.

Since the longitudinal decorrelation is determined by the coherence function of the light source, we measured it using a mirror reflector in air. The dots in Fig. 2.2 show the coherence gate of the swept light source measured by translating a mirror in the longitudinal direction mounted on a piezo-stage (M-664.164, Physik Instrumente) by steps of 1 μm. As can be seen, the coherence gate has asymmetric side lobes which is attributed to the non-Gaussian shape of the light source. The coherence gate was fitted as the sum of two Gaussian which are shown as the gray dashed lines in Fig. 2.2. The sum of the individual Gaussians is shown as the gray full line. Note that the formalism presented in Sec. 2.2 is not restricted to a Gaussian spectrum of the light source, where the Fourier transform in Eq. (2.1) can be taken with an arbitrary spectral shape.

2.3.2 Flow system

Flow is generated by gravity and directed through a cylindrical glass capillary with an inner diameter of 562 ± 25 μm. The flowing suspension consists of 1 vol. % Intralipid (Fresenius Kabi) dissolved in 74 vol. % distilled water and 25 vol. % glycerol (Acros Organics). The latter is used to reduce the Brownian motion of the particles in the suspension. The capillary is submerged in distilled water to reduce reflections from the outer glass walls. As a reference, the flow velocity is quantified

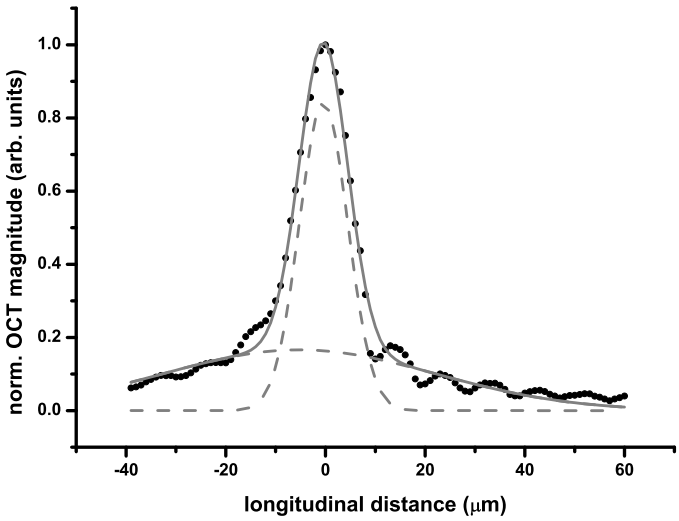

Figure 2.2: Measured coherence gate fitted with the sum of two Gaussian functions. The dots represent the measured data, the gray full line shows the fit to the data, the gray dashed lines show the individual Gaussian.

by a mass discharge measurement. The measured refractive index of the medium is $n = 1.38$.

2.3.3 Data analysis

Processing of the data is performed as follows: raw interferometric data consisting of 1088 data points is Fourier transformed to calculate the complex-valued OCT signal. For every path-length we calculate the autocovariance of the real part of the OCT signal over 1000 time-adjacent acquisitions. This process is repeated 10 times and averaged. The longitudinal and transverse velocities are determined in the time domain by fitting the real part of Eq. (2.12) to the autocovariance of the data. In this fit, v_x and v_z are the free running parameters, while the diffusion coefficient of the colloidal suspension was set to 1.6 ± 0.2 $\mu m^2 s^{-1}$, as measured in a no-flow condition [10].

2.4 Results

First we analyze measurements for transverse flow, i.e., perpendicular to the optical beam ($\theta = 90°$). Figures 2.3(a)-(c) show log-log plots of the magnitude of the Fourier transform of Eq. (2.12) for three depths in the capillary overlaid to the experimental data. Figure 2.3(a) shows data for a depth close to the capillary wall ($z = -0.85R$). The gray dashed line shows the model in Eq. (2.12) with only the transverse directional term and without the contribution of diffusion. A clear discrepancy is observed for the higher frequency content of the signal. The gray full line shows that including the effect of diffusion (the exponential term in Eq. (2.12))

demonstrates good agreement between the directional/diffusive model and the data. Figure 2.3(b) shows a similar plot, but for a depth at the center of the capillary. The diffusive/directional model also agrees well with the data. The slight discrepancy at the larger frequencies is attributed to noise, which is not included in Eq. (2.12). Figure 2.3(c) shows data for a depth of $z = 0.82R$. As can be observed, the power at the higher frequencies is slightly larger (10^{-4} compared to 10^{-5} at 20 kHz) than predicted by theory. We attribute this to noise and multiple scattering present at larger depths which can increase the linewidth of the power spectrum [43, 29]. Figure 2.3(d) shows the measured depth resolved flow velocity profile through the capillary. The dots represent mean values over five measurements and the error bars the corresponding standard deviations. The gray parabolas show the confidence region of the reference velocity measurement. As can be observed, the computed flow velocity is in good agreement with the expected reference parabolas. The velocities obtained from the fit near the solid-liquid interface are slightly larger than expected from the reference. We attribute this to the relative large effect of diffusion compared to the flow velocity at these locations on the OCT signal decorrelation.

Next we analyze measurements for the non-perpendicular direction. Figure 2.4 shows results from an experiment in which the flow velocity vector is oriented at $\theta = 79.5°$. Again, Figs. 2.4(a)-(c) show log-log plots of the magnitude of the Fourier transform of Eq. (2.12) overlaid to the measured data for three depths. Figure 2.4(a) shows data for a depth of $z = -0.89R$ for two cases. For the first case (gray dashed line), the effect of the longitudinal velocity gradient over the coherence gate is neglected, i.e., the integral in Eq. (2.12) is replaced by the Doppler phase term. As can be observed, the frequency at which the power spectrum peaks corresponds well to the Doppler frequency shift. However, the Gaussian and exponential terms describing the transverse directional and longitudinal diffusive dynamics are not sufficient to describe the broadening of the Doppler peak. For the second case (gray full line), the integration of the coherence gate over the longitudinal flow profile is included and, as can be observed, the model is in good agreement with the measurement: the non-uniform distribution of Doppler frequencies in the scattering volume in the presence of a longitudinal velocity gradient explains the additional broadening of the Doppler peak [1]. Figure 2.4(b) shows a similar plot, but at a depth corresponding to the center of the capillary. Here, the additional broadening is negligible since at the center of the flow profile the flow gradient vanishes (gray dashed and full lines indistinguishable). Figure 2.4(c) shows data for the opposite side of the flow profile at a depth of $z = 0.82R$. The Doppler broadening is well described by including the gradient effect. Similar to the results shown in Fig. 2.3, at higher frequencies the measured power is larger than predicted by theory which is attributed to the effect of multiple scattering at larger depths [43, 29]. The power spectra shown in Figs. 2.4(a) and (c) are skewed in opposite directions. This is caused by the asymmetric shape of the coherence gate due to the non-Gaussian shape of the source's spectral shape (cf. Fig. 2.2). Figure 2.4(d) shows the measured depth resolved transverse and longitudinal flow velocities through the capillary using the reference method and a fit of Eq. (2.12) to the data. The two higher flow velocity profiles correspond to the

[1] To evaluate Eq. (2.12) the necessary analytical expression for the longitudinal flow velocity is derived from the Doppler shift measurement.

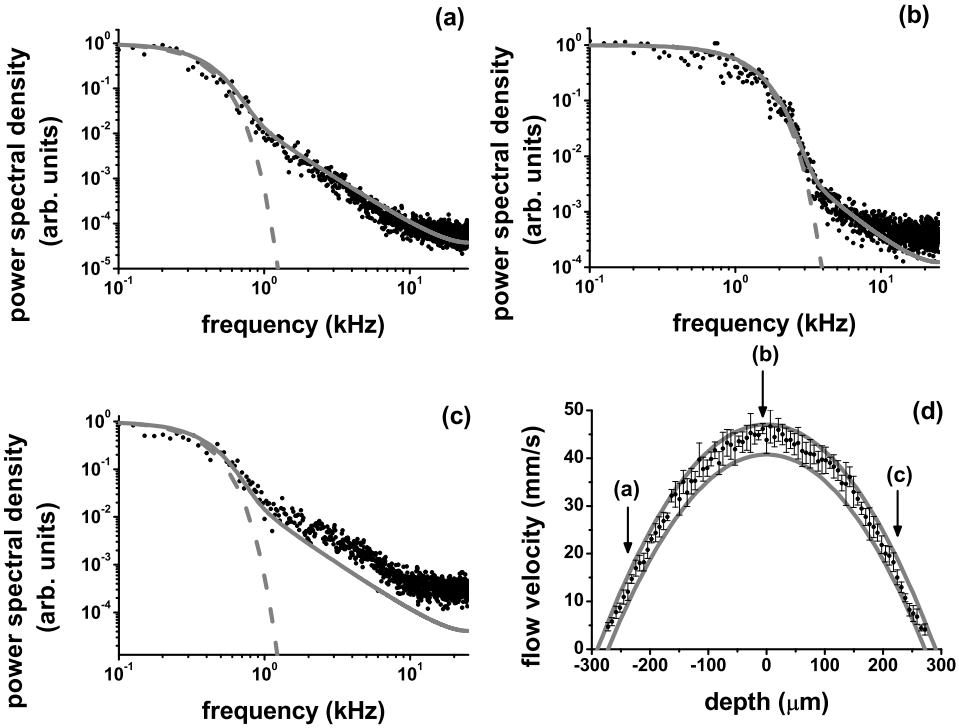

Figure 2.3: Log-log plots of the power spectral density for a perpendicular measurement: (a) at a depth of $z = -0.85R$ close to the capillary wall, (b) at the center, and (c) at a depth of $z = 0.82R$. The dots represent measured data, the gray dashed line represents the model with only directional dynamics and the gray full line the model including diffusion. (d) Depth resolved flow velocities in the capillary. The gray parabolas show the confidence interval of the reference velocity measurement. The arrows correspond to the depths shown in (a)-(c).

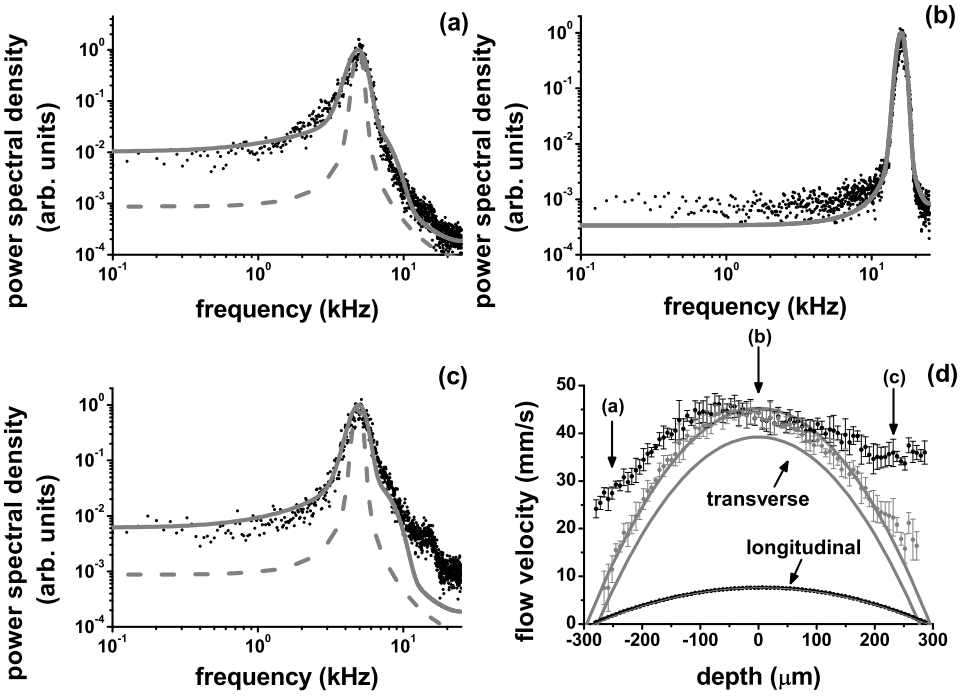

Figure 2.4: Log-log plots of the power spectral density for a measurement on a tilted capillary at $\theta = 79.5°$: (a) depth close to the wall of the capillary $z = -0.89R$, (b) depth at the center, and (c) at a depth of $z = 0.82R$. The dots represent the measured data, the gray dashed line is the model without the convolution with the coherence gate, and the gray full line includes it. (d) Depth resolved transverse and longitudinal flow velocities in the capillary for the two cases described above. The gray parabolas show the bounds of the reference velocity measurement. The arrows correspond to the depths shown in (a)-(c).

transverse velocity determined with and without the velocity gradient and the lower flow velocity profile corresponds to the longitudinal velocity. The error bars for the longitudinal velocity are indistinguishable in the scale of the plot. The gray parabolas show the confidence intervals of the reference velocities. As can be observed, when ignoring the longitudinal velocity gradient within the measurement volume, the broadening of the Doppler peak shown in the previous figures translates into a significant overestimation of the transverse flow velocity (black dots) away from the center of the flow channel. The data that includes the convolution of the coherence gate with the longitudinal phase term in Eq. (2.12), describes the expected transverse parabolic profile very well (gray dots). At large depths a small residual deviation of the transverse velocity is still observable, which we attribute to multiple scattering effects.

As an example application for simultaneous high speed imaging of depth resolved sample morphology and quantitative flow, Fig. 2.5 shows contour plots of the longitudinal and transverse flow velocities through the cross-section of the capillary

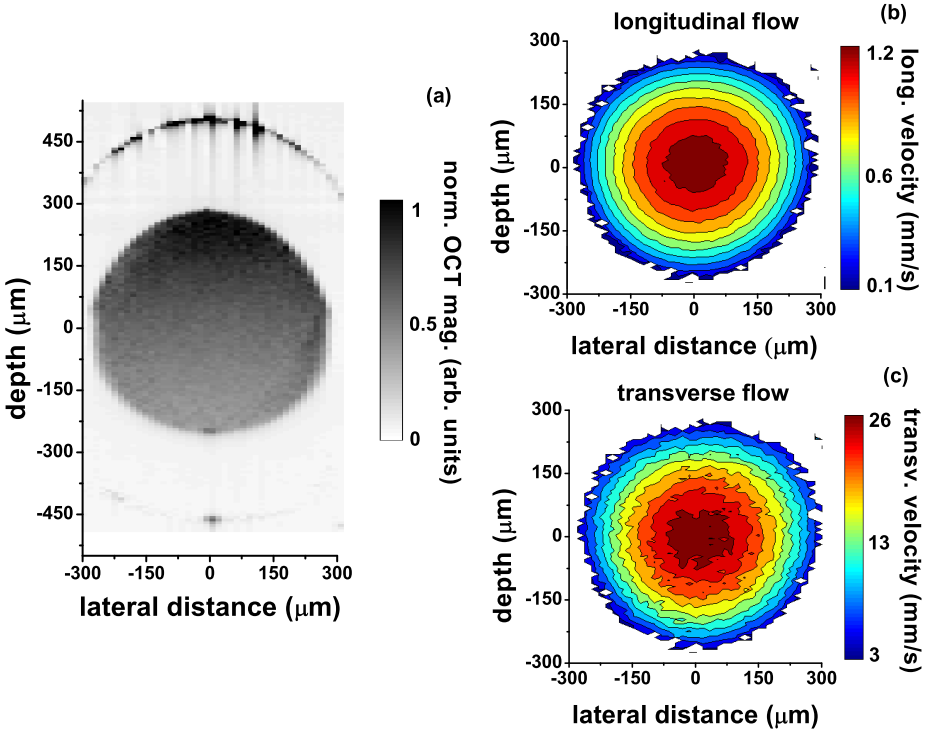

Figure 2.5: (color online). (a) OCT magnitude image of the tilted flow capillary. (b) and (c) Contour plots of the longitudinal and transverse flow velocities in the flow channel. The flow velocity is only computed in the region of interest determined by the OCT magnitude image.

and the corresponding OCT magnitude image. The flow velocity vector is tilted at $\theta = 87.4°$. The images are composed of 37 depth resolved lines with a total acquisition time of 37 s. Using the described method, the measured maximum flow velocity $v_{\max} = \sqrt{v_{x,\max}^2 + v_{z,\max}^2} = 26.3 \pm 1.0$ mm/s at the center of the capillary is in good agreement with the reference velocity of 24.0 ± 2.3 mm/s.

2.5 Discussion

Our results show that we can determine with high accuracy both the longitudinal and transversal flow. The maximum longitudinal and transverse velocities that can be measured are determined by the Nyquist frequency of the time sampling, which is limited by the sweep rate of the laser [42]. The lower bound for the longitudinal velocity is determined by the signal-to-noise ratio [44]. The lower bound for the transverse velocity is determined by the fit of Eq. (2.12) and the dynamic time constants $\tau_1 = (Dq^2)^{-1}$ and $\tau_2 = w_x/v_x$. For small transverse velocities the decorrelation of Eq. (2.12) is dominated by the diffusive term given that $\tau_1 \ll \tau_2$. In the

presence of diffusion an accurate estimation of small transverse velocities is therefore challenging. However, from our theoretical analysis we observe that a smaller value for w_x increases the sensitivity towards the lower range of transverse velocities. However, a smaller w_x decreases the sensitivity for the measurement of the diffusion coefficient [45]. The presented method can be used to determine with micrometer spatial resolution both the diffusion coefficient and the flow velocity from the OCT autocorrelation function simultaneously with the sample morphology. This provides an excellent testing ground for, e.g., the study of the behavior of the diffusion coefficient under shear-stress, which is of paramount importance in studies of shear thinning [46], liquid-gel transitions [47], and anomalous diffusion [48]. Furthermore, using the presented technique diffusion and flow near solid-liquid interfaces and in complex geometries can be studied. These effects are of particular importance in, e.g., hemodynamic research, where the shear-rate has been shown to be a major factor in plaque rupture in arteries [49]. Finally, with the presented technique the effect of flow on rotational diffusion can be studied [27].

2.6 Conclusion

We have presented and validated a theory to quantify the local transverse and longitudinal directional dynamics of a colloidal suspension by measuring the path-length resolved autocorrelation function using optical coherence tomography. In contrast to the studies in Refs. [30, 31, 32, 36], we have an analytical theoretical model, which incorporates the effects of the longitudinal flow velocity gradient and the diffusive dynamics to accurately measure the longitudinal and transverse flow velocity. Based on this model we have obtained accurate results by fitting the model to the measured data with no free/unknown parameters. Our technique yields the local velocity and the sample morphology with high spatial and temporal resolution, which we demonstrated on flow in a capillary. We anticipate that the presented method opens up new opportunities for the study of a range of rheological properties of a variety of (non-)Newtonian fluids in complex flow geometries.

CHAPTER 3

Simultaneous and localized measurement of diffusion and flow using optical coherence tomography

Abstract

We report on the simultaneous and localized measurement of the diffusion coefficient and flow velocity based on the normalized autocorrelation function using optical coherence tomography (OCT). Our results on a flowing suspension of polystyrene spheres show that the flow velocity and the diffusion coefficient can be reliably estimated in a regime determined by the sample diffusivity, the local flow velocity, and the Gaussian beam waist. We experimentally demonstrate that a smaller beam waist results in an improvement of the velocity sensitivity at the expense of the precision and accuracy of the estimation of the diffusion coefficient. Further, we show that the decay of the OCT autocorrelation function due to flow depends only on the Gaussian beam waist irrespective of the sample position with respect to the focus position.

This chapter has been published as:

- N. Weiss, T.G. van Leeuwen, and J. Kalkman, "Simultaneous and localized measurement of diffusion and flow using optical coherence tomography," Opt. Express **23**, 3448-3459 (2015).

3.1 Introduction

Quantification of diffusive and translational dynamics of particles is interesting for the study of fundamental fluid dynamic processes such as, shear dependent diffusion [48], intracellular transport [50], biofilm growth [51], and blood circulation [52] and for a number of applications such as, aerosols [53] and particle sorting [54].

Two techniques are available to quantify flow and diffusion simultaneously. First, particle tracking based techniques such as particle image velocimetry (PIV), use a sequence of (microscopy) images to track the motion of individual particles which are then used to calculate the particle displacement to find the relevant dynamic parameters. Second, dynamic light scattering (DLS) detects the fluctuations of single scattered light from an ensemble of particles without resolving the individual particles. By fitting an appropriate model to the autocorrelation function of the scattered light, the ensemble averaged particle dynamics is measured. However, in the case of PIV the focus has to be mechanically scanned along the propagation direction of the light to produce useful imaging ranges and in DLS the path length distribution of the scattered light is not known, providing only volumetric averaged information about the ensemble particle dynamics in large sample volumes for low particle concentrations.

Localized particle dynamics can be probed using optical coherence tomography (OCT). Using a combination of coherent and confocal gating OCT measures the exact path length distribution of the scattered light up to a few millimeters deep into a sample and with high spatio-temporal resolution [1]. Functional extensions based on the combination of OCT and DLS have been developed to quantify particle diffusion [43, 10, 55, 27], flow velocity [56, 57, 58], and flow and diffusion [36, 59].

In this manuscript we report on the simultaneous and localized measurement of the diffusion coefficient and flow velocity of a colloidal suspension. We quantify the fluctuations in the measured backscattered signal by fitting a model to the normalized autocorrelation function. Previously, we have shown that the autocorrelation function can be used to quantify the flow velocity for arbitrary flow angles in the presence of diffusion [59]. In the case of longitudinal flow, the longitudinal velocity gradient over the coherent detection gate is a source of additional decorrelation of the OCT signal. With the aim of studying the coupling of the flow and diffusion processes in the measurement model, in this work we constrain the flow to be perpendicular to the detection direction. Although, both processes are independent sources of decorrelation, we show that the flow velocity and the diffusion coefficient can be reliably estimated in certain regimes that are determined by the sample diffusivity, the local flow velocity, and the Gaussian beam waist.

3.2 Materials and methods

3.2.1 Optical coherence tomography system

The experiments are performed with a home built fiber-based swept-source OCT system. A schematic of the experimental set-up is shown in Fig. 3.1. The description of the system has been reported elsewhere [59] but is repeated here for convenience. The system operates at a center wavelength of 1312 nm with a bandwidth of 92 nm and a sweep frequency of 50 kHz (Axsun Technologies). The average output power is 20.9 mW and the duty cycle is 59.4%. Data is sampled (ATS9350, AlazarTech) with an interferometrically derived external clock signal at equidistant wavenumber intervals. To ensure phase stability each sweep is triggered by the signal of a fiber Bragg grating centered at 1266 nm (OE Land) [42]. The interferometric signal is detected with a 150 MHz balanced photodetector (PDB450C, Thorlabs) and a 80 MHz low-pass filter (VLF-80+, Mini-Circuits). The trigger signal is detected with a 125 MHz photodetector (1811, New Focus). To assess the influence of the focusing optics on the measured parameters, the sample and reference arms' optics are composed of a collimating lens (PAF-X-18-C, Thorlabs) and three different achromatic doublet focusing lenses (AC254-030-C, AC254-040-C, AC254-100-C, Thorlabs). Unless otherwise stated in the text the 40 mm focal length lens (AC254-040-C) is used. The power splitting ratio of the sample and reference arms is 90/10. The axial resolution is 8.1 ± 0.3 μm in air measured with a mirror reflector.

3.2.2 Flow system

Flow is generated by a perfusion pump (Perfusor fm, Braun) and directed through a cylindrical glass channel with a measured inner diameter of 1097 ± 25 μm or a glass channel with an inner diameter of 50 ± 5 μm (VitroCom). The flowing suspension consists of 1 vol. % polystyrene spheres (PPs-0.2, Kisker) suspended in distilled water. The measured mean sphere diameter is 152±15 nm (np400, qNano, Izon) [60]. The measured refractive index of the medium at 1312 nm is $n = 1.33$. The flow channel is placed perpendicular to the propagation direction of the imaging beam by minimizing the Doppler shift. The experimental flow conditions throughout the manuscript are well described by Poiseuille flow with a maximum Reynolds number of 9 and we assume no hydrodynamic effects on the diffusion. The measured signal-to-noise ratio for the flowing polystyrene suspension using the 30 mm, 40 mm, and 100 mm lens is equal to, 36 dB, 36 dB, and 31 dB, respectively.

3.2.3 Data analysis

The path length resolved diffusion coefficient and flow velocity are measured by fitting a model of the normalized autocorrelation function of the OCT magnitude for every path length independently using the model derived in [59] without the presence of a longitudinal flow component:

$$g(z,\tau) = e^{-2D(z)q^2|\tau|} e^{-2\left[\frac{v(z)\tau}{w_0}\right]^2}, \tag{3.1}$$

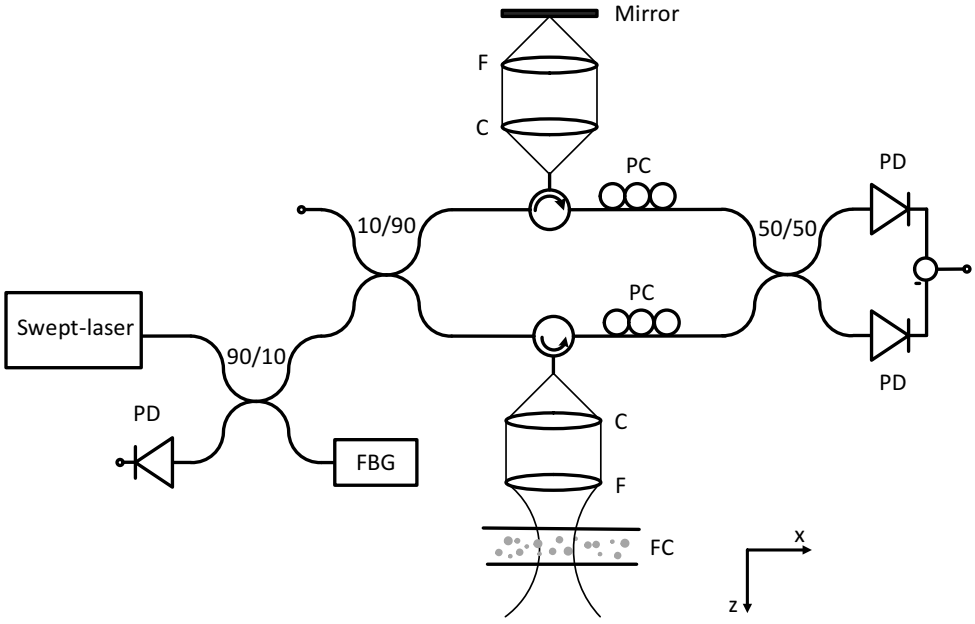

Figure 3.1: Schematic of the experimental swept-source OCT set-up. PD: photodetector, FBG: fiber Bragg grating, PC: polarization controllers, C: collimating lens, F: focusing lens, and FC: flow channel. Gravity is in the z-direction. Adapted from [59].

where the exponential term describes the longitudinal diffusive dynamics and the Gaussian term describes the transverse directional dynamics, with z representing the optical path length (OPL) and $|\tau|$ the time. The additional factor of 2 in the exponents accounts for the use of the magnitude of the OCT signal in the analysis [10]. $D(z)$ is the path length resolved diffusion coefficient given by the Stokes-Einstein equation $D = k_{\mathrm{B}}T_{\mathrm{K}}/6\pi\eta r$, with k_{B} Boltzmann's constant, T_{K} the absolute temperature, η the viscosity, and r the hydrodynamic particle radius. The absolute value of the scattering vector is $q = 4\pi n \sin(\alpha/2)/\lambda$, with n the refractive index of the medium, λ the wavelength in vacuum, and α the scattering angle. Further, $v(z)$ is the path length resolved transverse flow velocity and w_0 is the beam waist ((1/e) radius of the field). The normalization was taken with respect of $g(z, 0)$. For our OCT set-up, the spread of q over the bandwidth is small, therefore we set $q = q_c$ at the center wavelength. The scattering angle α is assumed to be equal to 180°.This assumption is valid for OCT system operating in the backscattering geometry. Due to the moderate numerical apertures used here, no significant deviation is expected from this angle. For the derivation of Eq. (3.1) we have assumed no number fluctuations, independence of particle concentration, and single scattering [59].

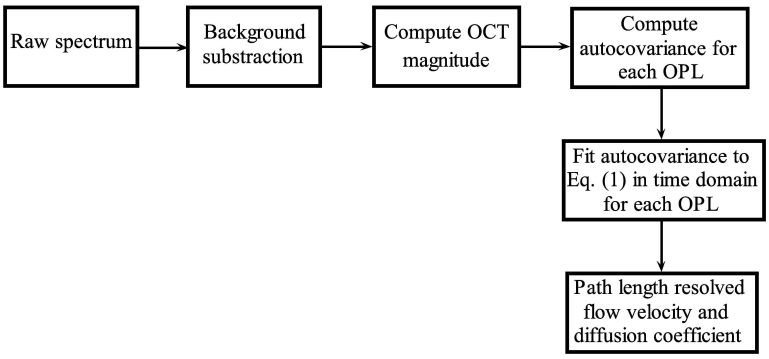

Figure 3.2: Diagram of the data processing steps.

3.2.4 Model fitting

Processing of the data is performed as follows: raw interferometric data consisting of 1088 data points is Fourier transformed to calculate the complex-valued OCT signal. For every path length we calculate the normalized autocovariance of the magnitude of the OCT signal over 5000 time-adjacent acquisitions. This process is repeated 20 times and averaged. The transverse velocity and diffusion coefficient are determined in the time domain by fitting Eq. (3.1) to the data. In this fit, v and D are the fit parameters. In all plots throughout the manuscript, all values of v and D are mean values over 5 measurements and the error bars are the corresponding standard deviations. The error on the fitted parameters is expressed as the coefficient of variation, which is defined as the ratio of the standard deviation to the mean. The results of the model fitting are shown in the frequency domain. Figure 3.2 shows a flow diagram of the data processing steps.

3.3 Results

3.3.1 Diffusion

Figure 3.3 shows results for the measurement of the diffusion coefficient for a suspension of polystyrene spheres in the absence of flow. Figure 3.3(a) shows a typical plot of the normalized OCT magnitude for the flow channel. The focus is placed near the center of the channel to reduce the influence of multiple scattering and noise at longer path lengths [29]. Figure 3.3(b) shows the path length resolved diffusion coefficient for the polystyrene suspension. The calculated mean diffusion coefficient over all path lengths is 3.0 ± 0.2 $\mu m^2/s$. This is in good agreement with the expected diffusion coefficient of 2.8 ± 0.3 $\mu m^2/s$. It should be noted that boundary effects on the diffusion are to be expected, however the range of distances at which these effects occur is small compared to the coherence length of the light source [55]. The power spectral density at path lengths of 516 μm and of 994 μm is calculated and plotted in Fig. 3.3(c) and (d), respectively. The power spectrum is well described by a Lorentzian line shape, which is the Fourier transform of the exponential term of

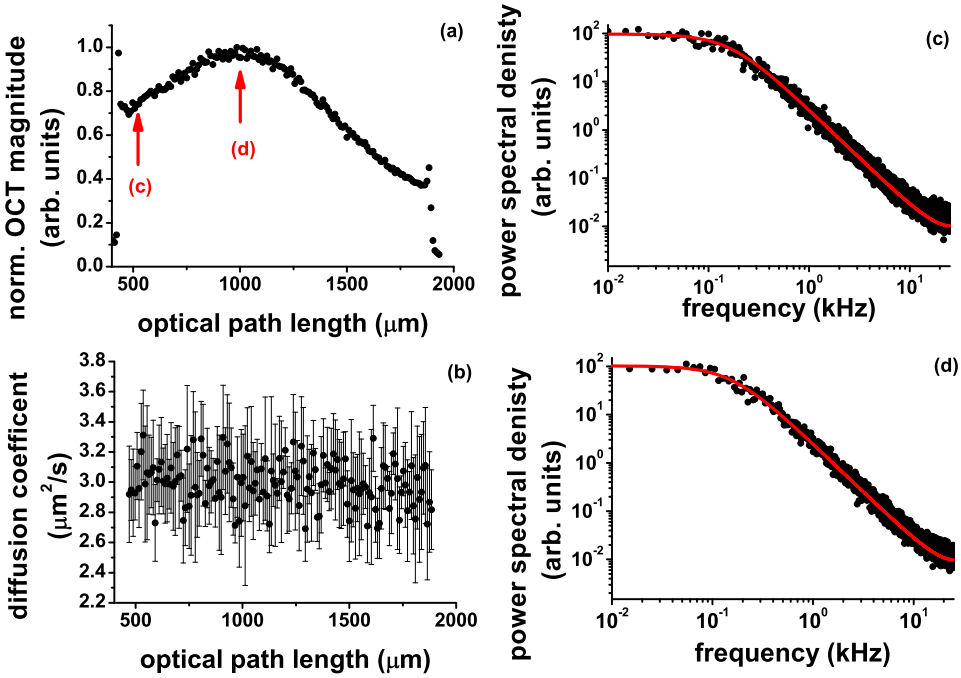

Figure 3.3: Measurement of the local diffusion coefficient of the polystyrene suspension in the absence of flow: (a) Plot of the normalized OCT magnitude in the flow channel. (b) Path length resolved diffusion coefficient for the polystyrene suspension. (c) and (d) Log-log plot of the power spectral density for the optical path lengths shown by the arrows in (a). The circles represent the measured data and the red line represents the model including only the diffusion term.

the normalized autocorrelation function in Eq. (3.1). As can be observed, the data (circles) and the model (line) are in good agreement.

3.3.2 Flow and diffusion, one parameter fit

We start by showing that the decay of the Gaussian term in the normalized OCT autocorrelation function in Eq. (3.1) is characterized by the Gaussian beam waist (i.e., the beam radius at the focus) and not by the local beam radius irrespective of the sample position relative to the focus. Figure 3.4(a) shows plots of the power spectral density for an experiment where a 50 μm diameter channel was translated in the longitudinal direction away from the position of the focus. The measured data (markers) correspond to different distances from the focus, but with the same flow velocity. The data is compared to a model that depends only on the beam waist at the focus and to a model that is based on a depth dependent beam radius. As can be clearly seen, all power spectra overlap and the decay of the power spectral density does not depend on the value of the beam radius at the corresponding distance from the focus, but depends only on the beam waist at the focus. The deviations from

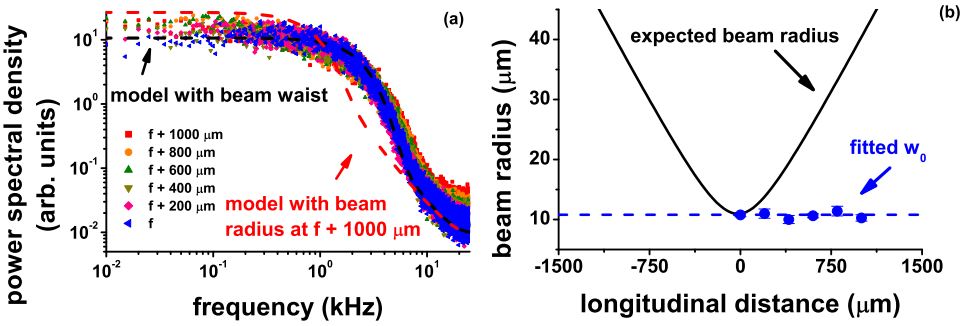

Figure 3.4: Independence of the autocorrelation decay from the local beam radius: (a) Power spectral densities measured at the center of a 50 μm channel at different distances from the focus but for the same flow velocity. The markers show the measurements and the dashed lines show the expected models using the beam waist (black) and using the beam radius at 1000 μm from the focus (red). (b) Beam radius for a focused Gaussian beam (line) and fitted w_0 (markers).

3

the model at high frequencies is attributed to the influence of noise which increases with increasing distance from the focus. Figure 3.4(b) shows the expected beam radius for a focused Gaussian beam for a lens with a focal length of 40 mm and the values for the beam waist calculated by fitting the data shown in Fig. 3.4(a) and by letting w_0 be the only fitting parameter in Eq. (3.1). Clearly, the fitted values of w_0 are independent of the position of the sample with respect to the focus.

Figure 3.5 shows results for the measurement of the path length resolved flow velocity with the diffusion coefficient fixed to the value measured in the no-flow case (cf. Sec. 3.3.1). Since the diffusion coefficient does not depend on optical path length, v is the only fitting parameter in Eq. (3.1). Figure 3.5(a) shows the path length resolved flow velocity. The gray parabola shows the reference velocity calculated based on the flow rate set by the perfusion pump and the diameter of the channel. As can be observed, the measured flow velocity is in good agreement with the reference values. Figure 3.5(b) shows the coefficient of variation of the fitted flow velocity. For optical path lengths close to the walls of the channel an increase in the coefficient of variation is observed. Figure 3.5(c) and (d) show the power spectral density for the path lengths shown by the arrows in Fig. 3.5(a). The circles show the data and the black line shows the data corresponding to the no-flow diffusion experiment. For the path length close to the wall of the channel, the decay of the power spectral density for the flow experiment is well described by a Lorentzian decay as was the case for the no-flow experiment. However, for the path length corresponding to the center of the channel, this is no longer the case: the contribution of the Gaussian (flow) term is clearly observed in the first half of the frequency range. For all path lengths, an excellent agreement is observed between the data and the model.

Figure 3.6 shows the dependency of the velocity uncertainty for different Gaussian beam waists. Figure 3.6(a) shows the beam radius for three focusing lenses measured with the knife edge method [61]. The squares correspond to a lens with a focal length

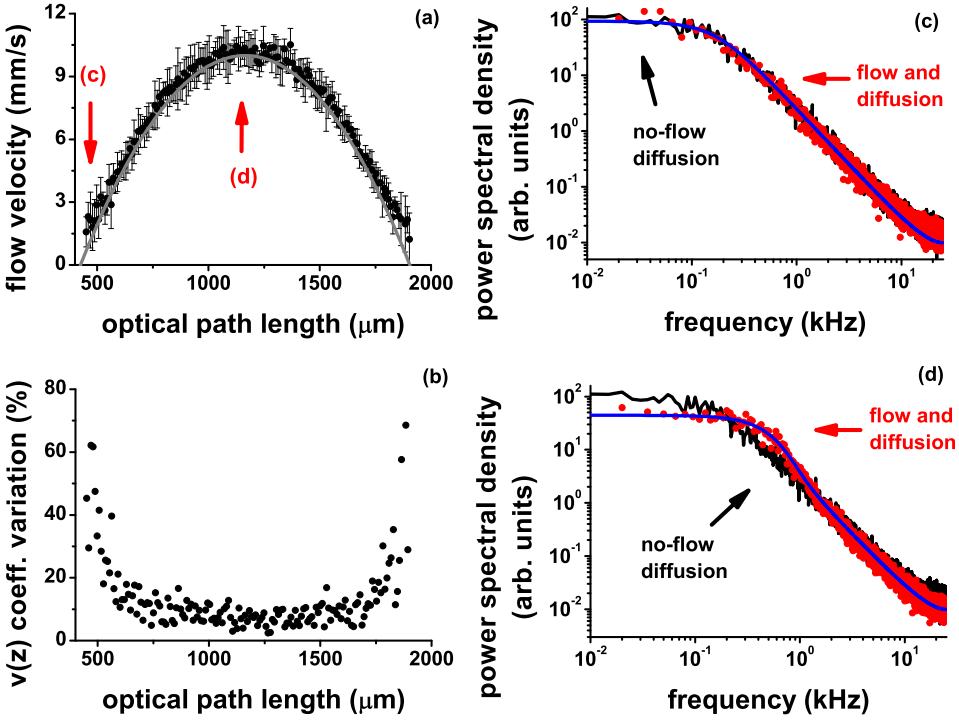

Figure 3.5: (a) Measured path length resolved flow velocity (circles) through the cylindrical flow channel and reference velocity (gray line). The arrows correspond to the path lengths shown in (c) and (d). (b) Coefficient of variation for the measured flow velocities shown in (a). (c) Measured power spectral density for a path length close to the wall of the channel (red circles) and fitted model (blue line). For comparison, the black line shows the no-flow diffusion case (cf. Fig. 3.3(b)). (d) Similar to (c), but for a path length corresponding to the center of the flow channel.

of 30 mm, the circles for a lens with a focal length of 40 mm, and the triangles for a lens with a focal length of 100 mm. The dashed lines show the corresponding Gaussian beam models. The measured waist values are 8.5 ± 0.5 μm, 10.8 ± 0.5 μm, and 26.3 ± 1 μm, respectively. Figure 3.6(b) shows the flow velocity's coefficient of variation measured in three different experiments with the three lenses plotted versus the flow velocity. For each experiment the maximum reference flow velocity is 10 mm/s. The coefficient of variation monotonically decreases for increasing flow velocity for all three lenses. For a particular flow velocity, the choice of a smaller beam waist results in a lower value for the coefficient of variation compared to the values measured with a larger beam waist.

3.3.3 Flow and diffusion, two parameter fit

Figure 3.7 shows the power spectral density for an optical path length near the edge of the channel (Fig. 3.7(a)) and for an optical path length corresponding to the

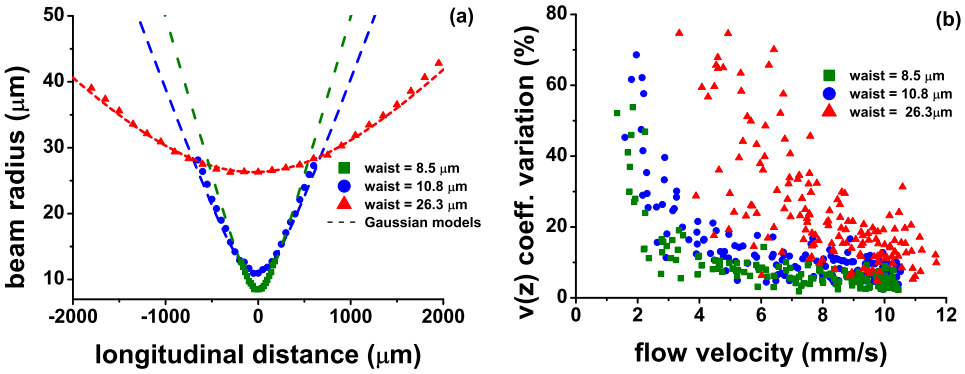

Figure 3.6: (a) Beam radius in the longitudinal direction of the imaging beam for three focusing lenses. The markers represent the data and the dashed lines show the corresponding Gaussian beam models. (b) Coefficient of variation versus the measured flow velocity.

center of the channel (Fig. 3.7(b)). A fit of both diffusion and flow (blue line) to the data (circles) is compared to the contributions of only diffusion (green) and only flow (red). It can be seen that at optical path lengths with relatively low flow velocity values the decay of the power spectral density is well described by a Lorentzian (diffusion) power spectrum. However, for relatively larger flow velocities, the decay of the power spectral density at low frequencies is well described by a Gaussian (flow) power spectrum and at high frequencies it converges towards a Lorentzian power spectrum.

Figure 3.8 shows results for the simultaneous measurement of the diffusion coefficient and the flow velocity based on data similar to the one shown in Fig. 3.7. Figure 3.8(a) shows the path length resolved flow velocities for a set of three varying reference velocities. The markers show the measured velocities and the lines show the reference velocities. The measured velocity values are well in agreement with the expected reference values. Figure 3.8(b) shows the corresponding coefficient of variation for the fitted velocities. For optical path lengths close to the walls of the channel an increase in the coefficient of variation is observed similar to the case for a fit with fixed diffusion (cf. Fig. 3.5). Figure 3.8(c) shows the measured path length resolved diffusion coefficient (markers) determined simultaneously with the flow velocities shown in Fig. 3.8(a). The diffusion coefficient measured in the no-flow case is shown here as a reference (line). As can be observed, the diffusion coefficient measured at relatively low flow velocities is in good agreement with the reference values. For the relatively large flow velocities at the center of the flow channel, a path length dependency of the measured diffusion coefficient is observed where the diffusion coefficient at the center of the channel is larger than the diffusion coefficient measured near the wall of the channel. As the maximum flow velocity through the center of the channel increases, the overestimation of the diffusion coefficient increases as well. Figure 3.8(d) shows the coefficient of variation for the fitted diffusion coefficient. For optical path lengths close to the center of the channel an increase in the coefficient of variation is observed.

Figure 3.9 shows results for the simultaneous measurement of the diffusion coef-

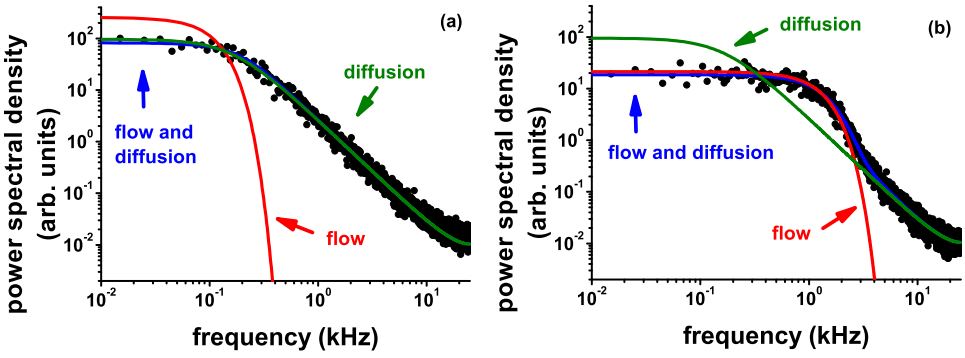

Figure 3.7: Power spectral densities for an optical path length close to the edge of the channel (a) and for an optical path length at the center of the channel (b). The circles show the data, the blue line shows the full model accounting for flow and diffusion, the red line shows the model accounting only for flow, and the green line shows the model accounting only for diffusion.

ficient and the flow velocity at high flow rates measured with two lenses with a waist of 26.3 μm and a waist of 10.8 μm. Figure 3.9(a) shows the path length resolved flow velocity and Fig. 3.9(b) shows the corresponding diffusion coefficient. As can be seen, the flow velocity measured with both lenses and the diffusion coefficient measured with the largest waist are in good agreement with the reference values. However, the diffusion coefficient measured with the smallest waist is overestimated in the center of the channel (cf. Fig. 3.8). Figure 3.9(c) and (d) show the coefficient of variation for the measured flow velocity and the diffusion coefficient, respectively. For both waists the flow velocity is measured accurately. The larger beam waist results in an improved estimation of the diffusion coefficient.

3.4 Discussion

Based on the theoretical model derived in Ref. [59] we have studied the simultaneous measurement of the local diffusion coefficient and flow velocity of a colloidal suspension.

We have constrained the experimental and fitting conditions to study the influence of the diffusion coefficient, the flow velocity, and the beam waist on the measured OCT autocorrelation function. Our experimental results show that, although the diffusive and translation dynamics enter Eq. (3.1) as independent multiplicative decorrelation terms, a reliable estimation of both quantities is challenging. In the case of the presence of a single dynamical process the estimation is straightforward, as we have shown for diffusion only.

The extension of this analysis to the case of two component particle dynamics is not trivial. Interestingly, interpreting the Gaussian (flow) term as being a transit time effect of the moving scatterers through the illumination profile would result in a dependence on the local beam radius. However, we have shown that the decay of the normalized OCT autocorrelation function is characterized by the beam waist

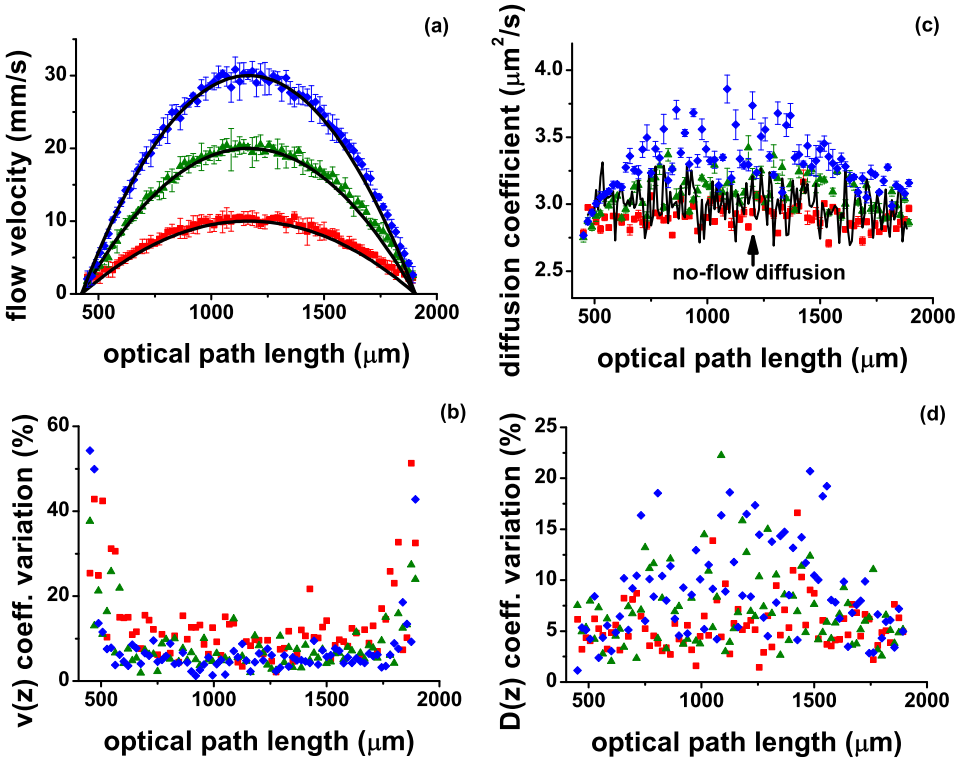

Figure 3.8: Simultaneous fitting of flow and diffusion for a set of different reference velocities: (a) Path length resolved flow velocity. The solid line shows the reference velocity. (b) Coefficient of variation of the fitted flow velocity. (c) Path length resolved diffusion coefficient for the velocities shown in (a). (d) Coefficient of variation of the fitted diffusion coefficient. For the sake of visualization, in Figs. (a-d) only every other data point has been plotted.

irrespective of the longitudinal position of the scatterer with respect of the focus. This is in excellent agreement with the theoretical prediction given in Ref. [45], where this effect is attributed to the phase curvature of a focused Gaussian beam. More specifically, away from the focal plane the effect of beam radius increase and curvature increase compensate each other in the measured decay rate. As a result, the decay due to flow does not depend on the local Gaussian beam radius.

Our experimental results show that the uncertainty with which either the diffusion coefficient and the flow velocity can be quantified is determined by the contributions from the single exponential (diffusion) and Gaussian (flow) decay terms in the autocorrelation function. In the particular case of relatively low flow velocities the decay of the autocorrelation function is dominated by the diffusive dynamics and is well described by a single exponential decay. In this case, the contribution of the Gaussian (flow) term to the total decay is small and therefore the estimation of the flow velocity has a large uncertainty. In the case of relatively high flow velocities the decay of the autocorrelation function is dominated by the translational dynamics

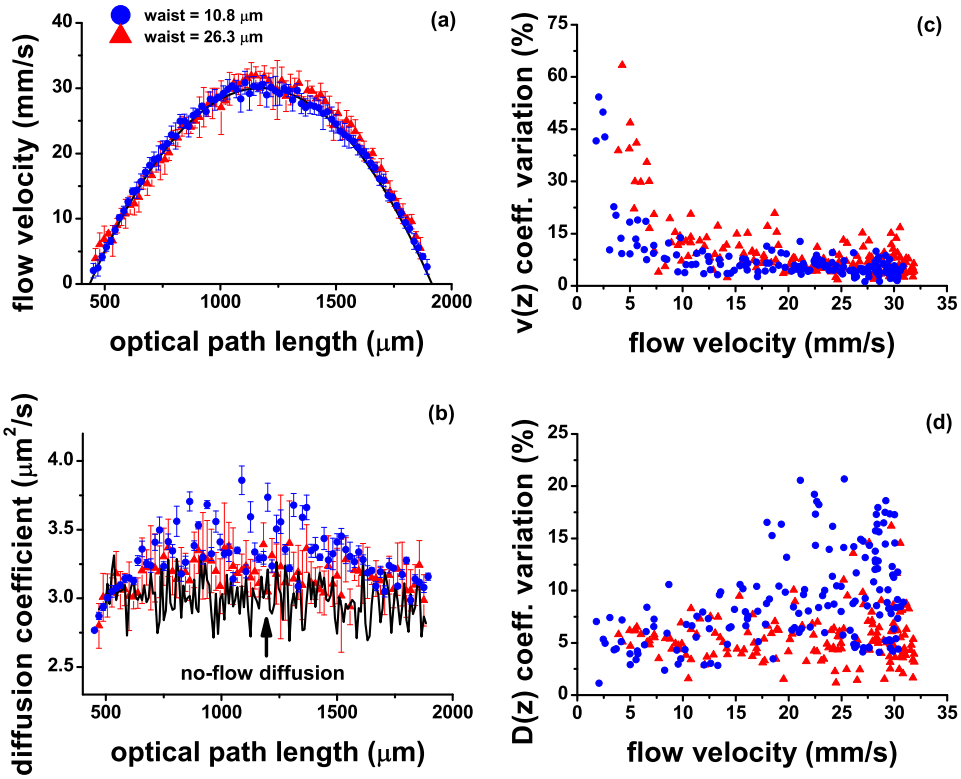

Figure 3.9: Simultaneous measurement of flow and diffusion at high flow rates. (a) Path length resolved flow velocity measured using a waist of 10.8 μm (blue circles) and measured using a waist of 26.3 μm (red triangles). The solid line shows the reference velocity. (b) Path length resolved diffusion coefficient corresponding to the velocity values shown in (a). The solid line shows the diffusion coefficient measured in the absence of flow. (c) Coefficient of variation for the flow velocities. (d) Coefficient of variation for the diffusion coefficient. For the sake of visualization, in Figs. (a) and (b) only every other data point has been plotted. Note that the data for the waist of 10.8 *μm is the same as in Fig. 3.8.*

and is well described by a Gaussian decay. This results in a large uncertainty of the diffusion coefficient since the contribution of the single exponential decay to the total decay is relatively small. Note also that the uncertainty in the fitted diffusion coefficient and flow velocity is caused by uncertainties in either dynamic process (spread in data) and by correlation between fit parameters (systematic overestimation of diffusion for high flow).

The choice of the beam waist determines in which regime either dynamical process dominates the decay of the autocorrelation function. We identify two regimes for the choice of the beam waist. For applications that deal mainly with the estimation of the diffusion coefficient, it is more suitable to choose a larger beam waist such that the decay due to diffusion dominates over a large part of the velocity range of interest. However, for applications which deal mainly with quantifying small flow

velocities, a smaller beam waist is more suitable such that the decay due to flow dominates. As an illustrative example, we plotted in Fig. 3.10 the decay time constants $\tau_D = (2Dq^2)^{-1}$ (diffusion) and $\tau_v = (\sqrt{2}v/w_0)^{-1}$ (flow) based on the data shown in Fig. 3.9 (a), (c), and (d). As long as the decay due to diffusion dominates over the decay due to flow, the uncertainty of the diffusion coefficient is approximately 5%. However, as the decay due to flow starts dominating, the uncertainty in D increases. A similar behavior is observed for the uncertainty of the flow velocity, where an uncertainty of 5% is measured when the decay due to flow determines the total decay, but the precision decreases when diffusion becomes more dominant. Finally, by choosing either a large or a small beam waist we can choose the precision with which we can measure either D, v, or both together.

In principle, a generalization of our results to arbitrary values of the beam waist is possible but should be performed with care. For small beam waists a strong reduction in the depth of focus would become a limitation for practical applications requiring long imaging ranges. Also, as a consequence of tight focusing a stronger dependency on the scattering angle is expected which has been shown to result in a more complex functional decay for the diffusive dynamics [62]. Furthermore, for a fixed laser sweep rate a smaller beam waist will limit the maximum flow velocity that can be measured. In this case, the temporal resolution of the autocorrelation function should be sufficiently small to sample the flow decay $\tau_v = (\sqrt{2}v/w_0)^{-1}$ sufficiently. For large beam waists the influence of low signal-to-noise ratios [58] and multiple scattering [63] should also be considered. In our experiments and at the measured signal-to-noise ratios, the influence of the signal-to-noise ratio on the estimated dynamical parameters can be neglected. A thorough description of these effects on the estimation uncertainty of the dynamical parameters is subject of future research.

For this study, we have constrained the flow to be perpendicular to the propagation direction of the imaging beam. By doing this, we have been able to study the influence of flow and diffusion on the amplitude terms of the normalized autocorrelation function. In essence, a generalization to arbitrary flow directions is possible. As we have shown previously, a longitudinal flow velocity component can be accurately measured by fitting an additional phase term to the normalized autocorrelation function [59]. For moderate longitudinal flow the phase and the amplitude terms in the autocorrelation function remain uncoupled and thus, the results presented in this work can be generalized directly to the more complex case of arbitrary flow direction.

3.5 Conclusion

We presented measurements of the local diffusion coefficient and flow velocity based on the normalized autocorrelation function measured by optical coherence tomography. Based on our model, we have obtained accurate results by fitting the model to the measured data with only the physically relevant parameters as fitting parameters. Our results on a flowing suspension of polystyrene spheres show that the flow velocity and the diffusion coefficient are reliably estimated. The regime where this is possible is determined by the diffusion coefficient of the sample, the local flow velocity, and the Gaussian beam waist produced by the focusing optics. We have

experimentally shown that a smaller beam waist results in an improved estimation of the flow velocity and that a larger beam waist results in an improved estimation of the diffusion coefficient. Finally, we showed that the decay of the autocorrelation function due to flow depends only on the Gaussian beam waist irrespective of the sample position with respect to the focus position.

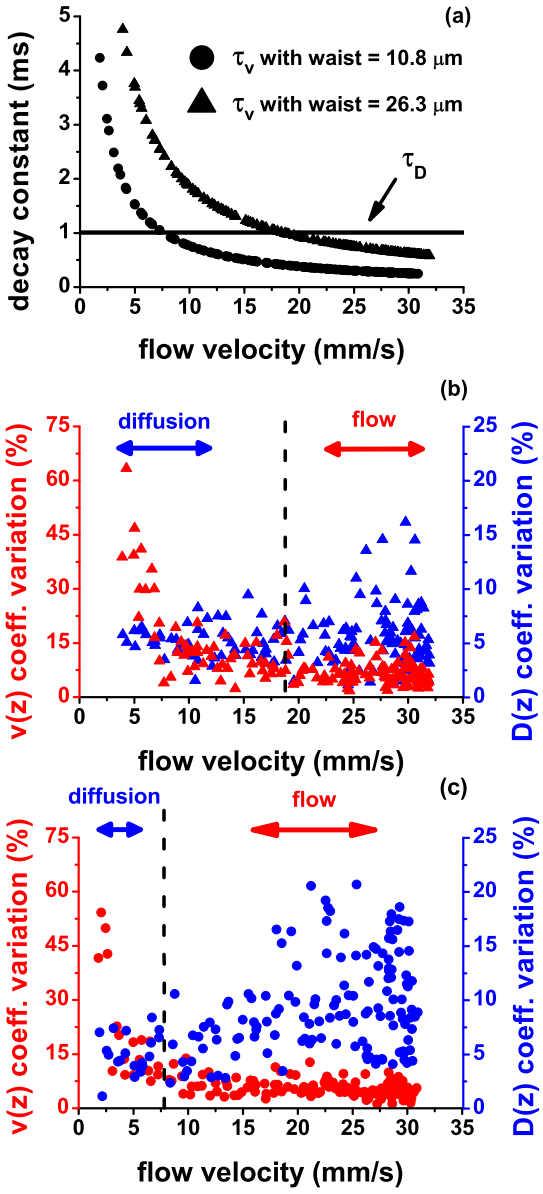

Figure 3.10: (a) Decay time constants of the flow (markers) and diffusion (line) terms of the OCT autocorrelation function. (b) Coefficient of variation for the flow velocity (red markers, left ordinate) and for the diffusion coefficient (blue markers, right ordinate) measured with a waist of 26.3 μm. *The dashed lines show the transition point for the regimes where diffusion of flow dominate the decay. (c) Similar to (b), but measured with a waist of* 10.8 μm.

CHAPTER 4

Measurement of biofilm growth and local hydrodynamics using optical coherence tomography

Abstract

We report on localized and simultaneous measurement of biofilm growth and local hydrodynamics in a microfluidic channel using optical coherence tomography. We measure independently with high spatio-temporal resolution the longitudinal flow velocity component parallel to the imaging beam and the transverse flow velocity component perpendicular to the imaging beam. Based on the measured velocities we calculate the shear-rates in the flow channel. We show the relation between the measured biofilm structure and flow velocities as biofilm growth progresses over the course of 48 hours.

This chapter has been published as:

- N. Weiss, K. El Tayeb El Obied, J. Kalkman, R.G.H. Lammertink, and T.G. van Leeuwen,"Measurement of biofilm growth and local hydrodynamics using optical coherence tomography," Biomed. Opt. Express **7**, 3508-3518 (2016).

4.1 Introduction

Bacteria have the ability to attach to a large variety of surfaces. Under favorable conditions individual bacteria cells can group to form large colonies called biofilms. Biofilms are characterized by the production of an extracellular matrix as well as a modified cellular growth rate when compared to planktonic organisms [64]. These altered structural and physiological states make biofilms more resistant to antibiotics, disinfectants, and germicides [64]. The formation of biofilms is characterized by a three-step process: attachment, maturation, and dispersal. During the attachment phase, individual planktonic cells attach to an inert surface to from a microcolony. With the right environmental cues the biofilm matures via cellular proliferation and the production of an extracellular polymeric matrix [65]. During dispersal, planktonic cells leave the original biofilm and can re-attach downstream at a new location and initiate another biofilm lifecycle. In biomedical applications, and particularly in the use of medical devices, this process causes spreading of infections if the host organism fails to eradicate the mobile planktonic cells [66]. In industrial applications, such as e.g., the production of drinking water, it has been shown that biofilm detachment is responsible for increased concentrations of planktonic cells and is therefore a source of persistent contamination [67]. Biofilm dispersal originates mainly from two driving mechanisms, the first is based on internal biofilm processes, such as enzymatic degradation, and the second is based on perturbations of the hydrodynamic environment, such as an increase in shear forces [68]. It has been shown that the local hydrodynamics also modifies the structure of biofilms, e.g., by creating biofilm streamers that cause exponentially fast clogging of industrial and medical flow systems [51]. Hence, simultaneous measurement of both biofilm structure and local hydrodynamic parameters is paramount for the understanding of transient biofilm dynamics such as biofilm detachment and dispersal.

Biofilm morphology and local flow have been measured by combining confocal laser scanning microscopy with particle image velocimetry [20] and by nuclear magnetic resonance [69]. More recently, the potential of optical coherence tomography (OCT) to measure biofilm structure non-invasively and label-free has been demonstrated [70]. Moreover, OCT is very well apt to measure local flow as Doppler-OCT has been applied to measure shear-rate distributions in asymmetric flow channels [71]. For biofilms, OCT imaging has been applied to study membrane biofouling [72, 73, 74], to study biofouling mitigation using two phase flow cleaning [75], to characterize biofilm structure in lab scale reactors [76], to study dynamic deformations and to estimate biofilm mechanical properties [77], to visualize biofilm formation *in-vivo* [78, 79], to study structural transient effects [80, 81], and to visualize biofilm growth under laminar and turbulent flow conditions [82].

In this paper, we use optical coherence tomography (OCT) to simultaneously quantify biofilm structure and the related flow velocities and shear-rates in a microfluidic channel. We measure independently with high spatio-temporal resolution the longitudinal flow velocity component parallel to the imaging beam and the transverse flow velocity component perpendicular to the imaging beam based on the OCT autocorrelation function. Based on the velocity measurements, we calculate the shear-rates inside the microfludic channel. We show the relation between the

local biofilm structure and the local flow velocity as biofilm growth progresses over the course of two days.

4.2 Materials and Methods

4.2.1 Optical coherence tomography system

The experiments are performed with a home built fiber-based swept-source OCT system. A schematic of the experimental set-up is shown in Fig. 4.1(a). The description of the system has been reported elsewhere [59] but is repeated here for convenience. The system operates at a center wavelength of 1312 nm with a bandwidth of 92 nm and a sweep frequency $f_s = 50$ kHz (Axsun Technologies). The average output power is 20.9 mW and the duty cycle is 59.4%. Data is sampled (ATS9350, AlazarTech) with an interferometrically derived external clock signal at equidistant wavenumber intervals. To ensure phase stability each sweep is triggered by the signal of a fiber Bragg grating centered at 1266 nm (OE Land) [42]. The interferometric signal is detected with a 150 MHz balanced photodetector (PDB450C, Thorlabs) and a 80 MHz low-pass filter (VLF-80+, Mini-Circuits). The trigger signal is detected with a 125 MHz photodetector (1811, New Focus). The sample and reference arms' optics are composed of a collimating lens (PAF-X-18-C, Thorlabs) and an achromatic doublet focusing lens (AC254-040-C, Thorlabs). The power splitting ratio of the sample and reference arms is 90/10. The longitudinal resolution is $w_z = 8.1 \pm 0.3$ µm in air measured with a mirror reflector and the transverse resolution is $w_t = 10.8 \pm 0.2$ µm measured with a knife edge. The imaging beam is scanned laterally using a galvanometric mirror (GVSM002, Thorlabs).

4.2.2 Flow system

Flow is generated by two pressure vessels (Schott) and directed through a flow system consisting of tubing, valves, a mass-flow controller, and a flow channel. A schematic of the flow set-up is shown in Fig. 4.1(b). The flow channel was fabricated by casting Polydimethylsiloxane (PDMS) (Sylgard 184, Dow Corning) over a SU-8 master mold with the channel structure. The cured PDMS is sealed from the top with a glass plate (150 µm thickness). The flow channel has a length of 1.1 cm and a rectangular cross-section of 200 µm by 400 µm. The first pressure vessel contains a suspension of 0.5 vol.% 200 nm polystyrene spheres (PPs-0.2-S-PEG30000, Kisker). These particles act as tracers that provide backscattering from the fluid in order to measure the flow velocity with the OCT system. The second pressure vessel contains the solution with the bacteria. For growing the biofilms, the methods used in membrane filtration experiments were followed. In these experiments mixed bacterial communities are used instead of monocultures. D-glucose, sodium nitrate, and anhydrous sodium phosphate were used as nutrients and were added to tap water in a mass ratio carbon:nitrogen:phosphorous of 100:20:10 [83, 72]. The initial carbon concentration was 1 mg/L. All the chemicals were purchased from Sigma-Aldrich. Both pressure vessels are driven at 1 bar and are connected to a mass flow controller (mini CORI-FLOW M12V14I, Bronkhorst) via two independent valves.

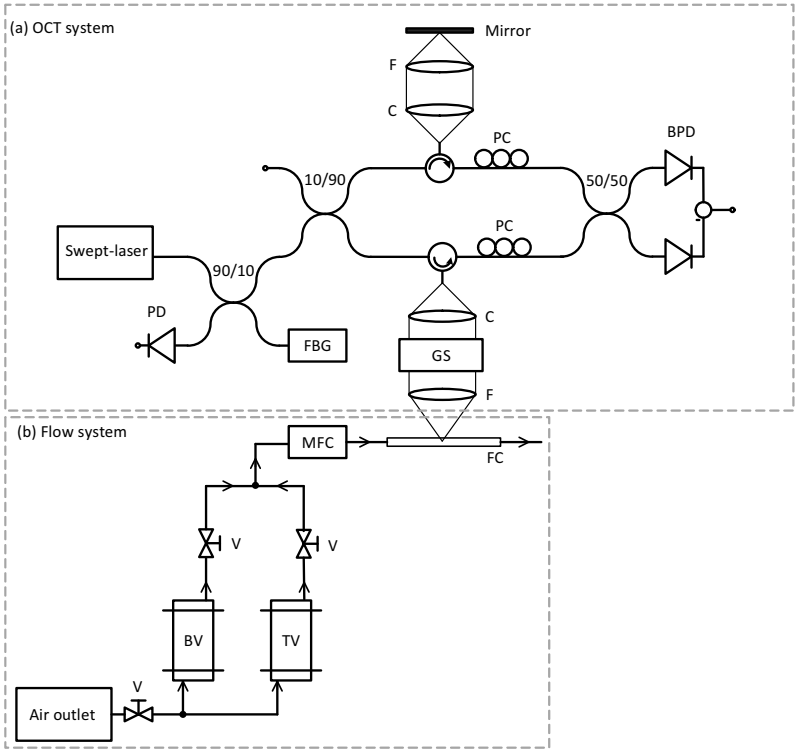

Figure 4.1: Schematic of the experimental swept-source OCT set-up (a) and flow system (b). PD: photodetector, FBG: fiber Bragg grating, PC: polarization controllers, C: collimating lens, F: focusing lens, GS: galvanometric scanner, FC: flow channel, TV: tracer vessel, BV: bacteria vessel, V: valve, and MFC: mass flow controller. Adapted from Ref. [59].

During OCT flow measurements, the tracer vessel valve is open and the bacteria vessel valve is closed. During a vessel switch event both valves remain open for a period of two minutes to ensure pressure stabilization in the flow lines. For the rest of the experiment, the tracer vessel valve remains closed and the bacteria vessel valve remains open. During the entire experiment the flow rate is set to 2.5 g/h. The Reynolds number in the reference flow measurements is Re = 3. One cycle of the valve operation scheme is shown in Fig. 4.2(a). To reduce the effect of increased gas solubility inside the pressure vessels, the liquid phase was isolated from the gas phase with a plastic flexible container. The experiment is run for a total of 48 hours with OCT measurements taken every 24 hours.

4.2.3 Data Acquisition

Biofilm morphology and flow velocities are measured over a 200 μm by 200 μm area of the flow channel over the course of two days. A schematic of the scan geometry is shown in Fig. 4.2(b). The beam is scanned in discrete steps of 5 μm in the x- and y-direction. At every point the imaging beam is held stationary for 600 ms to

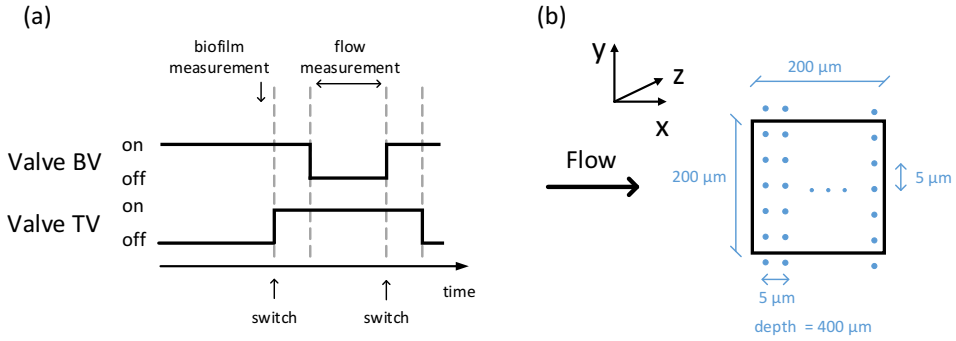

Figure 4.2: (a) One cycle of the valve operation scheme. At a vessel switch event both valves remain open for a period of two minutes. Flow measurements are performed only when the tracer vessel valve is open. Biofilm morphology measurement is performed before opening the tracer vessel valve. (b) Top view of the flow channel showing the scanning geometry of the imaging beam. Each dot represents the position of the imaging beam in the (x, y)-plane during the scan. The step resolution in the x- and y-direction is 5 µm. The main flow direction is in the positive x-direction.

4

acquire the interferometric signal. Due to the lack of contrast between the biofilm and the tracer particles, the morphology of the biofilm is measured in the absence of tracers (cf. Fig. 4.2(a)). The flow channel is aligned such that (x, y)-plane is parallel to the focal plane of the OCT system and gravity is in the positive z-direction.

4.2.4 Data analysis

The depth resolved flow velocity is measured at every position (x, y) by fitting a model of the normalized autocorrelation function of the OCT magnitude for every depth independently using the model derived in Refs. [59, 36, 58]:

$$g(z,\tau) = e^{-2D(z)q^2|\tau|} e^{-2\left[\frac{v_t(z)\tau}{w_t}\right]^2} e^{-\left[\frac{v_z(z)\tau}{w_z}\right]^2}, \tag{4.1}$$

where the first exponential term describes the longitudinal diffusive dynamics, the two Gaussian terms respectively describe the transverse and longitudinal flow dynamics , with z representing depth and $|\tau|$ the time lag of the autocorrelation function. The additional factor of 2 in the exponents accounts for the use of the magnitude of the OCT signal in the analysis [10]. The variable $D(z)$ is the depth resolved diffusion coefficient. The measured diffusion coefficient of the tracer particles under no-flow conditions is $D(z) = 2.3 \pm 0.2$ µm^2/s. The absolute value of the scattering vector is $q = 4\pi n \sin(\alpha/2)/\lambda$, with n the refractive index of the medium, λ the wavelength in vacuum, and α the scattering angle. The measured refractive index of the medium at 1312 nm is $n = 1.33$. Further, in the first Gaussian term, $v_t(z) = (v_x(z)^2 + v_y(z)^2)^{1/2}$ is the depth resolved transverse flow velocity and w_t is the beam waist ((1/e) radius of the field). In the second Gaussian term, $v_z(z)$ is the depth resolved longitudinal flow velocity and w_z is the waist ((1/e) radius) of the coherent detection gate. The normalization was taken with respect to $g(z, 0)$. For

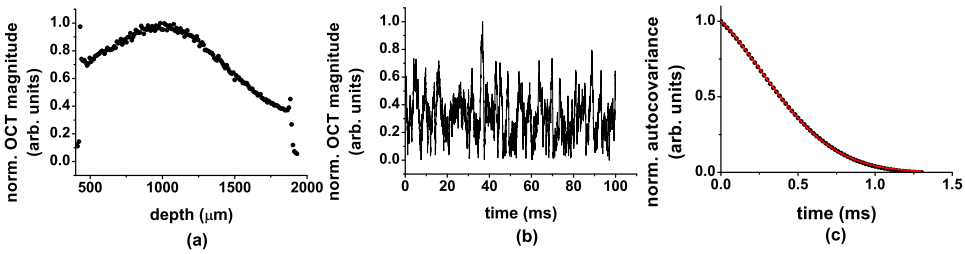

Figure 4.3: Schematic of the processing steps to fit the transverse flow velocity: (a) Normalized magnitude of the OCT signal; the amplitude variations over time for a particular depth are shown in (b) and (c) autocovariance of the data and fit (line).

our OCT set-up, the spread of q over the bandwidth is small, therefore we set $q = q_c$ at the center wavelength and $\alpha = 180°$. Furthermore, under the experimental conditions described here, we assume in Eq. 4.1 that the spread of Doppler frequencies over the coherent detection gate can be neglected [59].

4.2.5 Data processing

Processing of the data is performed as follows: raw interferometric data consisting of 1088 data points is Fourier transformed to calculate the complex-valued OCT signal $a_{OCT}(z,t)$, where t represents time. In order to conserve the sign of the longitudinal flow velocity, the calculation of the flow velocities is performed in a two-step process. First, the longitudinal flow velocity $v_z(z)$ is measured by calculating the phase difference $\Delta\varphi(z)$ of $a_{OCT}(z,t)$ of time-adjacent acquisitions as $v_z(z) = \Delta\varphi(z)\lambda f_s/4\pi n$, with $\Delta\varphi(z) = \arg\left[a_{OCT}(z,t+dt)a^*_{OCT}(z,t)\right]$, where * denotes complex conjugation and $dt = f_s^{-1}$ [44]. Second, to measure the transverse flow velocity $v_t(z)$, we calculate the autocovariance of the magnitude of the OCT signal over 1000 time-adjacent acquisitions for every depth inside the flow channel. This process is repeated 10 times and averaged. The transverse velocity is determined in the time domain by fitting Eq. (4.1) to the normalized autocovariance of the data. In this fit, v_t is the only fit parameter. v_z and D enter the fit as constant parameters. The diffusion coefficient D is set equal to the measured no-flow value [84]. In all plots throughout the manuscript, all values of v_t and v_z are mean values over 3 measurements and the error bars are the corresponding standard deviations. The averaging over 3 measurements is performed by splitting the 600 ms acquisition time in three groups of 200 ms. Figure 4.3 shows a schematic of the fitting procedure. The shear-rate is calculated from the spatial dependence of the flow by using a fourth order central difference formula in MATLAB to approximate the derivative of the flow velocity. To calculate the cross-sectional flow rate, the velocity values are integrated using trapezoidal numerical integration.

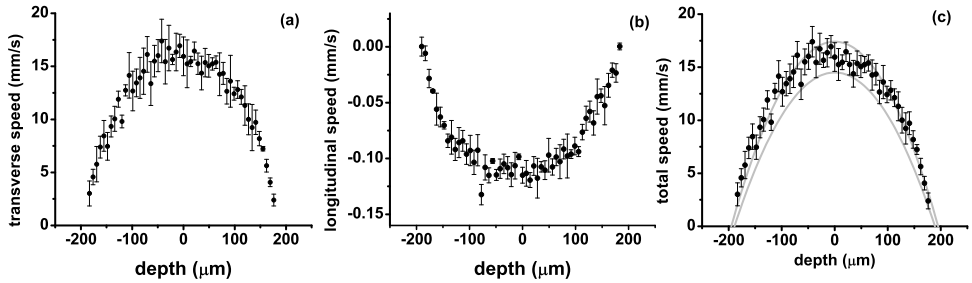

Figure 4.4: Measured flow velocities at the center of the flow channel: (a) transverse flow velocity, (b) longitudinal flow velocity, and (c) total flow velocity. The parabolae show the confidence interval of the reference flow velocity calculated based on the set-point of the mass-flow controller and the measured channel depth and width.

4.3 Results

First, we present measurements of the flow velocities at the center of the channel before the bacteria solution is seeded into the system. This serves as a reference case to demonstrate the changes in flow velocity profiles as the biofilm growth progresses inside the channel. Figures 4.4(a-b) show the depth resolved transverse and longitudinal flow velocity components, respectively and Fig. 4.4(c) shows the magnitude of the total flow velocity calculated as $v_{\text{total}} = (v_t^2 + v_z^2)^{\frac{1}{2}}$. The negative sign of the longitudinal flow velocity component indicates the direction at which the tracer particles are moving in the z-direction. It should be noted that the measured transverse flow velocity lacks directionality (cf. Eq. 4.1). The parabolas in Fig. 4.4(c) show the confidence interval of the reference flow velocity calculated based on the set-point of the mass-flow controller and the measured channel dimensions. The measured total flow velocity is in good agreement with the reference velocity. Due to variations of the channel geometry caused by manufacturing tolerances and imperfections, the longitudinal axis of the channel is not guaranteed to be perpendicular to the propagation direction of the imaging beam. This results in the local longitudinal flow velocity at a particular point in the channel to be non-zero.

Second, we present measurements of the channel morphology and flow velocities as biofilm growth progresses. Figure 4.5 shows a representative cross-section of the flow channel in the $(y, z)-$plane. The first column shows the reference case where the channel is filled only with the suspension of tracer particles. The second and third column show the channel morphology and flow velocities after 24 and 48 hours of seeding the bacteria solution, respectively. The transverse (second row) and longitudinal (third row) flow velocities show a smooth parabolic flow profile. The growth of the biofilm at the walls of the flow channel is seen in the OCT images as a clear increase in the biofilm thickness as the experiment progresses. Biofilm growth occurs predominantly on the side and bottom PDMS walls of the channel and less on the top glass wall. Correspondingly, the transverse and longitudinal flow velocity profiles change in magnitude, where a clear increase of the maximum flow velocity is observed. The flow shape when compared to the reference case is no

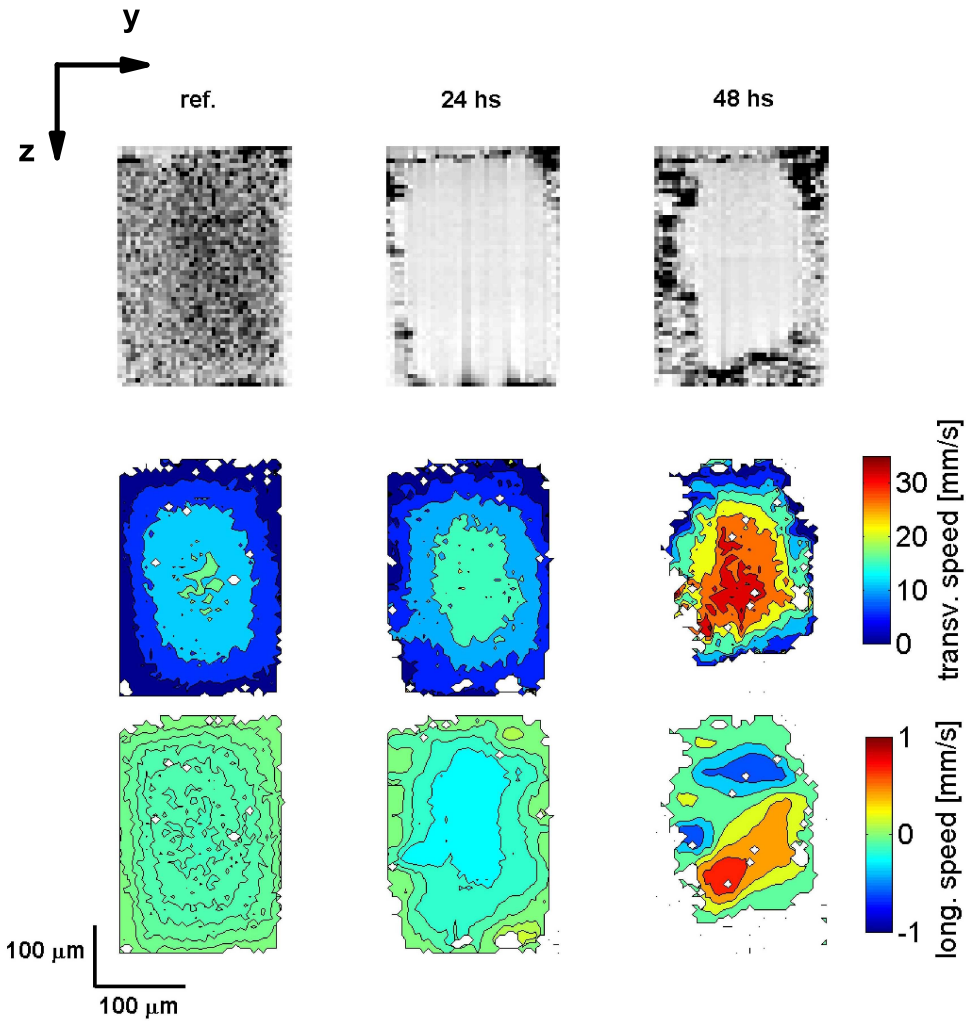

Figure 4.5: Channel morphology and longitudinal and transverse flow velocities in the (y, z)-plane. The first row shows the channel morphology, the second row shows the transverse flow velocity and the third row shows the longitudinal flow velocity. The first column shows the reference data, and the second and third column show the data after 24 and 48 hours after starting the experiment, respectively. The scale of the flow velocity is the same for all three cases. The points where the velocity estimation algorithm did not converge are shown in white.

longer parabolic and a shift of the maximum flow velocity away from the center of the channel is observed for the transverse flow velocity. Additionally, a clear change in the direction of the longitudinal flow velocity is seen after 48 hours of growth.

To quantify biofilm growth, we calculate the ratio of biofilm volume to channel surface area ($\mu m^3_{biofilm}/\mu m^2_{substratum}$) based on the type of data shown in the first row

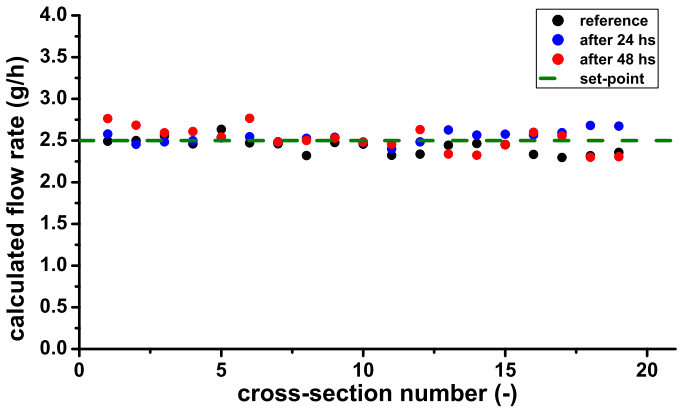

Figure 4.6: Flow rates through the cross-section of the flow channel calculated by numerically integrating the measured velocity data. The dashed line shows the set-point of the mass-flow controller.

of Fig. 4.5. We do this for the two days of measurements. For the biofilm volume calculations we filtered the biofilm morphology data using a binary mask. In the location where we observe the biofilm we set the index to 1 and all other locations are set the index to 0. We do this for 20 cross-sections. Then we calculate the total number of elements with a value of 1 and multiply the sum with the voxel size. The channel surface area was calculated by multiplying the perimeter by the distance scanned in the x-direction. For determining the biofilm locations we select a threshold based on the gray-scale intensity picture. This results in a biofilm to surface area of 0.4 $\mu m^3_{biofilm}/\mu m^2_{substratum}$ after 24 hours and 1.4 $\mu m^3_{biofilm}/\mu m^2_{substratum}$ after 48 hours.

Based on the velocity and the channel morphology both quantified with our OCT based method shown in Fig. 4.5 the total flow rate through the channel cross-section is calculated. Figure 4.6 shows the results of the numerical integration of the flow velocity data for the reference measurement, for the measurement after 24 hours of growth and for the measurement after 48 hours of growth. Each data point represents a different cross-section of the channel separated by 5 µm. The data shown in Fig. 4.5 corresponds to the fifth cross-section. The calculated flow rate is in good agreement with the flow rate set-point of the mass-flow controller of 2.5 ± 0.05 g/h.

Third, we present results on the calculated shear-rates based on the velocity data shown in Fig. 4.5. Figures 4.7 and 4.8 show the shear-rate in the $(y, z)-$plane for the transverse and the longitudinal flow velocities, respectively. As before, in both figures the first column shows the reference data, and the second and third column show the data after 24 and 48 hours, respectively. The first row shows the shear-rate in the y-direction (dv/dy) and the second row shows the shear-rate in the z-direction (dv/dz). As the experiment progresses, for both velocity components, the shear-rate increases. This is attributed to the combined effect of the increase in the flow velocity and biofilm growth reducing the cross-section of the flow channel.

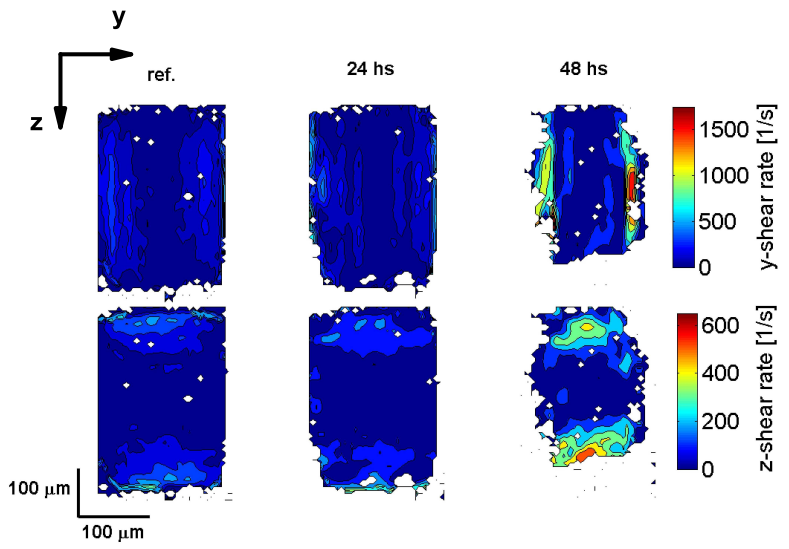

Figure 4.7: Calculated shear-rate in the $(y, z)-$plane for the transverse flow velocity component corresponding to the velocity data shown in Fig. 4.5. The first row shows the shear-rate in the y-direction and the second row shows the shear-rate in the z-direction. The first column shows the reference data, and the second and third column show the data after 24 and 48 hours after starting the experiment, respectively.

Due to the aspect ratio of the channel, the shear-rate in the y-direction is larger than the shear-rate in the z-direction.

4.4 Discussion

Our results show that using an OCT and a microfluidic platform biofilm growth and the underlying transverse and longitudinal flow velocities can be accurately measured.

Here, we have calculated the longitudinal flow velocity v_z using the Doppler shift carried by the phase of the complex-valued OCT signal. In principle, a determination of v_z by fitting the autocorrelation function of the complex OCT signal is possible [59], however in this way the sign of the longitudinal velocity is lost. Further, due to the relation between the transverse velocity v_t and the autocorrelation function in Eq. 4.1, we are only able to measure the absolute value of v_t. By introducing a velocity bias by scanning the imaging beam with, e.g., a galvanometric mirror, the sign of the transverse velocity can be measured [57]. In principle, the same method can be applied to resolve the transverse flow velocity in its elementary component v_x and v_y. However, this would result in prolonged measuring times for each location of the flow channel.

In the experiments presented here we have used a Coriolis mass-flow controller to drive the flow through the microfluidic channel at a constant rate. Since bacteria attachment is naturally not restricted to the flow channel of interest, but takes place

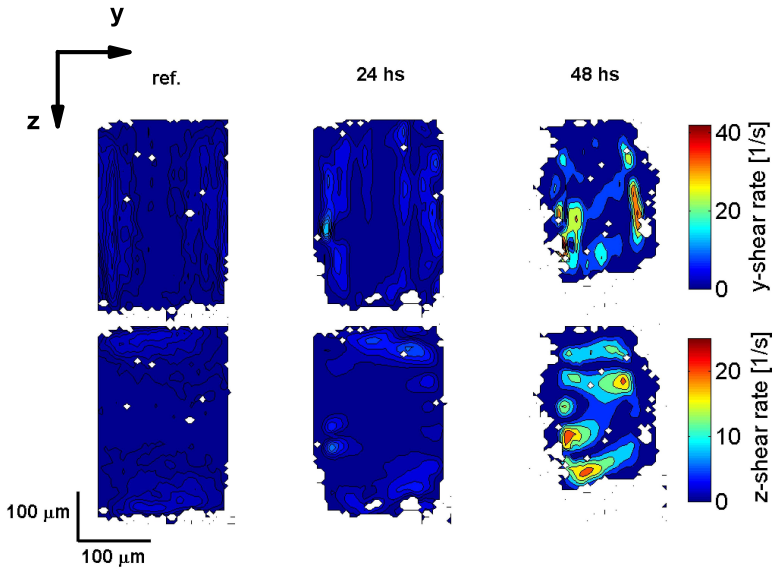

Figure 4.8: Calculated shear-rate in the $(y, z)-$plane for the longitudinal flow velocity component corresponding to the velocity data shown in Fig. 4.5. The first row shows the shear-rate in the y-direction and the second row shows the shear-rate in the z-direction. The first column shows the reference data, and the second and third column show the data after 24 *and* 48 *hours after starting the experiment, respectively.*

in all tubing and valves of the system, we observed that the performance of the stability of the mass flow controller decreases for the later stages of the experiment. We attribute this to the bacteria attachment to the tubing and valve of the mass flow controller. However, for the flow velocity measurements in the first 48 hours the input flow was stable.

Our results show that as bacteria attaches to the walls of the channel, biofilm thicknesses down to 10 µm can be clearly detected based on the OCT magnitude images. However, due to the lack of scattering of the original bacteria suspension, tracer particles were used to measure the underlying flow velocities. In order to reduce unwanted interactions of the tracers with the biofilm and the flow system, the tracers were coated with polyethylene glycol (PEG). For this work we assumed minimized biofilm-particle interactions due to the PEG coating [85, 86]. The duration of the presence of tracers inside the flow channel is minimized by the duration of the OCT based flow measurement. Optimization of the scan mechanism of the imaging beam can further reduce the duration of the presented flow measurement as well as limit the interaction of the tracers with the biofilm.

We have shown that determination of the flow velocities with high spatio-temporal resolution allows for an accurate determination of the shear-rates inside the flow channel. This approach allows for the direct observation of the dynamic deformations of the biofilm surface due to shear-stress [77]. This is important for the study of biofouling processes, e.g., for the production of drinking water [72]. For

the current study, we have chosen a relatively simple geometry of the flow channel. To study more complex phenomena, such as e.g., the formation of biofilm streamers [51], curved channel structures or channels with features along the flow direction can be used. Furthermore, the presented approach can be further combined with numerical modeling to study physical and biochemical processes. In order to do this, biofilm OCT images can be used to extract structural templates to serve as boundary conditions to solve Navier-Stokes and mass-transport equations [87].

4.5 Conclusion

We have presented simultaneous and localized measurements of the longitudinal and transverse flow velocities and quantified biofilm growth in a microfluidic channel using optical coherence tomography. We have shown that there is a clear relation between the measured flow velocity data and the biofilm morphology. We anticipate that the presented methodology will improve the quantification and understanding of the influence of flow parameters such as channel geometry and local flow driving biofilm growth dynamics.

CHAPTER 5

Doppler-based lateral motion tracking for optical coherence tomography

Abstract

Non-uniform lateral scanning of the probe beam in optical coherence tomography produces imaging artifacts and leads to a morphologically inaccurate representation of the sample. Here, we demonstrate a solution to this problem which is based on the Doppler shift carried by the complex-valued depth-resolved scattering amplitude. Furthermore, we demonstrate the feasibility of Doppler flow velocity measurements in underlying flow channels while laterally scanning the imaging probe over large surfaces with arbitrary and varying velocity. Finally, we performed centimeters-long hand-held B-mode imaging of skin *in-vivo*.

This chapter has been published as:

- N. Weiss, T.G. van Leeuwen, and J. Kalkman, "Doppler-based lateral motion tracking for optical coherence tomography," Opt. Lett. **37**, 2220-2222 (2012).

5.1 Introduction

Optical coherence tomography (OCT) is an imaging technique in which low coherence interferometry is used to produce depth dependent back scatter profiles from tissue (A-lines). By lateral scanning the OCT beam or the tissue, high resolution cross-sectional images of tissue are obtained. As OCT systems generally operate at constant A-line rates, a uniform velocity sweep across the sample yields an ensemble of A-lines that are uniformly sampled in space, resulting in a morphologically correct image. In general, scanning of the OCT probe beam is performed with galvanometric scanners that can achieve high frequency, constant velocity sweeps, with large duty cycles. However, their lateral scan range is limited to several millimeters.

Manual scanning of the imaging probe has been proposed as an alternative method for lateral scanning. However, contrary to galvanometric scanning, in manual scanning OCT, A-lines are no longer sampled uniformly in space due to the non-uniform velocity. Yet, by determining the non-uniform relative displacement trajectory of the scanning probe, the raw OCT image can be spatially resampled to construct a morphologically accurate image of the sample. In [88] the relative displacement is determined based on the correlation of adjacent A-lines. Consequently, this approach relies on *a priori* knowledge of the sample structure and its scattering properties. In [89] the relative displacement is measured with an external optical monitoring system that consists of a tracking camera and identification markers attached to the imaging probe to track its position during image acquisition. While this approach allows for a complete estimation of the position and orientation of the imaging probe, its main drawback is that the OCT system becomes more complex and expensive, and dependent on a direct line of sight between the monitoring camera and the OCT probe. Here, we propose to estimate the relative displacement based on the intrinsic OCT signal.

5.2 Materials and methods

Assuming a solid sample with stationary scatterers, the Doppler shift, measured at depth z and time t, quantifies the velocity of the moving probe over a sample. The probe velocity is approximated by [44]:

$$v(z,t,t+T) = \frac{\lambda_c}{4\pi n \cos\theta} \frac{\arg\left[a_{\mathrm{OCT}}(z,t) a^*_{\mathrm{OCT}}(z,t+T)\right]}{T} , \tag{5.1}$$

where λ_c is the center wavelength of the source, n is the refractive index of the sample, θ is the angle between the optical axis of the probe and the direction of motion, T is the time period between two adjacent A-lines, and $a_{\mathrm{OCT}}(z,t)$ is the complex-valued depth resolved scattering amplitude. The one dimensional displacement trajectory of the probe is calculated by numerically integrating (5.1). Then, the ensemble of A-lines defined by $|a_{\mathrm{OCT}}(z,t)|$ is resampled from a uniform time axis to a uniform displacement axis thus correcting for the image distortion caused by the non-uniform lateral scan velocity. We assume that the velocity measurements $v(z,t,t+T)$ are uncorrelated random variables with identical standard deviations, a linear interpolation of (5.1), and a shot noise limited detection. Then, the minimum

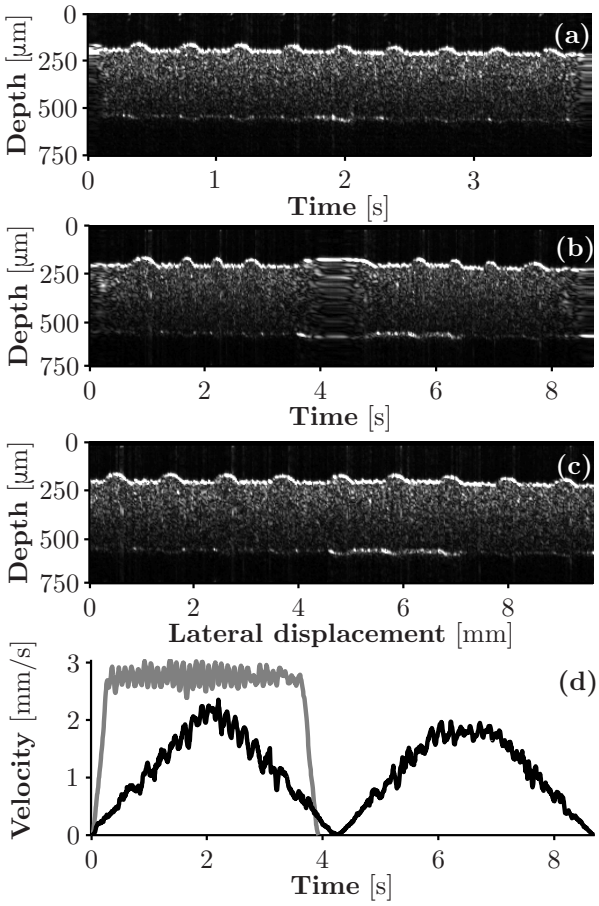

Figure 5.1: Doppler-based lateral motion tracking of a tissue phantom: (a) Quasi-uniform motion and control image. (b) Non-uniform motion plotted in a uniform time axis showing lateral motion artifacts. (c) Non-uniform motion resampled into a uniform displacement axis, lateral motion artifacts are corrected. (d) Measured stage velocities of (a) and (b). Note that the high frequency oscillations are typical for lead screw translation stages.

displacement error is written as [44]:

$$\Delta x(t+T) = \frac{\lambda_c}{2\sqrt{2}\pi n \cos\theta}\sqrt{N}\Delta\phi \ , \tag{5.2}$$

with N the number of A-lines acquired during time $t+T$ and $\Delta\phi$ the phase stability of the OCT system.

We implemented the displacement estimation technique in a home-built spectral-domain OCT system operating at a center wavelength $\lambda_c = 1300$ nm and an A-line acquisition rate $f_A = 16.846$ kHz [29]. To illustrate the effects of non-uniform scanning, we performed OCT imaging of a silicon-based tissue phantom with a constant pitch ridge pattern [90] that was placed on a motorized translation stage (Zaber T-LS28-M) and was programmed to move with uniform and non-uniform

velocities. The velocity was measured at a depth of 250 μm beneath the surface of the tissue phantom. For all measurements the angle θ in (5.1) is calibrated by translating the stage a known distance and equating the calculated and programmed distances.

5.3 Results and discussion

Figure 5.1(a) shows a morphologically correct OCT image of the tissue phantom acquired by translating the stage with quasi-uniform velocity. Figure 5.1(b) shows the same tissue phantom measured with a non-uniform velocity. The corresponding velocity profiles are shown in Fig. 5.1(d). It can be observed that the pitch of the ridge pattern decreases in areas where the scan velocity was relatively high and that it increases in areas of relatively low velocity. The computed displacement trajectory is used to resample the ensemble of A-lines from a uniform time axis into a uniform displacement axis, yielding a morphologically correct B-mode image of the phantom shown in Fig. 5.1(c).

The displacement error is characterized by scanning five times over 5953 μm of the phantom. The mean measured displacement is 5950 ± 6 μm which is in good agreement with the 5.5 μm accuracy of the translation stage [91]. The error given by (5.2) for these scans is 0.6 μm with a measured $\Delta\phi = 1.6$ mrad, $N = 224200$, $\theta = 82.76°$, and $n = 1.36$.

A tissue phantom with homogeneously distributed stationary scatterers represents an idealized case. However, since the method relies on Doppler information available from discrete depths within the sample, it allows for the continuous acquisition of flow velocity profiles of moving particles and the simultaneous measurement of the lateral movement of the probe beam. To illustrate this, we measured the three-dimensional flow profile in a tissue phantom containing a flow channel in which a 1 vol.% Intralipid (Fresenius Kabi) solution was flowing. B-mode OCT images were acquired by translating the stage with quasi-uniform velocity across the flow channel. In this configuration, the total Doppler shift is a vectorial sum of the shift generated by the flowing particles and the shift produced by the moving stage. Figure 5.2(a) shows a segment of a B-scan of the tissue phantom with the flow channel. Figure 5.2(b) shows the lateral velocity profiles taken at two depths indicated with arrows. By accounting for the movement of the stage from depths close to the surface, the correct flow profile is reconstructed with zero flow velocity outside the flow channel.

As an application of the presented technique we performed a hand-held B-mode acquisition of *in-vivo* skin of one of the author's ventral forearms. A spacer with a large glide surface was added to the sample arm to fix the distance between the objective lens and the surface of the skin and to maintain a constant angle during scanning. The raw and resampled OCT images are shown in Fig. 5.3. A clear reduction in the image artifacts can be observed after resampling the ensemble of A-lines with the corresponding displacement trajectory measured near the surface. The extent of the lateral displacement axis, calculated based on the Doppler shift, compares well with a direct measurement of the total displacement of 59 ± 5 mm.

During *in-vivo* hand-held skin measurements, abrupt accelerations are observed

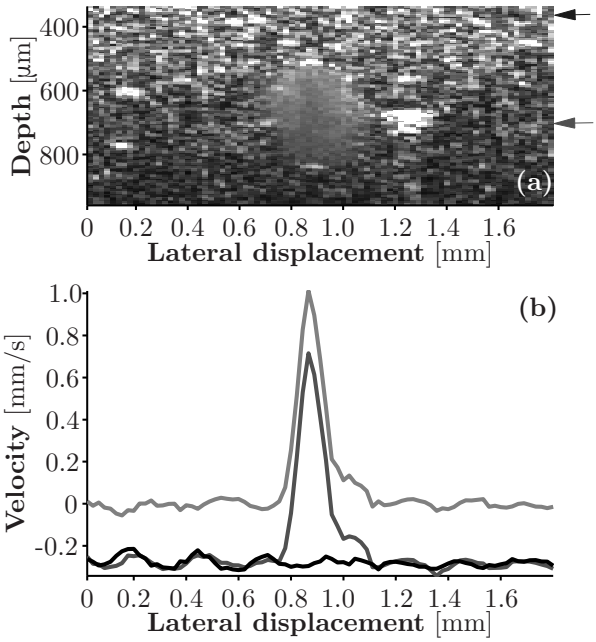

Figure 5.2: (a) OCT image of the tissue phantom with a channel with flowing Intralipid solution. (b) Velocity while translating the stage, measured through the flow channel (dark gray line/arrow) and measured at a shallower depth (black line/arrow). The flow profile is calculated by subtracting both signals (light gray line).

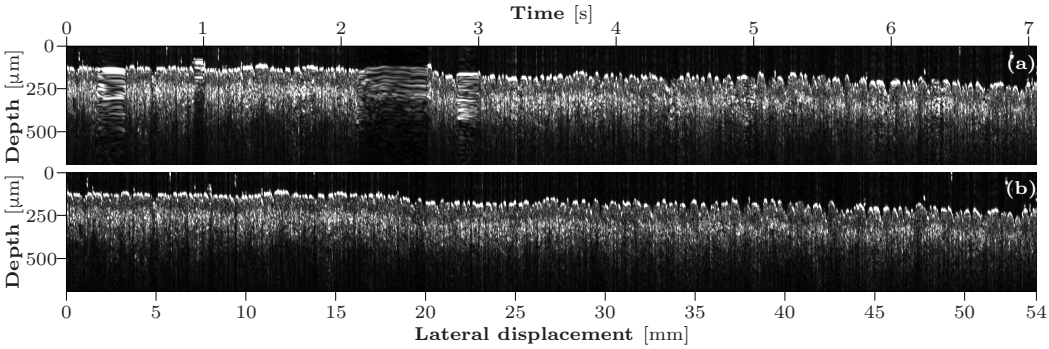

Figure 5.3: Hand-held B-mode OCT image of the skin of the ventral forearm: (a) B-scan plotted in a uniform time axis. (b) B-scan resampled and plotted in a uniform displacement axis correcting for the lateral scanning artifacts caused by the non-uniform motion of the OCT probe.

which degraded the accuracy of the displacement measurement. We believe that these originate from the friction between the elastic skin and the imaging probe. A solution to this problem is the use of refractive index matching media or ultrasound gel to reduce the friction at the probe-skin interface, which has the additional advantage to reduce OCT image artifacts such as intensity distortions [92].

The method presented here is accurate and simple, but suffers from problems generally associated with integration-based estimation methods and with Doppler OCT such as accumulation of errors, phase wrapping at high velocities [42], a decrease of lateral resolution, and a decrease of signal-to-noise ratio [37]. In general, these problems can be solved by using higher acquisition rates. More importantly, in the current implementation of the Doppler-based motion tracking only one component of the two-dimensional velocity vector in the plane of motion of the probe is measured. Nevertheless, as long as the orientation of the probe relative to the direction of motion and the angle θ in (5.1) remain constant during the image acquisition procedure, morphologically correct images are obtained. The full velocity vector can be obtained by combining the Doppler shift of two OCT beams or by determining the magnitude of the velocity vector using, e.g., decorrelation techniques [93]. Lastly, the assumption that the refractive index is constant at a fixed depth is not met for *in-vivo* applications.

5.4 Conclusion

In conclusion, we demonstrated a simple method to accurately measure the displacement trajectory of a moving OCT probe based on the depth-resolved phase information. The experiments demonstrate that the information carried by the OCT signal fully suffices for the correction of images from non-uniform lateral scanning artifacts, as well as for continuous large scale B-mode acquisition of morphologically correct images and flow.

CHAPTER 6

Photonic force phase imaging

Abstract

We report on a method to measure the height profile of non-scattering soft (biological) samples in liquid environments using a combination of optical tweezers and optical coherence tomography. An optical tweezer is used to trapped a 3 μm in diameter polystyrene sphere that is used as a probe to scan the surface of a sample. A phase-sensitive optical coherence tomography system is used to detect the backscattered radiation from the probe. In this way, the measured displacement of the probe is used to measure the height profile of the sample with nanometer resolution. The method is validated by measuring the height profile of a silicone mold of a precision diffraction grating. As an application example for profilometry of soft non-scattering samples we measured the height profile of a smooth muscle mouse aorta fixed cell.

This chapter contains unpublished data.

6.1 Introduction

The established technique to measure the height profile of samples at sub-μm resolution is the Atomic Force Microscope (AFM) [94]. AFM can achieve resolutions in the order of 1 Åusing cantilever spring constants in the order of 0.1 . . . 1 N/m. When measuring soft biological material using a sharp AFM tip in combination with relatively high spring constants can result in damage of the sample. Moreover, the application of AFM in liquid environments is not straightforward. A solution to this problem is presented by the Photonic Force Microscope (PFM) [95]. In PFM, an optical tweezer is used to trap a dielectric particle and probe the surface of a sample. Typically, the forward scattered light of the trapped particle is used to measure the position of the particle inside the trapping volume. In the case that the trapped particle interacts with a sample, the trapped particle will be deflected and the variations in the scattered intensity can be used to measure the height profile of the sample. This principle is similar to AFM, however the spring constants involved are two to three orders of magnitude smaller than those of the AFM cantilever [96]. Furthermore, the PFM probe is easier to characterize when compared to the AFM cantilever.

Typically, the forward scattered and unscattered radiation by the probe particle trapped in an optical tweezer is detected by using a quadrature photodiode [96]. The integrated intensity over each detector quadrant can be related to the three-dimensional position of the particle. However, the intensity detection dynamic range is typically limits the position detection to 400 nm in the propagation direction of the trapped beam and 200 nm in the transverse direction for a 1064 nm trapping laser [96].

Here, we report on a method based on optical coherence tomography (OCT) to measure the displacement in the propagation direction of the trapping beam of an optically trapped dielectric particle. We use the high sensitivity of the phase of the OCT signal to quantify the height profile of a non-scattering silicone diffraction grating and a fixed smooth muscle mouse aorta cell.

6.2 Materials and methods

The experiments are performed with a fixed stage microscope (BX51WI, Olympus) and a home built fiber-based swept-source OCT system. A schematic of the experimental set-up is shown in Fig. 6.1. The optical tweezer set-up is built around the microscope and is based on a 1070 nm laser (IPG Photonics), a beam expander (BE02-05C, Thorlabs), an acousto-optic deflector (DTD-274HD6M, IntraAction), and a water immersion microscope objective (UPlanApo 60x/1.20w, Olympus). The probes used in the experiment are polystyrene spheres with a diameter of 3 μm (Thermo Scientific). The OCT system operates at a center wavelength of 1312 nm with a bandwidth of 92 nm and a sweep frequency of 50 kHz (Axsun Technologies). The average output power is 20.9 mW and the duty cycle is 59.4%. Data is sampled (ATS9350, AlazarTech) with an interferometrically derived external clock signal at equidistant wavenumber intervals. To ensure phase stability each sweep is triggered by the signal of a fiber Bragg grating centered at 1266 nm (OE Land) [42]. The in-

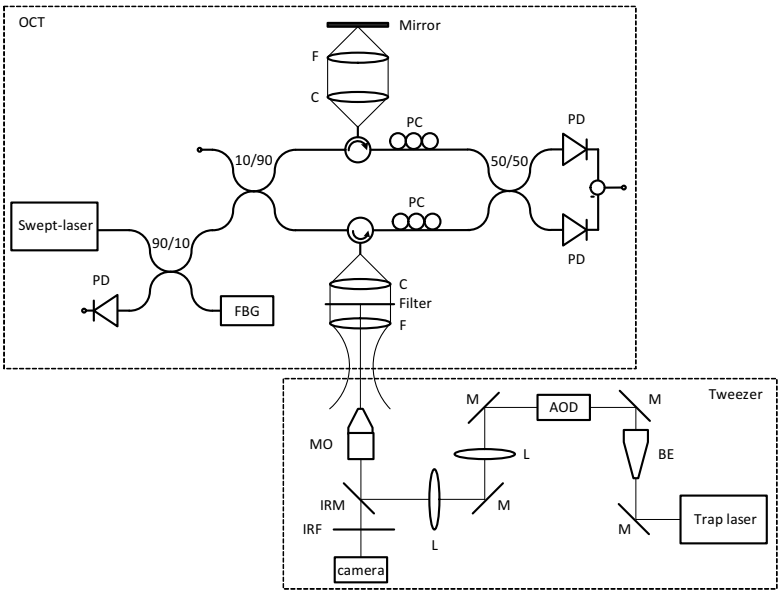

Figure 6.1: Schematic of the OCT and optical tweezer set-up. PD: photodetector, FBG: fiber Bragg grating, PC: polarization controllers, C: collimating lens, F: focusing lens, M: mirror, AOD: acusto-optical deflector, IRF: infra-red filter, IRM: infra-red mirror, and MO: microscope objective.

6

terferometric signal is detected with a 150 MHz balanced photodetector (PDB450C, Thorlabs) and a 80 MHz low-pass filter (VLF-80+, Mini-Circuits). The trigger signal is detected with a 125 MHz photodetector (1811, New Focus). The optics of the sample and reference arms are composed of a collimating lens (PAF-X-18-C, Thorlabs) and an achromatic doublet focusing lens (AC254-040-C, Thorlabs) with a numerical aperture of 0.04. The power ratio of the sample and reference arms is 90/10. We measured $w_x = 10.8 \pm 0.2$ µm and $w_z = 8.1 \pm 0.3$ µm in air with a mirror reflector. The refractive index of the medium is $n = 1.32$. To isolate the high-power beam from the optical tweezer from OCT-set-up a long-pass filter was used (67299, Edmund Optics).

A silicone grating is fabricated by making a negative mold of a precision diffraction grating (53006BK01-942R, Richardson Gratings) using the recipe described by de Bruin *et al.* [90]. The diffraction grating has 14.3 grooves/mm and a blaze angles of 3.33°.

The minimum measurable longitudinal displacement is determined by the phase stability of the OCT system [42]. Here, we quantify the phase stability as the standard deviation of 1000 time adjacent acquisitions of the complex-valued OCT signal generated by a trapped bead. The phase stability $\delta\phi$ is related to the longitudinal displacement δz by [42]:

$$\delta z = \frac{\lambda}{4\pi n}\delta\phi \ , \tag{6.1}$$

with λ the center wavelength of the source and n the refractive index of the medium.

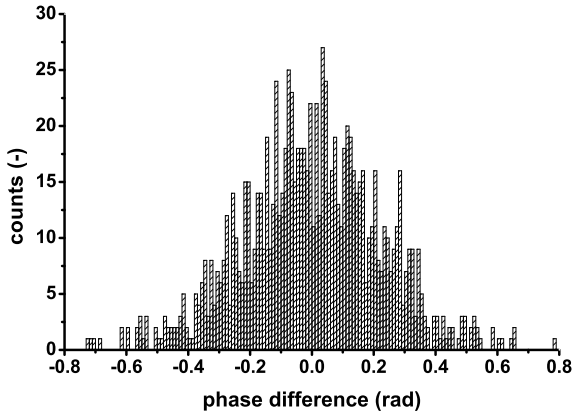

Figure 6.2: Histogram of the phase difference of the OCT signal from a trapped bead.

6.3 Results and discussion

Figure 6.2 shows a histogram of the measured phase difference from the OCT signal of a single trapped sphere. The calculated standard deviation of the phase values is 225 mrad. Using Eq. 6.1 results in a minimum measurable longitudinal displacement of 17.8 nm.

As a validation experiment we measured the profile of a silicone grating. Figure 6.3(a) shows a schematic of the experiment. The sphere is trapped on the surface of the silicone grating. The transversal displacement was generated by moving the silicone grating with a mechanical stage. As the silicone grating moves under the trapped sphere, the longitudinal movement of the sphere following the shape of the grating is measured by the OCT signal. Fig. 6.3(b) shows the measured longitudinal displacement of the trapped bead. The measured height of the grating is 3.5 μm. When compared to the height of the original grating there is a difference of 0.55 μm. This is attributed to imperfections in the production of the silicone mold. A further issue that should be taken into account is the finite size of the probe sphere when measuring steep walls. This can be overcome by using, e.g., triangular probes [95]. Figures 6.3(c) and (d) show microscopy images of the trapped sphere and the silicone grating corresponding to the positions shown by the arrows in Fig. 6.3(b).The difference in the grating height can also be seen by the sphere appearing out-of-focus in Fig. 6.3(d).

As an application example for profilometry of soft non-scattering samples we measured the height profile of a smooth muscle mouse aorta fixed cell. The experimental arrangement is analogous to the previous. The measured cell height profile is shown in Fig. 6.4. The inset shows a microsopy image of the cell and the probe sphere resting on its surface.

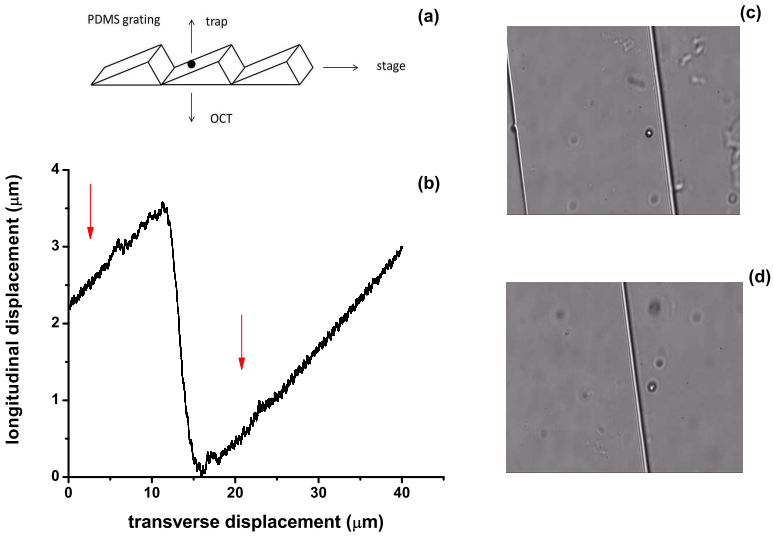

Figure 6.3: (a) Schematic of the experiment. The probe sphere is trapped from the top and is imaged from the bottom. The silicone gratings is move transversely by an electro-mechanic stage. (b) Measured longitudinal displacement of the trapped sphere. The arrows correspond approximately to the positions shown in (c) and (d).

6.4 Conclusion

We have combined optical tweezers and optical coherence tomography to measure the height profile of soft and non-scattering samples. Our experimental results show that by using the phase of the optical coherence tomography signal we are able to resolve sub-μm features of (biological samples). We anticipate that the presented method opens up new opportunities to measure profiles of non-scattering and soft samples in liquid environments.

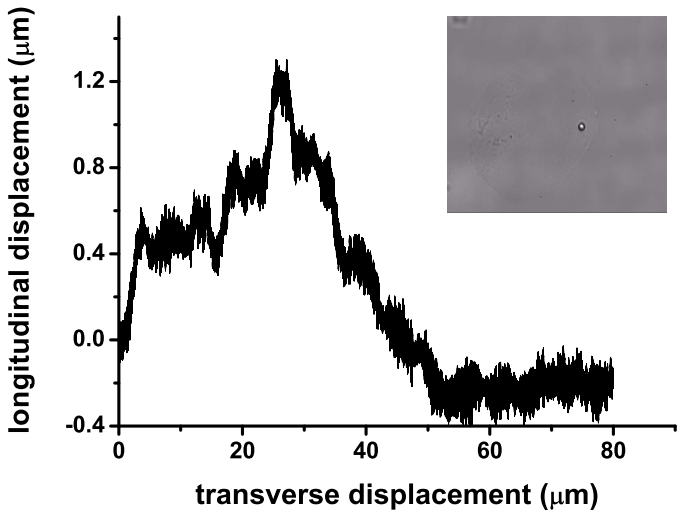

Figure 6.4: Measurement of the longitudinal displacement of the probe sphere as a fixated cell is transversely moved by the stage. The inset shows and image of the cell and the probe sphere.

CHAPTER 7

Concluding remarks

In this thesis, we have studied the influence of sample dynamics on a low-coherence interferometric signal measured by optical coherence tomography (OCT). Although, each chapter in this thesis is accompanied by its own conclusion section, here, we re-visit the main findings of this thesis. We have addressed two particular problems. First, we have studied the fluctuations caused to the OCT signal by directional (flow) and random (diffusion) motion of colloidal suspensions. In order to quantify this, we developed a theoretical model based on the complex-valued autocorrelation function of the OCT signal. For dynamical systems with directional and random motion, the autocorrelation function is governed by three characteristic decay term: an exponential decay corresponding to diffusion, a Gaussian decay corresponding to the flow velocity component transverse to the propagation direction of the imaging beam, and finally a Doppler term corresponding to the flow velocity component parallel to the propagation direction of the imaging beam. From the data and knowledge gathered in these studies we draw the following general conclusions:

1. The OCT autocorrelation function developed in Chapter 2 allows for an accurate and precise measurement of the flow velocity in a colloidal suspension. However, at high longitudinal shear-rates and flow non-perpendicular to the imaging beam, the distribution of Doppler frequencies over the coherence detection gate has to be accounted for. Neglecting to do so, results in an overestimation of the flow velocity component transverse to the propagation direction of the imaging beam.

2. In Chapter 3 we show that the OCT autocorrelation function can be used to simultaneously measure flow and diffusion. The regime where both dynamic parameters can be reliably estimated is determined by the diffusion coefficient of the sample, the local flow velocity, and the Gaussian beam waist of the imaging beam. The sensitivity by which the flow velocity component transverse to the propagation direction of the imaging beam is estimated can be improved by using a higher numerical aperture objective in the OCT sample arm. However, this comes at the expense of a decrease in the precision and accuracy of the estimation of the diffusion coefficient.

3. If the decorrelation due to the flow velocity component transverse to the propagation direction of the imaging beam is interpreted solely as a transit time effect, the OCT autocorrelation function should only depend on the local Gaussian beam radius. However, in Chapter 3 we have experimentally shown that the decorrelation time depends only on the Gaussian beam waist, i.e., the beam radius at the focus of the Gaussian beam.

4. The ability of OCT to locally measure sample morphology and flow velocity simultaneously and in single measurement, makes OCT a promising technique to study biological systems in microfludic devices. The high temporal resolution in the order of tens of microseconds allows OCT to resolve transient effects such as biofilm detachment processes.

5. When studying bacterial systems in microfluidic devices, such as in Chapter 4 of this thesis, care should be taken in the choice and concentration of tracer particles. A relatively large concentration of tracer particles is necessary for sufficient signal-to-noise ratio. However, this will cause an increased and mostly unwanted interaction between the tracers and the biological system. Therefore, a compromise must be made between the signal-to-noise ratio and the degree of interaction requirements.

6. Besides the limitations inherent to the OCT autocorrelation function presented in Chapters 2-4 the autocorrelation approach to measuring dynamics has the disadvantage of requiring relatively long measurement times. This is due to the fact that the calculation of the autocorrelation function relies heavily on averages. The use of light sources with a higher sweep rates would not help in this case, since the time extent of the autocorrelation function is determined by the acquisition time length of the signal. In Chapter 8 we explore possible solutions to this problem.

7. The combination of optical tweezers and OCT presented in Chapter 6 allows for the measurement of the longitudinal displacement of a trapped probe independent of the transverse displacement and with a longer dynamic range when compared to conventional detection schemes based on quadrature photodiodes.

Second, we have studied the effect of non-uniform sample motion on OCT images. In Chapter 5 we have shown that when the spatial sampling of the OCT signal is performed over a non-uniform spatial grid, the resulting OCT magnitude image presents contraction and dilation artifacts. Furthermore, we have shown that based only on the Doppler shift measured by the phase of the OCT signal we are able to reconstruct the (non-uniform) trajectory of the sample and correct for these image artifacts. From the data and knowledge gathered in this study we draw the following conclusions:

1. The OCT signal carries in principle sufficient information to correct for non-uniform spatial sampling artifacts as experience during OCT hand-held image acquisition.

2. In order to use the Doppler shift to reconstruct the sample absolute lateral displacement, the Doppler angle should be known and constant during the entire image acquisition process. This can be achieved by tilting the OCT probe at a specific angle as was done in the experiments in Chapter 5.

3. If the absolute lateral displacement is of no interest, the value of the Doppler angle is not required to reconstruct the images. However, the Doppler angle should remain constant during the scan.

4. The path-length resolution of the OCT signal allows for a reliable measurement of flow velocities of sub-surface flow channels, even in the presence of bulk probe or sample motion.

5. In combination with the first chapters of this thesis and in the case of a variable or unknown Doppler angle, the OCT autocorrelation function approach can be used to calculate the transverse velocity of the probe and to correct the OCT images.

CHAPTER 8

Outlook

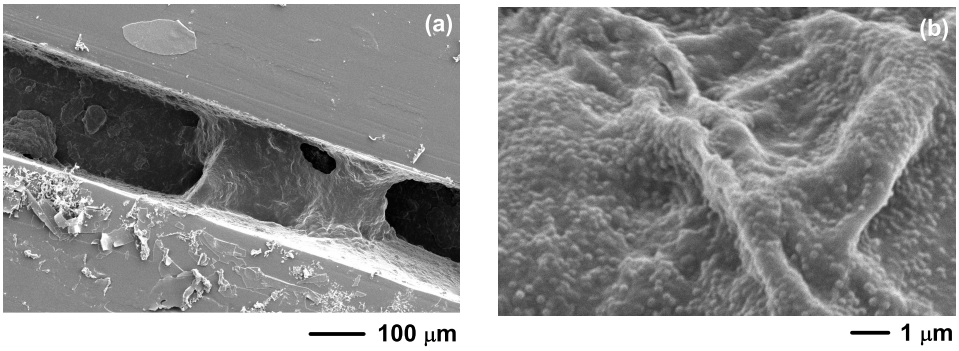

Figure 8.1: (a) Scanning electron microscopy image of the dehydrated biofilm grown during the experiments reported in Chapter 4. (b) Zoomed-in view of the biofilm and the attached tracer particles. Images courtesy of K. El Tayeb El Obied, University of Twente.

In this thesis we have developed, validated, and applied a model based on the autocorrelation function of the OCT signal to measure the dynamics of a sample. Besides the limitations and advantages of the autocorrelation function discussed in those chapters, one additional drawback of this approach is the relatively long measurement times required. The minimum length of time that the OCT signal is to be acquired is determined by the upper limit of the time decay rates of the autocorrelation function. This, in turn, is determined by the slowest dynamic process in the sample. For a colloidal suspension, this is given by the Brownian motion of the particles. More precisely, for the samples measured in this thesis, this was in the order of 1.5 to 3 ms. However, in practice, the OCT signal is acquired longer to perform averaging and to increase the signal-to-noise ratio of the measurement (e.g., 200 ms in the experiments described in Chapter 3). For applications with time constraints, such as *in-vivo* measurements or for the biofilm application presented in Chapter 4, a shorter measurement time is preferable. To illustrate this, in Fig. 8.1 we show scanning electron microscopy images of the dehydrated biofilm grown during the experiments reported in Chapter 4. Figure 8.1(a) shows the microfludic channel and the biofilm and Fig. 8.1(b) shows at higher magnification more details of the biofilm surface. The small spheres visible on the biofilm surface (diameter ~ 0.2 μm) are tracer particles that attached to the biofilm's surface in the course of the experiment. Based on these images it becomes clear that, if one is solely interested in studying

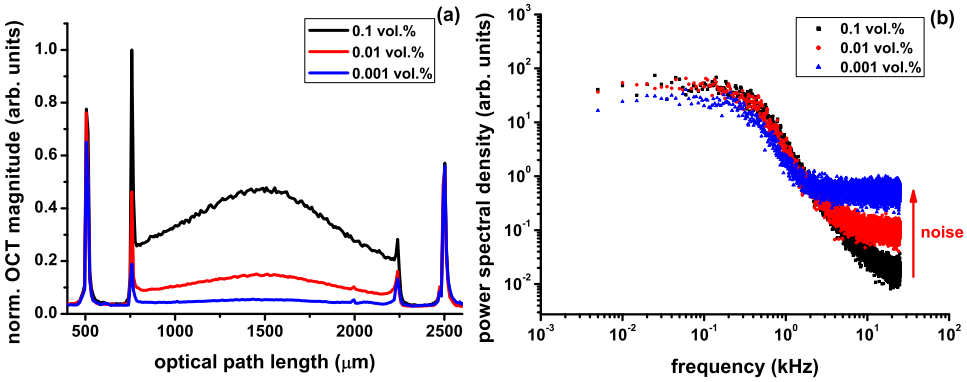

Figure 8.2: (a) Amplitude of the OCT signal for three different concentrations of tracers and (b) the corresponding power spectral densities. The noise clearly increases with decreasing tracer concentration.

biofilm growth, the interaction with the tracer particles is to be kept to a minimum. In this Outlook chapter we report on three possibilities to achieve this.

The first approach is straightforward and is to reduce the tracer concentration to minimize the number of tracers interacting with the biofilm. However, this would reduce the signal-to-noise ratio of the OCT measurement and therefore, assuming constant measurement time, increase the influence of noise in the autocorrelation function. In Fig. 8.2(a) we show how the amplitude of the OCT signal increases with increasing tracer concentration. The increase of noise due to a reduction in signal-to-noise ratio at the high frequencies of the power spectral density[1] is shown in Fig. 8.2(b). A detailed treatment of the effect of noise on the OCT autocorrelation function can be found in Ref. [58].

The second approach is to reduce the total measurement time by reducing the number of time samples used to calculate the time lags of the autocorrelation function. A reduction in the amount of time that the tracers are present in the channel, will reduce their total interaction with the biofilm. At this point, we re-visit the definition of the autocorrelation function of Chapter 1 in its time discrete form[2]:

$$g(m) = \sum_{n=0}^{N-m-1} s(n+m)s^*(n)\,, m \in [0; N)\,,$$

where m is the discrete time lag, and N is the total number of time lags. If we assume here for simplicity of the argument that $N = 4$, then we can write the individual

[1] The power spectral density is the Fourier transform of the autocorrelation function [16].

[2] Note that we have only written here the expression for positive time lags, however, by symmetry of the autocorrelation function, $g(-m) = g(m)$, for all time lags m [16].

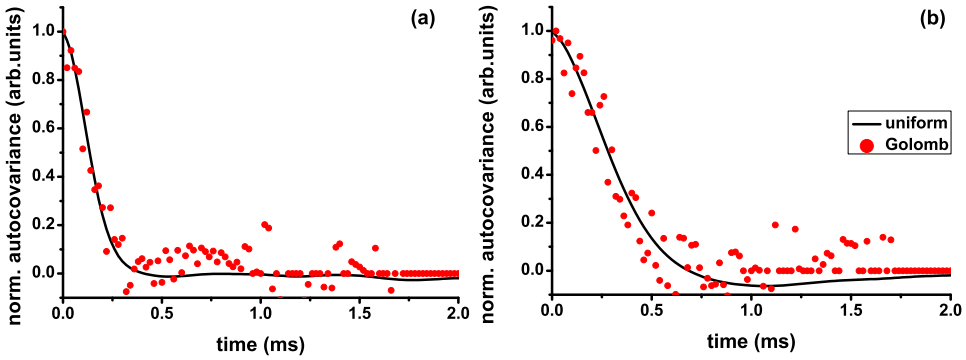

Figure 8.3: Autocovariance function of the amplitude of the OCT signal for a flowing suspension of polystyrene spheres. (a) and (b) show data for two different flow velocities. The solid line shows the autocovariance calculated using 1000 time uniform samples and the dots show the autocovariance calculated using a Golomb ruler with 12 non-uniform time samples. Note that averaging was the same for both cases.

terms of the autocorrelation function as:

$$
\begin{aligned}
g(0) &= s(0)s^*(0) + s(1)s^*(1) + s(2)s^*(2) + s(3)s^*(3)\,,\\
g(1) &= s(1)s^*(0) + s(2)s^*(1) + s(3)s^*(2)\,,\\
g(2) &= s(2)s^*(0) + s(3)s^*(1)\,,\\
g(3) &= s(3)s^*(0)\,.
\end{aligned}
$$

It becomes clear now that, for all time lags $m \leq N-2$, a single autocorrelation value $g(m)$ is calculated as the sum of all possible realizations of the particular time lag m. Here, with the aim of reducing the total measurement time, we propose to drop the redundancy in the calculation of the autocorrelation function by choosing a reduced subset of time sample in $[0;N)$. Continuing with the previous example for $N=4$, we write all four terms of the autocorrelation function g by using only the time discrete samples with index {0,1,3}:

$$
\begin{aligned}
g(0) &= s(0)s^*(0) + s(1)s^*(1) + s(3)s^*(3)\,,\\
g(1) &= s(1)s^*(0)\,,\\
g(2) &= s(3)s^*(1)\,,\\
g(3) &= s(3)s^*(0)\,,
\end{aligned}
$$

such that the signal value at $s(2)$ is not used. The time indices given by vector $\{0,1,3\}$ is called a Golomb ruler [97]. Golomb rulers provide a scheme to sample the autocorrelation function uniformly, based on a non-uniform time sampling of the underlying signal. Golomb rulers have been applied previously to radar applications [98] and radio astronomy [99] and we have applied them here to calculate the OCT autocorrelation function based on a reduced number of time samples of the OCT signal. Figure 8.3 shows a plot of the OCT autocovariance data of a flowing suspension of polystyrene spheres for two different velocities calculated using 1000

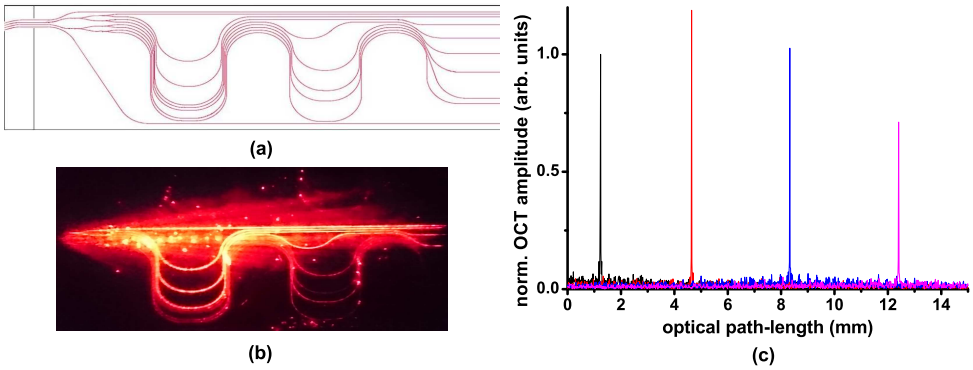

Figure 8.4: (a) Lay-out of a parallel OCT chip with 8 sample channels based on Y-splitters (image and design by LioniX BV). (b) Microscope image of the parallel OCT chip fabricated on TriPleX technology with light coupled from a 635 nm laser. (c) Normalized OCT amplitude measured using the first four channels of the parallel OCT chip and a mirror as a sample.

(uniformly sampled) time samples of the OCT amplitude (solid line) and calculated using a Golomb ruler using 12 (non-uniformly sampled) time samples of the OCT amplitude[3]. The data is taken from a data set acquired in the experiments reported in Chapter 3. As expected from the lack of redundancy (averaging) in the individual terms of the autocorrelation function the data calculated using the Golomb ruler is noisier but is, nonetheless, in good agreement with the data calculated using the uniform time samples.

8

The third approach is based on measuring multiple lateral sample points simultaneously and therefore reducing the total time required to measure a sample. Typically, OCT generates path-length resolved measurements in the propagation direction of the imaging beam. A swept-source OCT system, as described in this thesis, produces 544 path-length (or depth) measurements simultaneously at a rate of 50 kHz. However, the imaging area in the plane perpendicular to the propagation direction of the imaging beam is given by the diameter of the (Gaussian) imaging beam which is typically in the order of 10 to 20 μm. If a larger scan area is needed, then the imaging beam is typically scanned with a galvanometric mirror. This results in a sequential acquisition of the different sample points in the transverse direction. An alternative to this approach would be to have a plurality of OCT sample arms scanning different points of the sample simultaneously. Although a conventional fiber-based OCT system would be unsuitable due to space and cost constraints, integrated optics-based-OCT presents a promising alternative [101]. In Appendices A-C we report on three different approaches for an integrated-optics-based OCT interferometer, based on TriPlex, silicon, and silicon oxynitride technologies. The extension of these approaches to accommodate a plurality of sample arms in combination with dynamic sample parameter estimation is a promising topic for future research. As a proof-of-concept we show in Figs. 8.4(a-b) a parallel OCT chip

[3]For the interested reader, the optimal Golomb ruler of length 12 and order 85 used for Fig. 8.3 is: {0,2,6,24,29,40,43,55,68,75,76,85} and was taken from Ref. [100].

design based on integrated optics. The chip consists of 8 sample channels realized with Y-splitters. The signal of each sample channel is separated by introducing an increasing path-length delay between the individual sample channels. Figure 8.4(c) shows the response of the first 4 OCT sample arms to a mirror sample. The distance between the different signal peaks corresponds to the on-chip length difference of the individual waveguides.

The amplitude and the phase: Developments beyond this thesis

From an experimental point of view, the range of applications of the developed approach for the OCT autocorrelation function are not restricted to the few cases presented in this thesis. Recently, other research groups have applied the OCT autocorrelation to measure red-blood cell flux in capillary networks [102], to image *in-vivo* stroke injury [103], to measure Cilia driven flow [104], to correct for rotational distortion in catheter-based OCT [105], to measure viscosity in middle ear effusions [106], and to measure microfludic volumetric flow [107].

From a theoretical point of view, the relatively simple model presented in Chapter 2 has been further developed to resolve the directional ambiguity in the determination of the transverse flow velocity [57], to achieve improved velocimetry using a Bayesian approach [108], to include the influence of noise [58], to include the influence of the imaging optics [109], and to include explicitly the theoretical relation between the longitudinal velocity gradient and the autocorrelation function [110].

Appendices

APPENDIX A

Integrated-optics-based swept-source optical coherence tomography

Abstract

We designed, fabricated, and characterized an integrated-optics-based swept-source optical coherence tomography (SS-OCT) system in TriPleX technology. An external 1300 nm swept source is coupled to the chip, which contains waveguide structures for interferometric depth ranging and balanced detection. The complete OCT chip has a footprint of 0.4 cm $\times$ 1.8 cm. Light from the chip is focused onto the sample using an aspheric lens; the lateral resolution is 21 ± 1 μm. OCT measurements, performed with a moveable mirror, demonstrate a sensitivity of -80 dB and imaging up to the maximum depth of 5.09 mm. Corrected for dispersion, the measured OCT axial resolution of 12.7 ± 0.5 μm is in good agreement with the bandwidth limited resolution. Finally, we demonstrate cross-sectional OCT imaging of a multilayered tissue phantom over the whole depth range with the integrated-optics-based SS-OCT system.

This chapter has been published as:

- V. Duc Nguyen[1], N. Weiss, W. Beeker, M. Hoekman, A. Leinse, R.G. Heideman, T.G. van Leeuwen, and J. Kalkman, "Integrated-optics-based swept-source optical coherence tomography," Opt. Lett. **23**, 4820-4822 (2012).

[1]VDN was financially supported by the Smart Mix Program of the Netherlands Ministry of Economic Affairs and the Netherlands Ministry of Education, Culture, and Science.

A.1 Introduction

Optical coherence tomography (OCT) is an interferometric imaging technique that can make high resolution images up to a few millimeters deep [1]. Currently, OCT has its main applications in ophthalmology and intravascular imaging. Still, the widespread use of OCT in medicine and in other application areas, such as forensics, biometrics, and process control, is held back by its high costs and its large form factor. Integrated optics has the potential to make OCT devices and components significantly smaller, more functional, and more cost efficient [111].

Recently, we designed and fabricated integrated-optics components for OCT, such as elliptic couplers [112] and AWG spectrometers [113, 114], and demonstrated their use in spectral-domain OCT.

Compared to spectral-domain OCT, swept-source OCT (SS-OCT) has the advantage of a simpler optical design and larger imaging depth [115]. Recently, Yurtsever *et al.* [116] presented an integrated-optics interferometer in silicon on insulator and performed SS-OCT depth ranging. Yet, the measured OCT axial resolution was not bandwidth limited and the signal-to-noise ratio (SNR) was too low for imaging of turbid media. In this work, we demonstrate the design, fabrication, and characterization of an integrated-optics-based SS-OCT system and demonstrate cross-sectional OCT imaging of a multilayered tissue phantom.

A.2 Materials and methods

An optical chip containing waveguides is produced in TriPleX technology platform [117] and the waveguide geometry is a single strip Si_3N_4 of 50 nm height and 3.4 μm width. The top and bottom SiO_2 cladding layers are 8 μm thick. Waveguides operate in single mode at 1300 nm wavelength and have a minimum bending loss for TE polarization. At the end facets of the chip waveguides are tapered down to 1 μm to match the mode field diameter (9.2 μm) of a standard single mode fiber (SMF-28) to achieve optimal fiber-to-chip coupling. Waveguide splitters are made using directional couplers (DCs). A schematic of the on-chip waveguide layout and the experimental setup is shown in Fig. A.1(a). The chip contains a Michelson interferometer, sample arm, reference arm, and two identical DCs for light splitting and balanced detection. The optical path length of the reference arm is chosen such that the zero delay point is 6.9 mm away from the edge of the chip. A single OCT chip is only 0.4 cm × 1.8 cm.

The integrated-optics-based SS-OCT is compared to a home-build bulk optics SS-OCT system shown in Fig. A.1(b) [59]. Both integrated-optics-based and bulk SS-OCT systems use an Axsun swept source with a center wavelength of 1312 nm, 20.9 mW average output power, 50 kHz repetition rate, and ∼ 50% duty cycle. The start of the wavelength sweep is detected using the light reflected from a fiber Bragg grating (FBG) at $\lambda = 1266$ nm (OE Land). For both systems the interference spectrum is detected on a balanced photo detector (Thorlabs, PDB450C). The signal from the FBG triggers a 500 MHz digitizer (Alazar Tech, ATS9350) that acquires 1088 samples using the Axsun k-clock as an external clock signal. The 1088 clock cycles are equivalent to 92 nm of optical bandwidth corresponding to a maximum

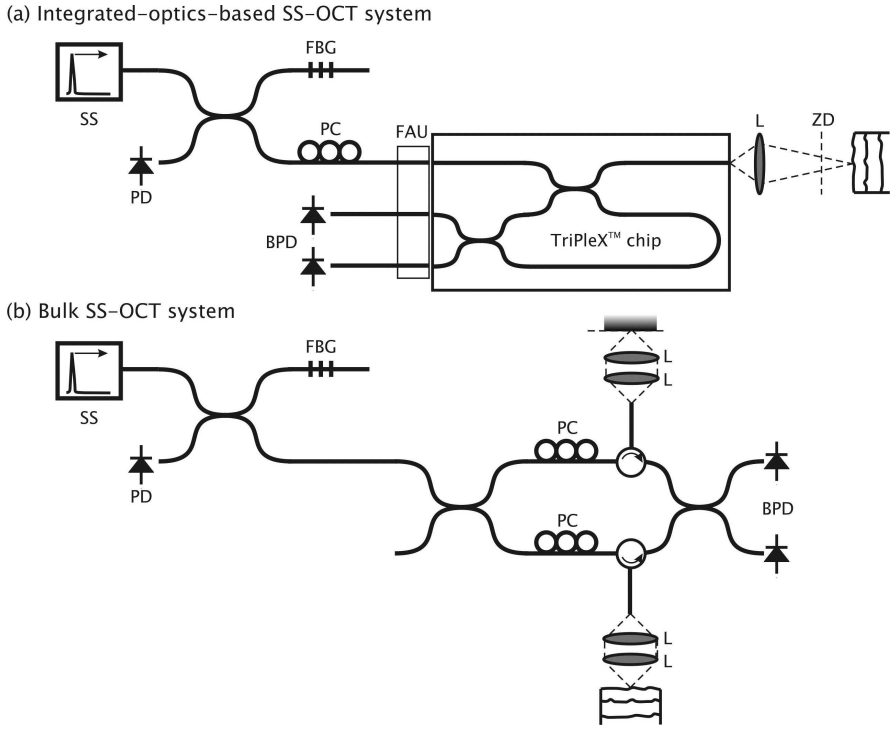

Figure A.1: Schematic of the experimental setup used for (a) the integrated-optics-based SS-OCT and (b) the bulk SS-OCT system. SS, swept source; FBG, fiber Bragg grating; FAU, fiber array unit; PC, polarization controller; BPD, balanced photo detector; L, lens; PD, photodiode; and ZD, zero delay.

imaging depth of $z_{\max} = 5.09$ mm. OCT depth scans are generated by Fourier transformation of the interference spectrum. To correct for dispersion differences between the sample and reference arm, the spectrum is resampled using a second-order dispersion correction in the wavevector versus frequency relation [118], while keeping the total optical bandwidth fixed.

The bulk SS-OCT system is based on a 90:10 fiber optic splitter with 90% of the light going to the sample arm and 10% going to the reference arm. The two arms of the interferometer are fully symmetric to avoid any dispersion mismatch. Light from the sample and reference arm are mixed and split by a 50:50 splitter for balanced detection.

In the integrated-optics-based SS-OCT system, light from the swept source is coupled into the chip via a fiber array unit (FAU) based on SMF-28 fibers with 127 µm pitch. A polarization controller is placed on the input fiber of the FAU to couple TE polarized light into the chip. In the chip, light is split into sample and reference arm by the first DC. In the sample arm, light from the waveguide is focused onto the sample by an aspheric lens (Geltech 355200). Back-reflected light from the sample goes again through the first DC and is recombined with light from

the reference arm in the second DC. There, it is split and coupled into two fibers of the FAU that are connected to the balanced detector. In all measurements, unless indicated otherwise, the focus position is set to 0.5 mm after the zero delay point. For this focus position the measured NA of the lens is 0.020 ± 0.001, corresponding to a lateral resolution of 21 ± 1 μm.

A.3 Results and discussion

The measured splitting ratio of the DC is 80:20 at the center of the wavelength band (1312 nm) with 80% of the light going to the bar port and 20% of the light going to the cross port [101]. The splitting ratio varies from 90:10 (1266 nm) to 75:25 (1358 nm) over the source spectrum. Ideally, both DCs split the light in a ratio of 50:50 independent of wavelength; however, due to fabrication errors this ideal splitting ratio was not reached.

Figure A.2 shows the OCT signal in depth measured for a moveable mirror in the sample arm. The raw OCT signal in Fig. A.2(a) shows poor axial OCT resolution for all depths. After dispersion correction at every depth the OCT signal increases and the axial resolution improves Fig. A.2(b), same vertical scale as in Fig. A.2(a). We measured the back-reflected light intensity from the mirror in the sample arm. After correcting for the OCT signal dependence on field and correcting for the SS-OCT system sensitivity roll-off in depth, we obtain a signal decrease as shown by the solid curve in Fig. A.2(b). As can be observed, the decrease of the OCT signal in depth is well described by the combined effects of SS-OCT system sensitivity roll-off in depth and lens focusing. The OCT axial resolution is determined by taking the full width at half-maximum of the OCT signals in Figs. A.2(a) and (b) and is shown in Fig. A.2(c). For all depths the dispersion mismatch between the waveguide material and air can be fully corrected. The measured average axial resolution of 12.7 ± 0.5 μm is in excellent agreement with the bandwidth limited axial resolution of 12.5 μm, which is calculated from the reference arm spectrum measured on one port of the balanced detector [113].

The OCT sensitivity is measured with the integrated optics-based SS-OCT using a glass plate as a reflector with 4% reflectivity in the sample arm. The measured SNR at a depth of 500 μm is 66 dB. This is 3 dB worse than measured with the bulk optics OCT system (SNR = 69 dB) using the same digitizer acquisition settings, sample, depth location, reference arm power, and sample arm power. From the glass reflectivity and the measured SNR we calculate the sensitivity of the integrated-optics based SS-OCT to be −80 dB.

As a demonstration of OCT imaging using the integrated-optics-based SS-OCT system, images of a layered tissue phantom are obtained by sample scanning. The tissue phantom consists of three layers of scattering medium ($\mu_s = 4$ mm^{-1}, refractive index $n = 1.41$) [113] interleaved with non-scattering tape. Figure A.3 shows OCT images of the tissue phantom at three different depth locations. For each depth location the dispersion correction is optimized and the focus position adjusted (500, 2500, and 3500 μm, for increasing depth location). All three scattering layers can be clearly observed at the three depth locations.

The measured −80 dB integrated-optics-based SS-OCT sensitivity is affected by

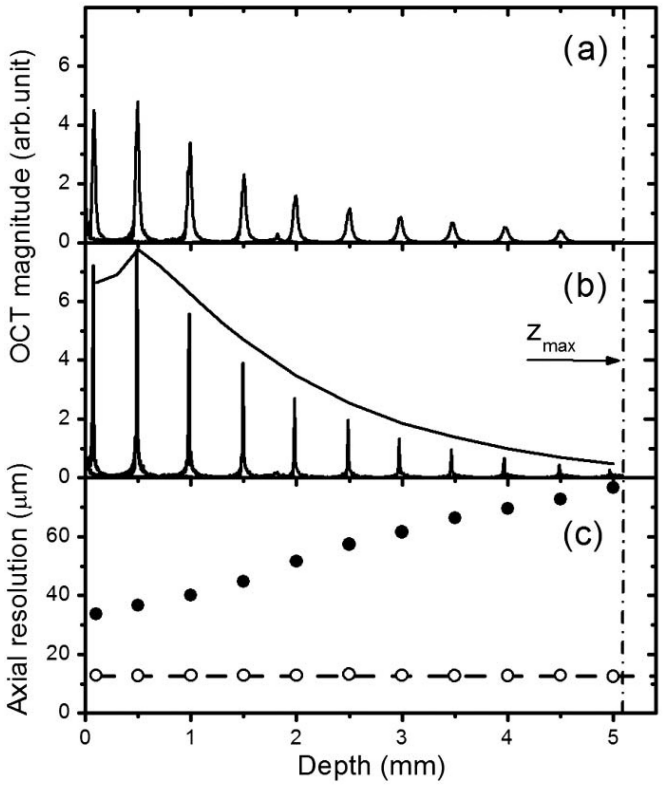

Figure A.2: Measured OCT signal in depth for a mirror in the sample arm. (a) OCT signal without dispersion correction and (b) OCT signal with dispersion correction. The solid curve indicates the SS-OCT signal drop due to system sensitivity and lens focusing. (c) Measured OCT axial resolution before (filled circles) and after (open circles) dispersion correction. The dashed line indicates the bandwidth limited OCT axial resolution and the vertical dashed dot line indicates the maximum imaging depth (z_{max}).

the following issues. (1) A measured 1.5 dB fiber-to-chip coupling loss and a 3.5 dB chip to fiber coupling loss, which is mainly due to FAU-to-chip misalignment and small offsets between the fiber and waveguide cores (typically 0.5 μm). In case of perfect alignment, fiber (round core) to waveguide (rectangular core) coupling loss is calculated to be 0.4 dB. (2) Unlike the bulk optics SS-OCT system, which collects most of the back-reflected light from the sample arm via a circulator, ideally, an integrated-optics-based SS-OCT with an 80:20 DC can only collect 16% of the back-reflected light from the sample (maximum 25% with a 50:50 DC), which leads to a 6.9 dB reduction in SNR compared to the bulk system. However, this issue can possibly be solved by incorporating an integrated-optics circulator into the chip design [119]. (3) The 80:20 splitting ratio is not constant over the entire bandwidth of the DCs, resulting in suboptimal balanced detection, which leads to a reduction in sensitivity [120]. We measured on the bulk SS-OCT system a 5 dB noise increase due to operating the digitizer at a higher voltage setting, necessary to handle the non-

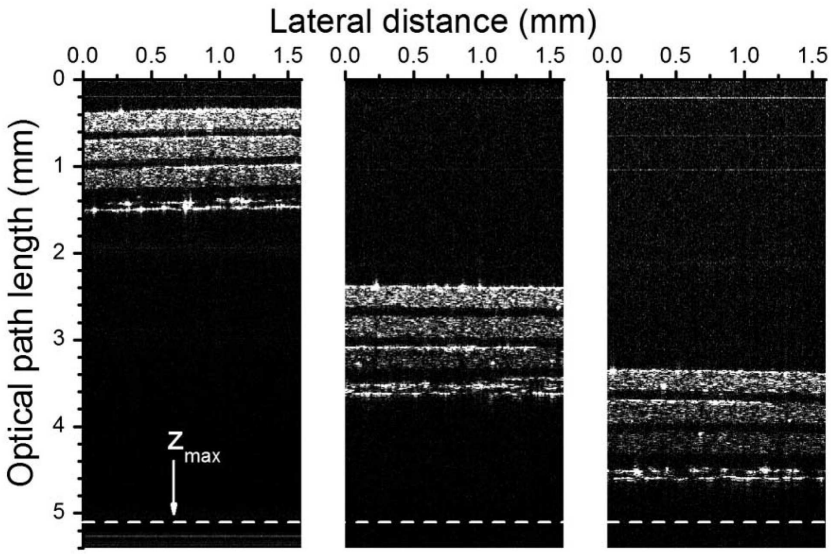

Figure A.3: OCT images of the tissue phantom measured with the integrated-optics-based SS-OCT system for three different sample depth locations

interferometric variation of the signal over the spectrum due to non-ideal balancing. However, we expect that these issues can be solved with the design and fabrication of a 50:50 wavelength-flattened DC [121]. Considering the aforementioned loss processes we estimate that the performance of the integrated-optics-based SS-OCT system can be improved by $10 - 15$ dB, bringing the performance of integrated-optics-based SS-OCT systems close to that of commercially available bulk SS-OCT systems.

A.4 Conclusion

In conclusion, we demonstrated the design and characterization of a 1300 nm integrated-optics based SS-OCT. Imaging of a layered tissue phantom with the integrated optics-based SS-OCT system demonstrates the feasibility of integrated-optics-based SS-OCT imaging.

APPENDIX B

Ultra-compact silicon photonic integrated interferometer for swept-source optical coherence tomography

Abstract

We demonstrate an ultra-compact silicon integrated photonic interferometer for swept-source optical coherence tomography (SS-OCT). The footprint of the integrated interferometer is only 0.75 $\times$ 5 mm^2. The design consists of three 2 $\times$ 2 splitters, a 13 cm physical length (50.4 cm optical length) reference arm, and grating couplers. The photonic integrated circuit was used as the interferometer of an SS-OCT system. The sensitivity of the system was measured to be -62 dB with 115 μW power delivered to the sample. Using the system, we demonstrate cross-sectional OCT imaging of a layered tissue phantom. We also discuss potential improvements in passive silicon photonic integrated circuit design and integration with active components.

This chapter has been published as:

- G. Yurtsever[1], N. Weiss, J. Kalkman, T.G. van Leeuwen, and R. Baets, "Ultra-compact silicon photonic integrated interferometer for swept-source optical coherence tomography," Opt. Lett. **39**, 5228-5231 (2014).

[1]GY was financially supported by Ghent University Methusalem project "Smart Photonic Chips".

B.1 Introduction

Optical coherence tomography (OCT) has become a standard tool for retinal imaging in the relatively short time since its invention [1]. During this period, the development of OCT has significantly benefited from the availability of optical fiber components developed for telecom applications. Currently, photonic integration in telecommunications is driven by the increasing demand for higher data bandwidth at a lower cost. Similarly, integrated photonics has the potential to reduce the size and the cost of OCT systems, which can open new opportunities for its deployment in various application areas.

Recently, various approaches to using integrated photonics for OCT have been studied. Akca *et al.* demonstrated an integrated spectrometer and a 2×2 splitter using silicon oxynitride (SiON) waveguides [122], albeit without on-chip integration of the reference arm. Nguyen *et al.* reported a Michelson interferometer using silicon nitride (Si_3N_4) strip waveguides. In this study, the reference arm was realized on chip [123]. However, the relatively short length of the reference arm did not encompass space for a sample arm galvo-scanner, and therefore the sample needed to be scanned to obtain cross-sectional images. More recently, Yurtsever *et al.* reported a Mach-Zehnder interferometer using silicon nitride (Si_3N_4) box-shaped waveguides with a long on-chip reference arm capable of accommodating a galvo-scanner in the sample arm [124].

In recent years, photonic integrated circuits based on silicon have gained substantial interest from the telecom industry. Silicon is one of the most developed material systems for microelectronic fabrication. Hence, using silicon as a platform for photonic integrated circuits enables the use of existing CMOS infrastructure and processing recipes developed for silicon microelectronics fabrication. Wafer-scale fabrication of silicon photonic integrated circuits using CMOS infrastructure [125] significantly reduces the price per chip. In addition to cost advantages, silicon waveguides have a very high confinement factor, which enables much smaller integrated photonic circuits than low-index-contrast material systems. In addition to miniaturization, significant reduction in size can enable faster, parallel OCT systems. Furthermore, several groups have also demonstrated that active components such as lasers, photodetectors, and modulators can be integrated on wafer-scale with silicon waveguides. A broad review of active component integration with silicon waveguides is presented by Park *et al.* [126]. In addition to active components, electronic and photonic integration can be combined on the same material system, which can further miniaturize electro-optical systems [127]. Thus, compared to other integrated photonic material systems, silicon can have a significant potential for mass fabrication of OCT devices, which would result in miniaturization, cost reduction, and wider deployment.

In this study, for the first time to the best of our knowledge, we demonstrate OCT imaging based on a silicon photonic integrated chip. The size of the chip is only 0.75×5 mm^2, which is 90 times smaller than the chip we previously demonstrated in silicon nitride (Si_3N_4) [124]. The chip consists of grating couplers, a 13 cm long (physical length) reference arm, and three 2×2 couplers in a Mach-Zehnder interferometer configuration. Using a swept light source, we obtained cross-sectional

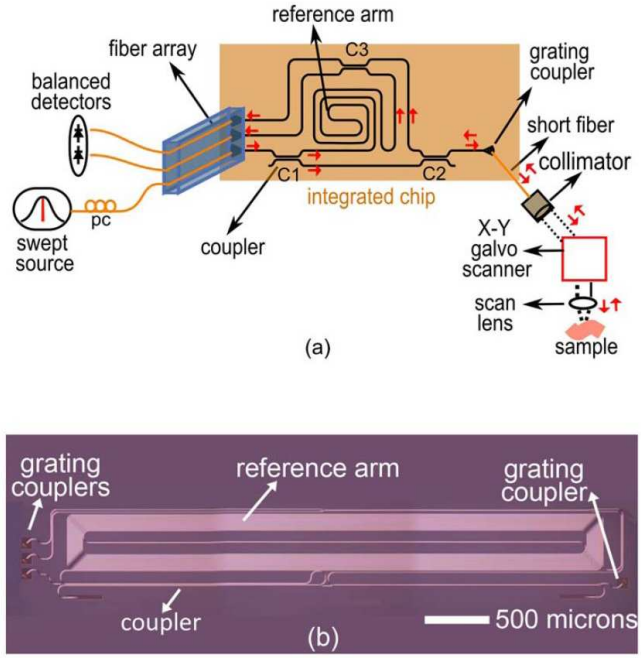

Figure B.1: (a) Schematic of the OCT setup with the photonic integrated circuit, pc: polarization controller; C1, C2, C3: 2×2 couplers. The direction of the light is indicated by red arrows. (b) Microscope image of the fabricated photonic integrated interferometer.

OCT images from a layered tissue phantom by scanning the beam with a galvo-scanner. Besides the design and the measurements, we discuss the challenges and potential improvements in silicon photonic integrated circuit design related to OCT imaging.

B.2 Materials and methods

An illustration of the OCT system used to perform the experiments is shown in Fig. B.1(a). Light from a swept source (Axsun Technologies, USA) centered at 1312 nm is coupled into the chip using an SMF-28 fiber array with a 127 μm pitch and 10° polish angle (OZ Optics, Canada). For long-term alignment stability, the fiber array was glued to the chip with UV curable glue. Coupling in and out of the chip is achieved with tilted grating couplers with reduced back reflection [128]. Grating couplers provide access to waveguides through vertical coupling. The polarization of the input light is adjusted to the TE-polarization since the grating couplers were designed for TE-light. After entering the chip, the light is split into reference and sample arms via the 2×2 coupler C1. In the sample arm, the light is split again by the 2×2 coupler C2 and finally sent out of the chip with a grating coupler. The light exiting the chip is coupled to a short piece of (2 cm) single-mode fiber (SMF), which is attached to a collimator (F280APC-C, Thorlabs, USA). The light

from the collimator is directed to the sample via the galvo-scanner and the scan lens. Back-scattered light from the sample is combined on the chip with the light from the reference arm at the 2×2 coupler C3. The combined light at both output arms of the 2×2 coupler C3 leaves the chip via grating couplers. The fibers in the fiber array aligned with these grating couplers send the light to a balanced photodetector (Thorlabs PDB 110C, USA).

A microscope image of the fabricated chip is shown in Fig. B.1(b). The single-mode rib waveguides are 470 nm wide, 220 nm high, and the bend radius is 50 μm. The loss of the straight waveguides is measured to be 0.35 dB/cm. The group index of the waveguides is $n_{\text{group}} = 3.88$ and hence the optical length of the reference arm is 50.4 cm. The designed circuit was fabricated on a 200 mm silicon-on-insulator (SOI) wafer consisting of 220 nm thick silicon on top of 2000 nm of buried oxide layer using 248 nm lithography. A single etch step of 70 nm was used for the definition of the waveguides and the grating couplers. To protect the chip from dust it was covered with silicon dioxide as a top cladding by using plasma deposition. The fabrication was performed through a cost sharing multi-project wafer service, ePIXfab silicon photonics platform.

To characterize the individual photonic integrated components, we measured the bandwidth of the grating couplers, the 2×2 couplers, and the power levels at the sample and reference arms. The grating couplers have 7.5 dB insertion loss and a 45 nm 3 dB bandwidth. For the 2×2 couplers, we chose to design adiabatic couplers as they have a broader bandwidth than directional couplers. Adiabatic couplers using both rib and ridge silicon waveguides have been experimentally demonstrated [129, 130]. In principle, couplers C1 and C2 can be realized using y-splitters, as they are wavelength independent. However, generally y-splitters have higher insertion losses than directional couplers and also cause some back reflection because of fabrication limited blunt at the junction. The length of the 2×2 couplers is 2.1 mm and the gap between the waveguides is 0.7 μm. Because of deviations between the designed and the fabricated geometry, the splitting ratio deviated from simulations; the measured splitting ratio was 45:55 at 1266 nm and 30:70 at 1356 nm.

The swept source has a 50 kHz repetition rate, 92 nm tuning range, and provides -6 dB roll-off at 3.5 mm depth. Each sweep cycle is sampled with 1088 points which corresponds to a 5.09 mm maximum imaging depth [59]. The power delivered to the chip was 12.4 dBm (17.5 mW), while the power on the sample was measured to be -9.4 dBm (115 μW), which means 21.8 dB attenuation compared to the input power. The attenuation results from the losses induced by the two grating couplers and the two 2×2 couplers. The power levels from the reference arm reaching the balanced photodetector were -14.7 dBm (36 μW) and -16.8 dBm (21 μW).

B.3 Results and discussion

Owing to their lower loss, the rib waveguides in this design (0.35 dB/cm loss) were preferred over ridge waveguides (2 dB/cm loss). However, the dispersion of these waveguides is significant; their group velocity dispersion was simulated to be -1700 ps/(nm·km) at 1310 nm. As dispersion of the reference arm cannot be compensated for in the sample arm, numerical dispersion compensation in software is

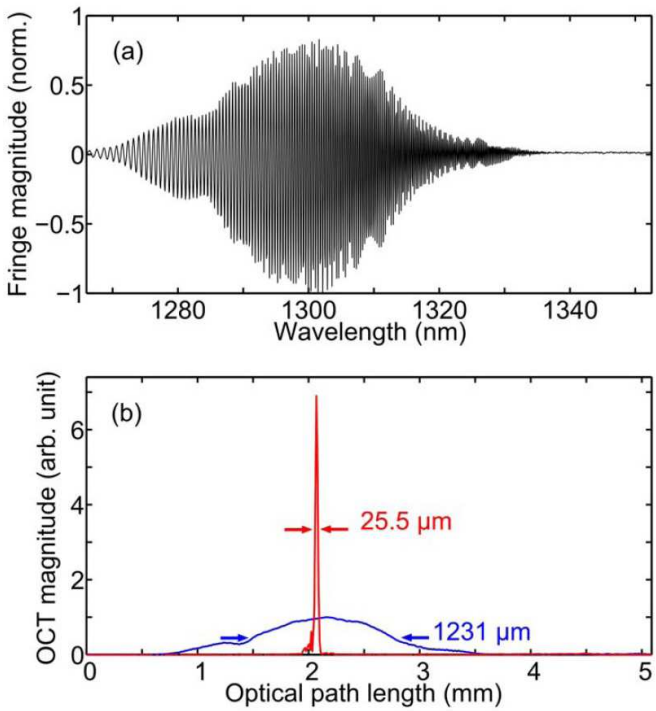

Figure B.2: (a) Interference fringe for a reflection from a mirror. (b) Fourier-transform of the interference signal, before (blue) and after (red) dispersion compensation. The peak of the blue line is normalized to 1.

necessary. For dispersion compensation, we first measured the reflection from a mirror in the sample arm. The measured interference fringe (Fig. B.2(a)) shows that the fringe frequency increases strongly with increasing wavelength. The measured bandwidth of the interference is reduced, compared to the source bandwidth because of the bandwidth of the grating couplers, which limits the axial resolution to 24.4 μm (FWHM) (obtained from the Fourier transform of the envelope of the interference signal). On the other hand, without dispersion compensation, the Fourier transform of the interference resulted in 1231 μm axial resolution as shown in Fig. B.2(b). To compensate for dispersion, we found the dispersion coefficients by fitting a third order polynomial to the phase obtained from the interference. After third order dispersion compensation [131], 25.5 μm axial resolution was obtained as shown in Fig. B.2(b). Compensation for dispersion orders higher than the third order did not further improve the axial resolution. The axial resolution of a fiber based OCT system using the same laser was 12.5 μm [59]. It should be noted that if the sample is placed close to the maximum imaging depth, aliasing will occur because of the large dispersion. The aliased signals cannot be compensated for dispersion and axial resolution and OCT signal amplitude near the maximum imaging depth will be degraded [132].

To characterize the sensitivity of the system, we placed an OD 1.2 neutral density

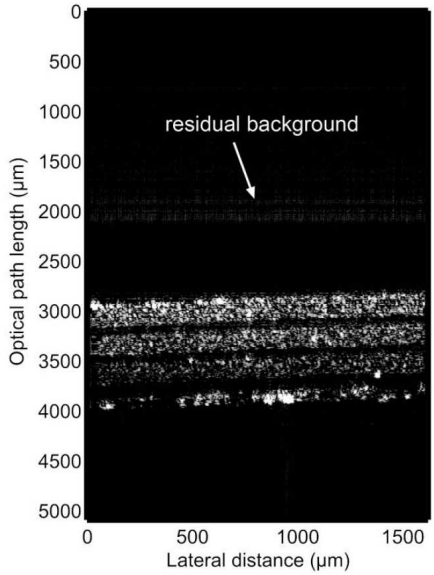

Figure B.3: OCT cross-sectional image (average of 100 B-scans) of a layered tissue phantom.

filter in the sample arm and measured the reflection from a mirror. The sensitivity of the system was calculated by the ratio of the amplitude of the OCT signal peak to the standard deviation of the noise floor. The sensitivity of the system with 115 μW power on the sample was measured to be −62 dB. We also measured the sensitivity of the fiber-based SS-OCT system [59] as −84 dB, using the same swept source, reference and sample arm powers, galvo-scanner, photodetector, and analog-to-digital converter card settings. Thus, the chip-based system had a 22 dB lower sensitivity than the fiber-based system. The degradation of the sensitivity can be explained mainly by the insertion losses in the grating couplers and an additional 3 dB loss of the 2×2 coupler C2 (while reflected light from the sample passes through the 2×2 coupler C2 and goes toward the photodetectors). Additionally, the 2×2 couplers of the fiber SS-OCT system (FC1310-70-50-APC, Thorlabs, USA) were significantly more wavelength independent than the on-chip 2×2 couplers and thus are better suited for balanced detection resulting in improved common mode noise reduction.

To demonstrate OCT imaging with the chip-based system, we imaged a three-layer tissue phantom as shown in Fig. B.3. The scattering layers of the phantom had a scattering coefficient $\mu_s = 4\ \mathrm{mm}^{-1}$, a refractive index $n = 1.41$, and were separated by non-scattering tape [79]. The image was obtained by averaging 100 B-scans. Near the middle of the image, a faint residual background signal as a result of internal reflections in the chip is seen. Because of laser power and phase fluctuations between each A-line, the background signal could not be completely removed by background subtraction. The residual background signal was observed only with the chip-based

system, and is absent in the fiber-based system. The phantom was placed slightly away from the residual background signal to prevent overlapping.

Although we demonstrated OCT imaging using the chip-based system, the sensitivity and axial resolution are relatively low compared to state-of-the art OCT systems. However, the sensitivity and the axial resolution can be significantly improved using more advanced fabrication methods to fabricate fiber to chip coupling structures with lower insertion loss and larger bandwidth. Simple grating couplers used in this study are easy to fabricate but are not the optimum solution. By using more advanced fabrication processes, grating couplers with 1.6 dB loss and 80 nm 3 dB bandwidth have been demonstrated [133]. For even larger bandwidths, a solution is to use horizontal butt-coupling using spot size converters to couple the light in and out of the chip. Spot size converters gradually enlarge the mode size in the waveguide and are usually fabricated as tapered waveguide structures. Ben Bakir *et al.* demonstrated 3×3 μm spot size converters with > 200 nm bandwidth and 1 dB insertion loss [134]. Coupling efficiently to such a small spot size converter with a lensed fiber is feasible. However, based on our experience, coupling efficiently to multiple adjacent small spot size converters may not be practical because of fabrication tolerances in lensed fiber arrays. Thus, spot size converters with low-loss coupling to standard SMFs are desirable. Shiraishi *et al.* demonstrated a spot size converter with 2.8 dB coupling loss to a standard SMF [135]. Further research on SMF spot size converters would increase the coupling tolerances and reduce packaging costs, and improve OCT performance.

In general, high index contrast integrated waveguides are much more dispersive than SMFs; however by changing the width and height of the waveguides or the cladding material, dispersion could be reduced. Through simulations, we observed that using ridge waveguides rather than rib waveguides provides more flexible dispersion tailoring. For example, we simulated that an SOI, SiO_2 cladding ridge waveguide with 220 nm height and 540 nm width would have zero group velocity dispersion at 1310 nm. Although rib waveguides have higher losses than ridge waveguides, their loss could be reduced to 0.45 dB/cm by using higher resolution lithography [125].

The return loss of individual components in a photonic integrated circuit for OCT is also crucial. The return loss of fiber components which are connected to each other with fibers much longer than the coherence length of the light source does not present a significant problem. However, the distances between individual components in a photonic integrated chip are in the order of the coherence length of OCT light sources. Thus, fringes resulting from reflections within the chip may appear as spurious background signals in the OCT signal. To avoid this, the transition between different photonic integrated components needs to be sufficiently smooth to reduce such reflection effects.

For Fourier-domain OCT implementation, currently silicon is more appropriate for SS-OCT than spectral domain OCT. Further technological improvements are necessary to demonstrate silicon spectrometers with specifications necessary for OCT ($\geq$ 512 channels, $\leq$ 0.2 nm resolution). While the first step toward an on-chip SS-OCT is to optimize the passive structures, in the long term, integration with active components will open new application opportunities. Wafer-scale integration of germanium photodetectors on silicon has recently been demonstrated [136]. An interferometer design similar to the one presented in this study can be integrated

with such on-chip photodetectors and used for balanced SS-OCT. Integrating the photodetectors will also eliminate the chip-to-fiber losses for the light sent to the photodetectors. Integration of a tunable laser and other active elements (e.g., optical amplifier, modulator) can be pursued by bonding prefabricated components on top of the passive structures or by bonding the active material epitaxial layers on top of the passive waveguides and then processing the active components [126].

Considering state-of-the-art silicon photonic components, including integrated photodetectors, an integrated interferometer for SS-OCT with sensitivity close to fiber interferometers could be realized. The major loss (for light returning from the sample) will be the 3 dB loss at coupler C2, as broadband integrated circulators have not matured yet. Additional 1-2 dB loss at the chip to collimating lens interface and 0.5 dB propagation loss could be present.

B.4 Conclusion

In conclusion, we have fabricated and characterized a silicon-based, integrated photonics interferometer for swept-source OCT. We have demonstrated cross-sectional imaging of a layered tissue phantom showing the feasibility and potential of integrated silicon-based OCT systems. Thanks to the small size of the silicon photonic integrated components, silicon photonics can become a platform for highly parallel OCT systems. Monolithic/hybrid integration of active components with passive structures can enable an on-chip OCT system at low cost and small form factor.

APPENDIX C

Chip based common-path optical coherence tomography system with an on-chip microlens

Abstract

We demonstrate an integrated optical probe including an on-chip microlens for a common-path swept-source optical coherence tomography system. This common-path design uses the end facet of the silicon oxynitride waveguide as the reference plane, thus eliminating the need of a space-consuming and dispersive on-chip loop reference arm, thereby obviating the need for dispersion compensation. The on-chip micro-ball lens eliminates the need of external optical elements for coupling the light between the chip and the sample. The use of this lens leads to a signal enhancement up to 37 dB compared to the chip without a lens. The light source, the common-path arm and the detector are connected by a symmetric Y junction having a wavelength independent splitting ratio (50/50) over a much larger bandwidth than can be obtained with a directional coupler. The signal-to-noise ratio of the system was measured to be 71 dB with 2.6 mW of power on a mirror sample at a distance of 0.3 mm from the waveguide end facet. Cross-sectional OCT images of a layered optical phantom sample are demonstrated with our system.

This chapter has been published in:

- L. Chang, N. Weiss, T.G. van Leeuwen, M. Pollnau, R.M. de Ridder, K. Wörhoff, V. Subramaniam, and J.S. Kanger, "Chip based common-path optical coherence tomography system with an on-chip microlens and multi-reference suppression algorithm," Opt. Express **24**, 12635-12650 (2016).

C.1 Introduction

Optical coherence tomography (OCT) [1] is an optical imaging technique which provides three-dimensional images with micrometer-resolution. OCT imaging of biological tissue has many clinical applications [137, 138]. More recently, OCT has also been increasingly used in industrial applications [139, 140, 141, 142, 143]. The state-of-the-art OCT systems are based on Fourier-domain OCT (FD-OCT) [144], which provides a sensitivity advantage over time-domain OCT (TD-OCT) [115]. FD-OCT is performed as either spectral-domain OCT (SD-OCT) with a broad-band light source and a spectrometer or swept-source OCT (SS-OCT) with a narrow-bandwidth frequency-swept light source [137]. FD-OCT systems provide a one-dimensional depth image (known as an A-scan) with a Fourier transform of the measured spectrum. The cross-sectional images (known as B-scans) are commonly measured by scanning the beam over the sample (such as using a galvanometer scanner) [144]. Currently, most of the OCT systems are based on discrete free-space optical components and fibers. The development in integrated optical circuit technology provides the opportunity to develop chip-based OCT systems having the potential for considerable size and cost reduction. Recently, several chip-based FD-OCT systems have been demonstrated. Akca *et al.* demonstrated a SD-OCT system with a 2×2 splitter and an integrated spectrometer based on silicon oxynitride (SiON) waveguides where the reference arm was not integrated on the chip [122]. Nguyen *et al.* demonstrated a SS-OCT system with a Si_3N_4 waveguide based interferometer and reference arm [79]. Nguyen *et al.* also demonstrated focusing with chip based Fizeau OCT, similar to the work performed here [112]. Yurtsever *et al.* demonstrated two different OCT systems [124, 145]. Both systems have a sufficiently long on-chip reference arm to accommodate a galvanometer scanner in the sample arm to obtain B-scans.

In systems with an on-chip reference arm, the dispersion difference between the reference arm and the sample path needs to be compensated using methods that may reduce the attainable axial resolution [145]. The on-chip reference arm has also relatively large dimensions in many OCT chips, especially in low-contrast waveguide technology where the minimum bending radius is the limiting factor for miniaturization. Another common practical challenge in chip based systems is the design and fabrication of a broad-bandwidth 50/50 coupler to be used in the interferometer, see e.g. [146]. Directional couplers are wavelength-dependent devices of which the coupling ratio is strongly dependent on fabrication accuracy, as reported in [79]. Both deficiencies decrease the efficiency of the OCT system. In all of these chip-based OCT studies, external lenses are needed for the optical chip-to-sample coupling. These external elements can be much larger than the chip itself.

In this study we demonstrate a chip-based common-path SS-OCT system that addresses the problems of current designs. Firstly, by using a common-path OCT system we avoid the need of a separate reference arm. Some advantages of common-path OCT compared to dual-arm OCT are a greater ease of alignment, a smaller sensitivity to vibration and a better stability. These have been demonstrated in several free-space-based or fiber-based OCT systems [147, 148, 149, 150]. On our chip we exploit the back reflection from the end facet of the waveguide to act as

the reference, thus obviating the need for a separate reference arm. This leads to a significantly smaller footprint of each OCT system which could be interesting for chip-based parallel OCT. This solution not only saves space on the chip, but also eliminates the decrease of axial resolution caused by dispersion [145]. Secondly, the three ports (the light source, the detector, and the common-path arm) of the chip are connected by a symmetric Y junction. Such junctions are intrinsically wavelength independent and their design and fabrication are less critical than for a directional coupler. Thirdly, a directly integrated micro ball lens [151] is positioned at a short distance from the waveguide facet for efficient coupling of the light between the chip and the sample. This micro-ball lens is the key component enabling the common-path configuration. The lens significantly reduces the divergence angle of the light exiting from the waveguide, thus improving the lateral resolution and the chip-sample coupling compared to the case without a lens. Our SS-OCT has a maximum optical depth range of 5.1 mm (measured from the end facet of the waveguide, limited by the laser source and detector-determined spectrum resolution), of which the lens occupies only the first 0.2 mm, thereby leaving sufficient room for the sample.

The introduction of a lens causes additional reflections at the lens surface, which act as additional parasitic reference planes that reduce the image quality. This artifact has also been observed in a fiber-based common-path OCT system with a 500 μm diameter ball lens [150]. We demonstrate the recovery of the image quality by using a deconvolution algorithm which is more generally applicable to other OCT systems suffering from the effects of multiple reference planes.

C.2 Experimental set-up

The key components of the integrated optical circuit are a Y junction (200 μm long, 7 μm wide) and a polymer micro-ball lens (100 μm in diameter). The circuit was fabricated on a silicon substrate with SiON waveguide technology which was developed in the Integrated Optical MicroSystems group at the University of Twente [152]. The waveguide core is a 600 nm thick, 2 μm wide SiON channel embedded in a SiO_2 layer. The refractive index of the SiON and SiO_2 parts are 1.55 and 1.45, respectively, at $\lambda = 1300$ nm. The integration of the polymer micro-ball lens with the SiON waveguide chip is based on photolithography and thermal reflow of a photoresist polymer [151].

The schematic layout of the SS-OCT system is shown in Fig. C.1(a). Light emitted from the swept laser (Axsun Technologies, USA, 1312 nm center wavelength, 92 nm optical bandwidth, 20.9 mW output power, 50 kHz repetition rate) travels through an optical isolator (OI) and is coupled to the chip through a fiber array unit (FAU) with a 250 μm pitch. The splitting ratio of the Y junction has been measured to be between 48/52 and 52/48 in the wavelength range of 1170 nm to 1650 nm by a separate setup. The wavelength range is limited at the short wavelength side by the waveguide becoming multi-modal and at the long wavelength side by the available InGaAs detector. The in-coupled light propagates through the Y junction with approximately 50% efficiency. The waveguide end facet, which back-reflects part of the light, acts as a reference plane as shown in Figs. C.1(b) and Fig. C.1(c). Due to the etching process, this facet is angled at 86 degrees (θ) with respect to

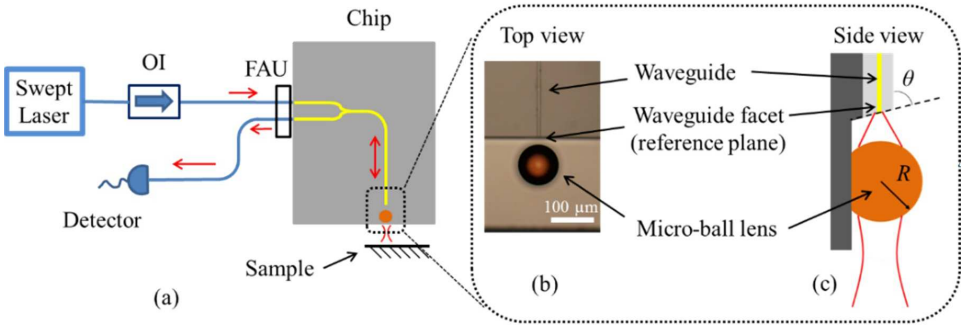

Figure C.1: Schematic of the SS-OCT experimental setup. (a) Light emitted by the swept laser source travels through an optical isolator (OI) and a fiber array unit (FAU) to the chip. The blue lines indicate optical fibers and the yellow lines represent the waveguides on the chip. (b) Microscope image of the end part of the chip showing the channel waveguide and the micro-ball lens. (c) Schematic of the side view of the structure in (b). The end facet is angled at 86 degrees (θ) with respect to the Si substrate plane.

the substrate plane, as shown in Fig. C.1(c). Thus, only 60% (simulated with a beam propagation method [153]) of the Fresnel-reflected light (3.5%) couples to a guided waveguide mode, resulting in a calculated effective power reflection of 2%, which was experimentally verified. The light that is transmitted through the facet travels through the lens onto the sample. For the experiments reported here, we chose a micro-ball-lens arrangement (65 ± 0.5 μm facet-to-lens-center distance, lens radius of 49 ± 0.5 μm) providing the best possible collimated beam (1.6 degrees half divergence angle, 15.3 μm beam waist at 0.3 mm optical path length, corresponding to an expected FWHM lateral resolution of 18 μm, 29 μm, 57 μm and 150 μm at 0.3 mm, 1 mm, 2 mm, and 5 mm optical path length, respectively) that has been reported in our earlier paper [151] (the beam divergence experiments, in an earlier paper, are repeated at a wavelength of 1.3 μm). Part of the light back reflected from the sample is coupled into the waveguide through the lens and interferes with the light that is reflected by the end facet. This interference signal propagates through the Y junction where 50% enters into the detection branch. The output signal from the chip is coupled to a detector (Thorlabs PDB 450C, USA; only one port of this balanced photodetector is used) through the same FAU. More details about the used light source and detector configurations can be found in Ref. [59]. OCT images are generated by scanning the sample in front of the chip with a linear translation stage (Zaber T-LS28-M).

C.3 Results and discussion

As the presence of the integrated lens has been shown to provide a considerable reduction of beam divergence [151], a substantial increase of the OCT signal is expected. This improvement is quantitatively demonstrated in Sec. C.3.1. In Sec. C.3.2 we show cross-sectional images of an optical phantom sample, which were obtained

	Reflected reference power P_R (μW)	Reflected sample power P_S (μW)	Power incident on the sample P_I (mW)
Without micro-ball lens	12.0 ± 0.5	2.8 ± 0.5	2.9 ± 0.1
With micro-ball lens	14.5 ± 0.5	$(2.9 \pm 0.1)10^2$	2.6 ± 0.1

Table C.1: Measured reflected reference power, reflected sample power and power incident on the sample with and without a micro-ball lens. The mirror was placed at 100 μm from the waveguide facet.

with our integrated probe. Some ghost images were noticed which are caused by closely spaced (less than the coherence length of a spectral channel) multiple reference reflections from the waveguide end facet and the lens surface. A deconvolution based method is demonstrated that largely removes these ghost images. The mathematical details of this method, which is based on a model of a multiple reference Fourier-domain OCT system is described in Ref. [154].

C.3.1 Signal enhancement with a micro-ball lens

The optical power levels were measured at several positions in the optical setup without and with a microlens (Table C.1). These optical power levels are important to quantitatively understand the signal enhancement realized with the micro-ball lens. The laser power (9 ± 0.2 mW before coupling to the chip) was the same for all measurements in Table C.1. A mirror sample was located as close as possible to the chip, which is approximately 0.1 mm distance, resulting in 0.3 mm and 0.1 mm optical path length from the sample to the waveguide facet in the case with and without a lens, respectively. The reflected reference power P_R and reflected sample power P_S were both measured at the detector location as shown in Fig. C.1(a). The power incident on the sample P_I is measured by placing a power meter at the position of the mirror sample. The signal-to-noise ratio of the system was measured to be 71 dB with 2.6 mW of power on a mirror sample at a distance of 0.3 mm from the waveguide end facet.

The results in Table C.1 show that P_R and P_I are similar in both systems. The slightly larger P_R and slightly smaller P_I in the situation with a micro-ball lens are due to reflections from the surfaces of the lens. Despite the larger optical path length between sample and waveguide facet P_S is approximately 100 times larger when compared to the case without the lens. P_R and P_I are kept the same as in Table C.1 for all the OCT measurements with the chip system in this study. P_S decreases rapidly in case of no lens, such that it cannot be measured directly (with the current setup) at larger optical path lengths but can only be calculated from the OCT measurements.

In order to study the OCT signal enhancement with the lens, the A-scan results of a mirror sample measured with and without the lens are shown in Fig. C.2(a). A peak is clearly visible at a position that corresponds to the optical path length difference between the mirror sample and the end-facet of the waveguide. For this measurement, the sample has been located at approximately 0.33 mm and 0.36 mm

from the waveguide facet in the respective cases with and without lens; the small offset was introduced to distinguish both peaks in the same graph. This means that in the case without the lens P_S at the sample is different from the value listed in Table C.1. The signal peak magnitude as measured for the chip with the micro-ball lens is a factor of 28 larger than the one measured without a lens.

The OCT signal roll-off (measured as the peak magnitude in the A-scan as a function of optical path length) with and without a micro-ball lens is compared in Fig. C.2(b). For these measurements the mirror sample was positioned at different distances from the waveguide facet, with the same light source and detector settings in all cases. The presence of the micro ball lens enhances the signal strength by up to 37 dB depending on the optical path length. In the same Figure, the calculated expected signal roll-off is presented, following Eq. (2) in Ref. [155]. For comparison, the calculated signal is normalized to the largest signal measured with a micro-ball lens. The calculated signal roll-off is based on the finite spectral resolution of the system, assuming a constant chip-sample coupling efficiency over the whole optical path length range. The values used in this calculation are 5.1 mm maximum optical path length and the ratio 0.73 of the spectral resolution to the sampling interval which is approximated by the detector duty cycle (0.73).

From Fig. C.2(b) it follows that the micro-ball lens extends the 6 dB roll-off range from 0.2 ± 0.1 mm to 1.7 ± 0.1 mm. This 6 dB roll-off range is commonly used as a characteristic parameter to indicate the signal decreasing speed of an OCT system. Since we could not measure the sample signal at exactly zero optical path length in our common-path configuration, the 6 dB signal roll-off is referred to the closest point (first point) measured in each system. The faster signal roll-off in the experiment, compared to the calculated one (which assumes a hypothetical 0 degree divergence beam), is most likely caused by the decrease of the chip sample coupling efficiency due to the beam divergence.

C.3.2 Multiple reference planes and phantom imaging

Close inspection of Fig. C.2(a) shows the appearance of relatively strong shoulders on the main peak for the case when the micro-ball lens is used. This is caused by Fresnel reflections that take place, not only at the end facet of the waveguide (the intended reference plane), but also from the front and back surfaces of the micro-ball lens. These lens surfaces, therefore, act as two additional reference planes in this common-path OCT system. Next, we will demonstrate that by using a deconvolution technique the artifacts in the A-scan caused by the lens can be eliminated. We model the measured signal as:

$$i(z) = G * H_{\mathrm{PSF}} \ , \tag{C.1}$$

where $*$ denotes convolution and G and H_{PSF} denote the sample reflectivity and the point spread function (PSF) of the OCT system in the axial direction, respectively [156]. The PSF is composed of the coherence gate depending on the source bandwidth and center wavelength, and a function describing the dependence on the reflectivities and relative positions of the (multiple) reference planes. This PSF can be characterized by measuring the response of a mirror. In case of a multiple references like in our chip system, this PSF is a multi-peak function resulting in ghost images for every additional reference plane that may overlap with the image that

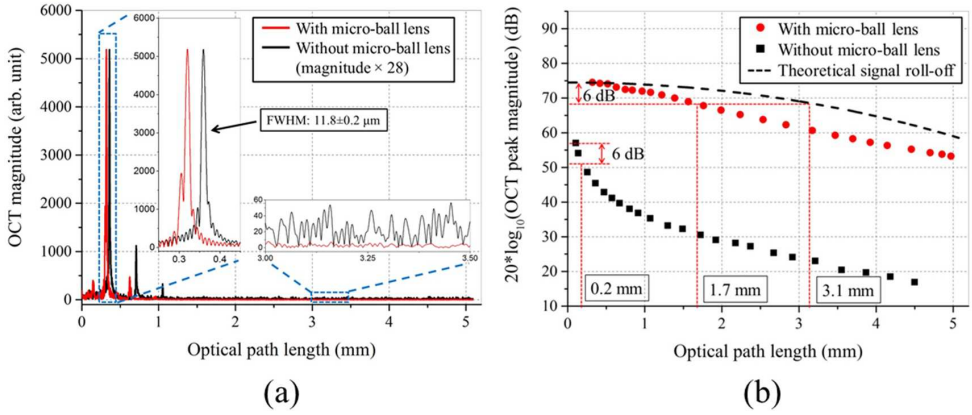

Figure C.2: Characterization of the chip-based OCT system. (a) A-scan results of a mirror sample measured with and without a micro-ball lens. The signal measured without the lens is multiplied by 28 to obtain equal peak magnitude for the cases with and without lens to enable easy comparison. The insets show a zoom in to the main signal peak and the noise floor, respectively. (b) Signal roll-off measured with and without a micro-ball lens. The peak position of each A-scan is marked with a red dot for the case with a lens and a black square for the case without lens. The peak magnitude is given in dB units, where 0 dB corresponds to the value 1 of the arbitrary units used in (a). The dashed black curve is a calculated signal roll-off based on the finite spectral resolution of the system. The red dashed lines indicate the 6 dB roll-off optical path length for each curve.

originates from the primary reference plane. A commonly used imaging processing technique, deconvolution, can be used to suppress or remove these unwanted ghost images [156].

Here, we investigate the applicability of the deconvolution technique for suppressing the ghost images. To this end, the PSF of our chip system is measured with a mirror sample, since G is a delta function in this case. A zoomed-in view of an A-scan result of a mirror sample is shown by the black curve in Fig. C.3(a), which is the PSF of our system. The effect of the two additional references is clearly visible as two additional peaks (peak 2 and 3) in Fig. C.3(a). The peaks numbered 1, 2, and 3 in Fig. C.3(a) are the interference of the mirror-waveguide-facet, mirror-lens-surface (close to the waveguide) and mirror-lens-surface (far from the waveguide), respectively. Next, this PSF is used in the deconvolution of A-scans from any sample measured with this chip system. An example of a deconvolution result is shown by the red curve in Fig. C.3(a) which shows a strong suppression of the peaks caused by reflections from the lens' surfaces.

In theory, the measurement of H_{PSF} is not sensitive to the position of the mirror sample with respect to the reference planes. Several PSF measurements using different mirror position have been performed and no significant differences were observed in the results.

Finally, we apply our OCT system to image an optical phantom. The optical phantom that is used consists of three scattering layers separated by two transparent layers. The scattering layer is silicone elastomer-based which includes scattering by

adding TiO_2 [90]. This layered sample is placed on a glass slide which is mounted on a translation stage to obtain cross-sectional OCT images. Two zoomed-in cross-sectional imagines are shown in Fig. C.3(b) and Fig. C.3(c). Each A-scan in the cross-sectional image is averaged over 30 measurements. The image after deconvolution shows a clear improvement in the contrast. This is due to the suppression of the ghost images of the scattering layers.

The full range of a deconvolved cross-sectional image is shown in Fig. C.3(d). All three scattering layers of the optical phantom can be clearly seen. The image in Fig. C.3(e) is a deconvolved cross-sectional image of the phantom measured at a larger distance from the chip. The image of the phantom becomes dimmer with increasing optical path length. Scattering layers are still clearly visible at an optical path length of 2.6 mm. Scattering (the glass holder and the sample were placed under angle to avoid specular reflection) from the rear side of the glass holder is even visible up to 4.2 mm.

Many different deconvolution algorithms exist for image processing. The deconvolution result may be different depending on the noise in the measurement and the algorithm used [157]. Since the described experiment is intended as a proof of concept that the artifacts arising from the multiple reference planes can be suppressed with a deconvolution approach, we did not perform a systematic study of different deconvolution algorithms. A further study on the selection of the deconvolution algorithms may be needed to find the optimal algorithm for this particular system.

The cross-sectional images demonstrated here were obtained by translating the sample with a mechanical stage. Since the micro-ball lens is integrated and the optical chip is a small low-mass device, an alternative implementation might mount the fiber-connected chip directly on a scanner to obtain two- or three-dimensional images.

C.4 Conclusions and outlook

In this study, we have demonstrated a chip-based common-path SS-OCT system with an integrated micro-ball lens. The common-path design eliminates the space-consuming and dispersive on-chip loop reference arm. Therefore, no dispersion compensation is needed to achieve the light-source-limited axial resolution. The three-port configuration (light source, common-path arm, and detector) enables the use of a wavelength-independent 50/50 Y junction which is much less sensitive to fabrication errors compared to a directional coupler. The drawbacks of this common-path configuration is that it cannot use a balanced detector, which leads to around 3-4 dB lower sensitivity compared to a traditional dual-arm OCT [150]. The use of an on-chip micro-ball lens eliminates the need for external optical elements for coupling the light between the chip and the sample. Such a micro-ball lens enables a very short distance of a few hundred µm between the sample and the reference plane, which is an important requirement for common-path OCT. The use of this micro-ball lens leads to a signal enhancement up to 37 dB compared to the chip without a lens, for a mirror sample. Multiple ghost images caused by additional reference planes (originating from the lens surface) could be largely suppressed using a decon-

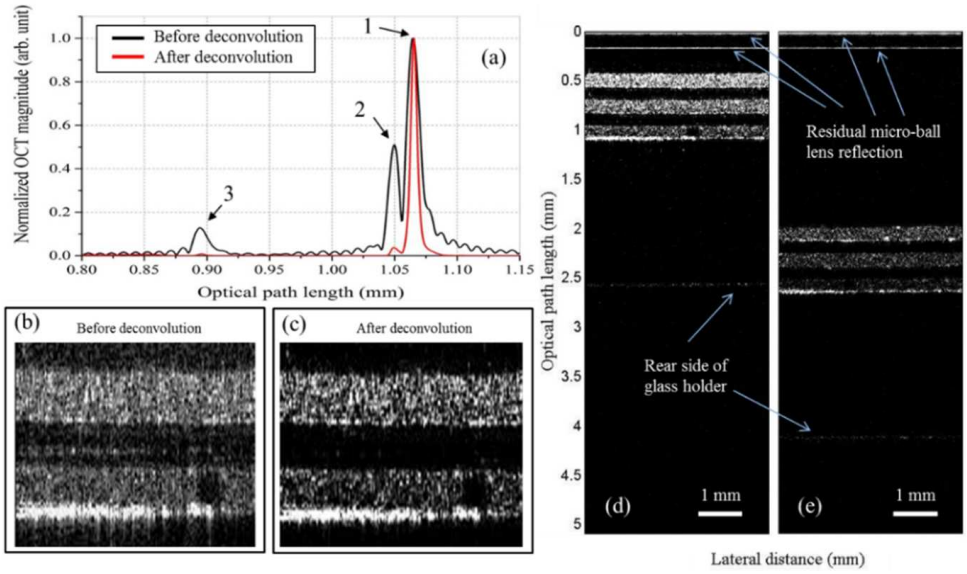

Figure C.3: (a) A zoomed-in view of an A-scan result of a mirror sample. This plot shows the effect of multiple references on a mirror sample (black curve) and its deconvolved solution (red curve). (b) and (c) Zoomed in cross-sectional images of a phantom sample before and after deconvolution. (d) and (e) The deconvolved phantom images at different distances from the chip.

volution scheme. Finally, cross-sectional imaging of a layered optical phantom, with suppressed ghost image, has been demonstrated.

The minimum footprint of this design could, in principle, be as small as 400 μm by 100 μm, which may enable the fabrication of a chip-based parallel OCT system with multiple independent detection channels. The minimum length of 400 μm is determined from the 200 μm long Y junction plus the 100 μm diameter micro-ball lens, plus some spacing. (However, in order to facilitate testing of the device, our prototype was equipped with several cm long straight access waveguides.) The minimum width of 100 μm is determined from the diameter of the lens.

We believe that, by integrating a micro-ball lens onto the chip and using a common-path configuration, we have moved a significant step forward in the development of on-chip SS-OCT systems.

Bibliography

1. D. Huang, E. A. Swanson, C. P. Lin, J. S. Schuman, W. G. Stinson, W. Chang, M. R. Hee, T. Flotte, K. Gregory, C. A. Puliafito, and J. G. Fujimoto, "Optical Coherence Tomography," Science **254**, 1178–1181 (1991).
2. J. F. de Boer, B. Cense, B. H. Park, M. C. Pierce, G. J. Tearney, and B. E. Bouma, "Improved signal-to-noise ratio in spectral-domain compared with time-domain optical coherence tomography," Opt. Lett. **28**, 2067–2069 (2003).
3. R. Leitgeb, C. K. Hitzenberger, and A. F. Fercher, "Performance of Fourier domain vs. time domain optical coherence tomography," Opt. Express **11**, 889–894 (2003).
4. W. Drexler, U. Morgner, R. K. Ghanta, F. X. Kärtner, J. S. Schuman, and J. G. Fujimoto, "Ultrahigh-resolution ophthalmic optical coherence tomography," Nature Med. **7**, 502–507 (2001).
5. G. J. Tearney, M. E. Brezinski, B. E. Bouma, M. R. Hee, J. F. Southern, and J. G. Fujimoto, "Determination of the refractive index of highly scattering human tissue by optical coherence tomography," Opt. Lett. **20**, 2258–2260 (1995).
6. J. F. de Boer, T. E. Miller, M. J. C. van Gemert, and J. S. Nelson, "Two-dimensional birefringence imaging in biological tissue by polarization-sensitive optical coherence tomography," Opt. Lett. **22**, 934–936 (1997).
7. D. J. Faber, M. C. G. Aalders, E. G. Mik, B. A. Hooper, M. J. C. van Gemert, and T. G. van Leeuwen, "Oxygen saturation-dependent absorption and scattering of blood," Phys. Rev. Lett. **93**, 028102 (2004).
8. V. M. Kodach, D. J. Faber, J. van Marle, T. G. van Leeuwen, and J. Kalkman, "Determination of the scattering anisotropy with optical coherence tomography," Opt. Express **19**, 6131–6140 (2011).
9. A. Mariampillai, B. A. Standish, E. H. Moriyama, M. Khurana, N. R. Munce, M. K. K. Leung, J. Jiang, A. Cable, B. C. Wilson, I. A. Vitkin, and V. X. D. Yang, "Speckle variance detection of microvasculature using swept-source optical coherence tomography," Opt. Lett. **33**, 1530–1532 (2008).
10. J. Kalkman, R. Sprik, and T. G. van Leeuwen, "Path-length-resolved diffusive particle dynamics in spectral-domain optical coherence tomography," Phys. Rev. Lett. **105**, 198302 (2010).
11. R. A. Leitgeb, L. Schmetterer, W. Drexler, A. F. Fercher, R. J. Zawadzki, and T. Bajraszewski, "Real-time assessment of retinal blood flow with ultrafast acquisition by color Doppler Fourier domain optical coherence tomography," Opt. Express **11**, 3116–3121 (2003).
12. B. J. Vakoc, R. M. Lanning, J. A. Tyrell, T. P. Padera, L. A. Bartlett, T. Stylianopoulos, L. L. Munn, G. J. Tearney, D. Fukumura, R. K. Jain, and B. E. Bouma, "Three-dimensional microscopy of the tumor microenvironment

in-vivo using optical frequency domain imaging," Nature Med. **15**, 1219–1223 (2009).

13. E. D. Moore and R. R. McLeod, "Phase-sensitive swept-source interferometry for absolute ranging with application to measurements of group refractive index and thickness," Opt. Express **19**, 8117–8126 (2011).
14. Z. Chen, T. E. Milner, D. Dave, and J. S. Nelson, "Optical Doppler tomographic imaging of fluid flow velocity in highly scattering media," Opt. Lett. **22**, 64–66 (1997).
15. B. R. White, M. C. Pierce, N. Nassif, B. Cense, B. H. Park, G. J. Tearney, B. E. Bouma, T. C. Chen, and J. F. de Boer, "In *vivo* dynamic human retinal blood flow imaging using ultra-high-speed spectral domain optical Doppler tomography," Opt. Express **11**, 3490–3497 (2003).
16. U. Kiencke and H. Jäkel, *Signale und Systeme* (Oldenburg, 2005).
17. B. J. Berne and R. Pecora, *Dynamic Light Scattering: With Applications to Chemistry, Biology, and Physics* (Dover Publications, 2000).
18. A. Günther and K. F. Jensen, "Multiphase microfluidics: from flow characteristics to chemical and materials synthesis," Lab Chip **6**, 1487–1503 (2006).
19. P. LeDuc, C. Haber, G. Bao, and D. Wirtz, "Dynamics of individual flexible polymers in a shear flow," Nature **399**, 564–566 (1999).
20. P. Stoodley, D. de Beer, and Z. Lewandowski, "Liquid flow in biofilm systems," Appl. and Environ. Microb. **60**, 2711–2716 (1994).
21. A. S. Popel and P. C. Johnson, "Microcirculation and hemorheology," Annu. Rev. Fluid Mech. **37**, 43–69 (2005).
22. X. Grandchamp, G. Coupier, A. Srivastav, C. Minetti, and T. Podgorski, "Lift and down-gradient shear-induced diffusion in red blood cells suspensions," Phys. Rev. Lett. **110**, 108101 (2013).
23. M. B. Lawrence and T. A. Springer, "Leukocytes roll on a selectin at physiologic flow rates: distinction from and prerequisite for adhesion through integrins," Cell **65**, 859–873 (1991).
24. Y. Yeh and H. Z. Cummins, "Localized fluid flow measurements with an HeNe Laser spectrometer," Appl. Phys. Lett. **4**, 176–178 (1964).
25. J. Ohtsubo and T. Asakura, "Velocity measurement of a diffuse object by using time-varying speckles," Opt. Quant. Electron. **8**, 523–529 (1976).
26. R. J. Adrian, "Particle-imaging techniques for experimental fluid mechanics," Annu. Rev. Fluid Mech. **23**, 261–304 (1991).
27. R. K. Chhetri, K. A. Kozek, A. C. Johnston-Peck, J. B. Tracy, and A. L. Oldenburg, "Imaging three-dimensional rotational diffusion of plasmon resonant gold nanorods using polarization-sensitive optical coherence tomography," Phys. Rev. E **83**, 040903(R) (2011).
28. M. D. Kulkarni, T. G. van Leeuwen, S. Yazdanfar, and J. A. Izatt, "Velocity-estimation accuracy and frame-rate limitations in color Doppler optical coherence tomography," Opt. Lett. **23**, 1057–1059 (1998).
29. J. Kalkman, A. V. Bykov, D. J. Faber, and T. G. van Leeuwen, "Multiple and dependent scattering effects in Doppler optical coherence tomography," Opt. Express **18**, 3883–3892 (2010).

30. H. Ren, K. M. Brecke, Z. Ding, Y. Zhao, J. S. Nelson, and Z. Chen, "Imaging and quantifying transverse flow velocity with the Doppler bandwidth in a phase-resolved functional optical coherence tomography," Opt. Lett. **27**, 409–411 (2002).
31. D. Piao, L. L. Otis, and Q. Zhu, "Doppler angle and flow velocity mapping by combined Doppler shift and Doppler bandwidth measurements in optical Doppler tomography," Opt. Lett. **28**, 1120–1122 (2003).
32. S. G. Proskurin, Y. He, and R. K. Wang, "Determination of flow velocity vector based on Doppler shift and spectrum broadening with optical coherence tomography," Opt. Lett. **28**, 1227–1229 (2003).
33. D. P. Davé and T. E. Milner, "Doppler-angle measurement in highly scattering media," Opt. Lett. **25**, 1523–1525 (2000).
34. Y. Wang and R. Wang, "Autocorrelation optical coherence tomography for mapping transverse particle-flow velocity," Opt. Lett. **35**, 3538–3540 (2010).
35. R. Michaely, A. H. Bachmann, M. L. Villiger, C. Blatter, T. Lasser, and R. A. Leitgeb, "Vectorial reconstruction of retinal blood flow in three dimensions measured with high resolution resonant Doppler Fourier domain optical coherence tomography," J. Biomed. Opt. **12**, 041213 (2007).
36. J. Lee, W. Wu, J. Y. Jiang, B. Zhu, and D. A. Boas, "Dynamic light scattering optical coherence tomography," Opt. Express **20**, 22262–22277 (2012).
37. S. H. Yun, G. J. Tearney, J. F. de Boer, and B. E. Bouma, "Motion artifacts in optical coherence tomography with frequency-domain ranging," Opt. Express **12**, 2977–2998 (2004).
38. M. Gu, C. J. R. Sheppard, and X. Gan, "Image formation in a fiber-optical confocal scanning microscope," J. Opt. Soc. Am. A **8**, 1755–1761 (1991).
39. D. P. Chowdhury, C. M. Sorensen, T. W. Taylor, J. F. Merklin, and T. W. Leste, "Application of photon correlation spectroscopy to flowing Brownian motion systems," Appl. Opt. **23**, 4149–4154 (1984).
40. R. V. Edwards, J. C. Angus, M. J. French, and J. W. Dunning Jr., "Spectral analysis of the signal from the laser Doppler Flowmeter: time independent systems," J. Appl. Phys. **42**, 837–850 (1971).
41. C. S. Johnson Jr. and D. A. Gabriel, *Laser Light Scattering* (Dover Publications, 1981).
42. H. C. Hendargo, R. P. McNabb, A. Dhalla, N. Shepherd, and J. A. Izatt, "Doppler velocity detection limitations in spectrometer-based versus swept-source optical coherence tomography," Biomed. Opt. Express **2**, 2175–2188 (2011).
43. K. K. Bizheva, A. M. Siegel, and D. A. Boas, "Path-length-resolved dynamic light scattering in highly scattering random media: The transition to diffusing wave spectroscopy," Phys. Rev. E **58**, 7664–7667 (1998).
44. M. A. Choma, A. K. Ellerbee, S. Yazdanfar, and J. A. Izatt, "Doppler flow imaging of cytoplasmic streaming using spectral domain phase microscopy," J. Biomed. Opt. **11**, 024014 (2006).
45. T. W. Taylor and C. M. Sorensen, "Gaussian beam effects on the photon correlation spectrum from a flowing Brownian motion system," Appl. Opt. **25**, 2421–2426 (1986).

46. Y. Xia and P. T. Callaghan, "Study of shear thinning in high polymer solution using dynamic NMR microscopy," Macromolecules **24**, 4777–4786 (1991).
47. G. Popescu, A. Dogariu, and R. Rajagopalan, "Spatially resolved microrheology using localized coherence volumes," Phys. Rev. E **65**, 041504 (2002).
48. H. Orihara and Y. Takikawa, "Brownian motion in shear flow: Direct observation of anomalous diffusion," Phys. Rev. E **84**, 061120 (2011).
49. S. D. Gertz and W. C. Roberts, "Hemodynamic shear force in rupture of coronary arterial atherosclerotic plaques," Am. J. Cardiol. **66**, 1368 (1990).
50. C. Joo, C. L. Evans, T. Stepinac, T. Hasan, and J. F. de Boer, "Diffusive and directional intracellular dynamics measured by field-based dynamic light scattering," Opt. Express **18**, 2858–2871 (2010).
51. K. Drescher, Y. Shen, B. L. Bassler, and H. A. Stone, "Biofilm streamers cause catastrophic disruption of flow with consequences for environmental and medical systems," Proc. Natl. Acad. Sci. U.S.A. **110**, 4345–4350 (2013).
52. J. Lee, H. Radharishnan, W. Wu, A. Daneshmand, M. Climov, C. Ayata, and D. A. Boas, "Quantitative imaging of cerebral blood flow velocity and intracellular motility using dynamic light scattering–optical coherence tomography," J. Cereb. Blood Flow Metab. **33**, 819–825 (2013).
53. R. Weber, R. Rambau, G. Schweiger, and K. Lucas, "Analysis of a flowing aerosol by correlation spectroscopy: concentration, aperture, velocity and particle size effects," J. Aerosol Sci. **24**, 485–499 (1993).
54. D. Di Carlo, D. Irimia, R. G. Tompkins, and M. Toner, "Continuous inertial focusing, ordering, and separation of particles in microchannels," Proc. Natl. Acad. Sci. U.S.A. **104**, 18892–18897 (2007).
55. K. Ishii, T. Iwai, and H. Xia, "Hydrodynamic measurement of Brownian particles at a liquid-solid interface by low-coherence dynamic light scattering," Opt. Express **18**, 7390–7396 (2010).
56. V. K. Srinivasan, H. Radhakrishnan, E. H. Lo, E. T. Mandeville, J. Y. Jiang, S. Barry, and A. E. Cable, "OCT methods for capillary velocimetry," Biomed. Opt. Express **3**, 612–629 (2012).
57. B. K. Huang and M. A. Choma, "Resolving directional ambiguity in dynamic light scattering-based transverse motion velocimetry in optical coherence tomography," Opt. Lett. **39**, 521–524 (2014).
58. N. Uribe-Patarroyo, M. Villiger, and B. E. Bouma, "Quantitative technique for robust and noise-tolerant speed measurements based on speckle decorrelation in optical coherence tomography," Opt. Express **22**, 24411–24429 (2014).
59. N. Weiss, T. G. van Leeuwen, and J. Kalkman, "Localized measurement of longitudinal and transverse flow velocities in colloidal suspensions using optical coherence tomography," Phys. Rev. E **88**, 042312 (2013).
60. F. A. W. Coumans, E. van der Pol, A. N. Böing, N. Hajji, A. Struk, T. G. van Leeuwen, and R. Nieuwland, "Reproducible extracellular vesicle size and concentration determination with tunable resistive pulse sensing," J. Extracell. Vesicles **3**, 25922 (2014).
61. A. Arnaud, W. M. Hubbard, G. D. Mandeville, B. de la Clavière, E. A. Franke, and J. M. Franke, "Technique for fast measurement of Gaussian laser beam parameters," Appl. Opt. **10**, 2775–2776 (1971).

62. D. A. Ross, "Focused laser beam effects in optical particle sizing by dynamic light scattering," Appl. Opt. **30**, 4882–4888 (1991).
63. A. J. Pine, D. A. Weitz, P. M. Chaikin, and E. Herbolzheimer, "Diffusing-Wave spectroscopy," Phys. Rev. Lett. **60**, 1134–1137 (1988).
64. R. M. Donlan and J. W. Costerton, "Biofilms: Survival mechanisms of clinically relevant microorganisms," Clin. Microbiol. Rev. **15**, 167–193 (2002).
65. M. Toyofuku, T. Inaba, T. Kiyokawa, N. Obana, Y. Yawata, and N. Nomura, "Environmental factors that shape biofilm formation," Biosci. Biotech. Biochem. **80**, 7–12 (2016).
66. J. W. Costerton, P. S. Stewart, and E. P. Greenberg, "Bacterial biofilms: a common cause of persistent infections," Science **284**, 1318–1321 (1999).
67. E. van der Wende, W. G. Characklis, and D. B. Smith, "Biofilms and bacterial drinking water quality," Water Res. **23**, 1313–1322 (1989).
68. L. Hall-Stoodley, J. W. Costerton, and P. Stoodley, "Bacterial biofilms: from the natural environment to infectious diseases," Nature **2**, 95–108 (2004).
69. Z. Lewandowski, S. A. Altobelli, and E. Fukushima, "NMR and microelectrode studies of hydrodynamics and kinetics in biofilms," Biotechnol. Progr. **9**, 40–45 (1993).
70. C. Xi, D. Marks, S. Schlachter, W. Luo, and S. A. Boppart, "High-resolution three-dimensional imaging of biofilm development using optical coherence tomography," J. Biomed. Opt. **11**, 034001 (2006).
71. T. G. van Leeuwen, M. D. Kulkarni, S. Yazdanfar, A. M. Rollins, and J. A. Izatt, "High-flow and shear-rate imaging by use of color Doppler optical coherence tomography," Opt. Lett. **24**, 1584–1586 (1999).
72. C. Dreszer, A. D. Wexler, S. Drusová, T. Overdijk, A. Zwijnenburg, H. C. Flemming, J. C. Kruithof, and J. S. Vrouwenvelder, "*In-situ* biofilm characterization in membrane systems using Optical Coherence Tomography: Formation, structure, detachment and impact of flux change," Water Res. **67**, 243–254 (2014).
73. E. Akhondi, B. Wu, S. Sun, B. Marxer, W. Lim, J. Gu, L. Liu, M. Burkhardt, D. McDougald, W. Pronk, and A. G. Fane, "Gravity-driven membrane filtration as pretreatment for seawater reverse osmosis: Linking biofouling layer morphology with flux stabilization," Water Res. **70**, 158–173 (2015).
74. S. West, M. Wagner, C. Engelke, and H. Horn, "Optical coherence tomography for the *in situ* three-dimensional visualization and quantification of feed spacer channel fouling in reverse osmosis membrane modules," J. Membrane Sci. **498**, 345–352 (2016).
75. Y. Wibisono, W. Yandi, M. Golabi, R. Nugraha, E. . R. Cornelissen, A. J. B. Kemperman, T. Ederth, and K. Nijmeijer, "Hydrogel-coated feed spacers in two-phase flow cleaning in spiral wound membrane elements: A novel platform for eco-friendly biofouling mitigation," Water Res. **71**, 171–186 (2015).
76. C. Li, S. Felz, M. Wagner, S. Lackner, and H. Horn, "Investigating biofilm structure developing on carriers from lab-scale moving bed biofilm reactors based on light microscopy and optical coherence tomography," Bioresource Technol. **200**, 128–136 (2016).

77. F. Blauert, H. Horn, and M. Wagner, "Time-resolved biofilm deformation measurements using optical coherence tomography," Biotechnol. Bioeng. **112**, 1893–1905 (2015).
78. A. E. Heidari, S. Moghaddam, K. K. Troung, L. Chou, C. Genberg, M. Brenner, and Z. Chen, "Visualizing biofilm formation in endotracheal tubes using endoscopic three-dimensional optical coherence tomography," J. Biomed. Opt. **20**, 126010 (2015).
79. C. T. Nguyen, W. Jung, J. Kim, E. J. Chaney, M. Novak, C. N. Stewart, and S. A. Boppart, "Noninvasive in vivo optical detection of biofilm in the human middle ear," Proc. Natl. Acad. Sci. U.S.A. **109**, 9529–9534 (2012).
80. C. Haisch and R. Niessner, "Visualisation of transient processes in biofilms by optical coherence tomography," Water Res. **41**, 1467–2472 (2007).
81. K. Rasmussen, C. Reilly, Y. Li, and R. S. Jones, "Real-time imaging of antibiofilm effects using CP-OCT," Biotechnol. Bioeng. **113**, 198–205 (2016).
82. M. Wagner, D. Taherzadeh, C. Haisch, and H. Horn, "Investigation of the mesoscale structure and volumetric features of biofilms using optical coherence tomography," Biotechnol. Bioeng. **107**, 844–853 (2010).
83. J. S. Vrouwenvelder, F. Beyer, K. Dahmani, N. Hasan, G. Galjaard, J. C. Kruithof, and M. C. Van Loosdrecht, "Phosphate limitation to control biofouling," Water Res. **44**, 3454–3466 (2010).
84. N. Weiss, T. G. van Leeuwen, and J. Kalkman, "Simultaneous and localized measurement of diffusion and flow using optical coherence tomography," Opt. Express **23**, 3448–3459 (2015).
85. I. Banerjee, R. C. Pangule, and R. S. Kane, "Antifouling coatings: recent developments in the design of surfaces that prevent fouling by proteins, bacteria, and marine organisms," Adv. Matter **23**, 690–718 (2011).
86. F. Meng, G. H. M. Engbers, and J. Feijen, "Polyethylene glycol-grafted polystyrene particles," J. Biomed. Mater. Res. A **70A**, 49–58 (2004).
87. C. Li, M. Wagner, S. Lackner, and H. Horn, "Assessing the influence of biofilm surface roughness on mass transfer by combining optical coherence tomography and two-dimensional modeling," Biotechnol. Bioeng. **113**, 989–1000 (2016).
88. A. Ahmad, S. G. Adie, E. J. Chaney, U. Sharma, and S. A. Boppart, "Cross-correlation-based image acquisition technique for manually-scanned optical coherence tomography," Opt. Express **17**, 8125–8136 (2009).
89. J. Ren, J. Wu, E. J., McDowell, and C. Yang, "Manual-scanning optical coherence tomography probe based on position tracking," Opt. Lett. **34**, 3400–3402 (2009).
90. D. M. de Bruin, R. H. Bremmer, V. M. Kodach, R. de Kinkelder, J. van Marle, T. G. van Leeuwen, and D. J. Faber, "Optical phantoms of varying geometry based on thin building blocks with controlled optical properties," J. Biomed. Opt. **15**, 025001 (2010).
91. Zaber Technologies, *Zaber T-series positioning products technical notes* (2006).
92. Y. M. Liew, R. A. McLaughlin, F. M. Wood, and D. D. Sampson, "Reduction of image artifacts in three-dimensional optical coherence tomography of skin in vivo," J. Biomed. Opt. **16**, 116018 (2011).

93. J. M. Rubin, T. A. Tuthill, and J. B. Fowlkes, "Volume flow measurement using Doppler and grey-scale decorrelation," Ultrasound Med. Biol. **27**, 101–109 (2001).
94. G. Binnig and C. F. Quate, "Atomic Force Microscope," Phys. Rev. Lett. **56**, 930–934 (1986).
95. L. P. Ghislain and W. W. Webb, "Scanning-force microscope based on an optical trap," Opt. Lett. **18**, 1678–1680 (1993).
96. A. Rohrbach, C. Tischer, D. Neumayer, E. Florin, and E. H. K. Stelzer, "Trapping and tracking a local probe with a photonic force microscope," Rev. Sci. Instrum. **75**, 2197–2210 (2004).
97. S. W. Golomb, *Radar signal patterns for combinatorial designs*, chap. 1 (Cambridge University Press, 2000).
98. J. M. Nohrden, "Spectral estimation using nonuniform sampling," Master's thesis, Massachusetts Institute of Technology (1995).
99. I. Martí-Vidal, "Optimum estimate of delays and dispersive effects in low-frequency interferometric observations," Astronom. and Astrophys. **517**, A83 (2010).
100. J. B. Shearer, "List of optimal Golomb rulers," (2016).
101. V. D. Nguyen, "Integrated-optics-based Optical Coherence Tomography," Ph.D. thesis, University of Amsterdam (2013).
102. J. Lee, J. Y. Jiang, W. Wu, F. Lesage, and D. A. Boas, "Statistical intensity variation analysis for rapid volumetric imaging of capillary network flux," Biomed. Opt. Express **5**, 1160–1172 (2014).
103. S. Sakadžić, J. Lee, D. A. Boas, and C. Ayata, "High-resolution in vivo optical imaging of stroke injury and repair," Brain Research **1623**, 174–192 (2015).
104. B. K. Huang, U. A. Gamm, V. Bhandari, M. K. Khokha, and M. A. Choma, "Three-dimensional, three-vector-component velocimetry of cilia-driven fluid flow using correlation-based approaches in optical coherence tomography," Biomed. Opt. Express **6**, 3515–3538 (2015).
105. N. Uribe-Patarroyo and B. E. Bouma, "Rotational distortion correction in endoscopic optical coherence tomography based on speckle decorrelation," Opt. Lett. **40**, 5518–5521 (2015).
106. G. L. Monroy, P. Pande, R. L. Shelton, R. M. Nolan, D. R. Spillman, R. G. Porter, M. A. Novak, and S. A. Boppart, "Non-invasive optical assessment of viscosity of middle ear effusions in otitis media," J. Biophotonics (2016).
107. L. R. De Pretto, G. E. C. Nogueira, and A. Z. Freitas, "Microfluidic volumetric flow determination using optical coherence tomography speckle: An autocorrelation approach," J. Appl. Phys. **119**(16), 163105 (2016).
108. K. C. Zhou, B. K. Huang, U. A. Gamm, V. Bhandari, M. K. Khokha, and M. A. Choma, "Particle streak velocimetry-optical coherence tomography: a novel method for multidimensional imaging of microscale fluid flows," Biomed. Opt. Express **7**, 1590–1603 (2016).
109. I. Popov and A. Vitkin, "Dynamic light scattering by flowing Brownian particles measured with optical coherence tomography: impact of the optical system," J. Biomed. Opt. **21**, 017002–017002 (2016).

110. N. Uribe-Patarroyo and B. E. Bouma, "Velocity gradients in spatially resolved laser Doppler flowmetry and dynamic light scattering with confocal and coherence gating," Phys. Rev. E **94**, 022604 (2016).
111. D. D. Culemann, A. Knuettel, and E. Voges, "Integrated optical sensor in glass for optical coherence tomography," IEEE J. Sel. Topics Quantum Electron. **6**, 730–734 (2000).
112. V. D. Nguyen, N. Ismail, F. Sun, K. Wörhoff, T. G. van Leeuwen, and J. Kalkman, "SiON integrated optics elliptic couplers for Fizeau-based optical coherence tomography," J. Lightwave Technol. **28**, 2836–2842 (2010).
113. V. D. Nguyen, B. I. Akca, K. Wörhoff, R. M. de Ridder, M. Pollnau, T. G. van Leeuwen, and J. Kalkman, "Spectral domain optical coherence tomography imaging with an integrated optics spectrometer," Opt. Lett. **36**, 1293–1295 (2011).
114. B. I. Akca, V. D. Nguyen, J. Kalkman, N. Ismail, G. Sengo, F. Sun, A. Driessen, T. G. van Leeuwen, M. Pollnau, K. Wörhoff, and R. M. de Ridder, "Toward spectral-domain optical coherence tomography on a chip," IEEE J. Sel. Topics Quantum Electron. **18**, 1223–1233 (2012).
115. M. A. Choma, M. V. Sarunic, C. Yang, and J. A. Izatt, "Sensitivity advantage of swept source and Fourier domain optical coherence tomography," Opt. Express **11**, 2183–2189 (2003).
116. G. Yurtsever, K. Komorowska, and R. Baets, "Low dispersion integrated Michelson interferometer on Silicon on insulator for optical coherence tomography," in *Proc. SPIE*, vol. 8091, p. 80910T (2011).
117. J. F. Bauters, M. J. Heck, D. John, D. Dai, M. C. Tien, J. S. Barton, A. Leinse, R. G. Heideman, D. J. Blumenthal, and J. E. Bowers, "Ultra-low-loss high-aspect-ratio Si_3N_4 waveguides," Opt. Express **19**, 3163–3174 (2011).
118. A. Kohlhaas, C. Fromchen, and E. Brinkmeyer, "High-resolution OCDR for testing integrated-optical waveguides: dispersion-corrupted experimental data corrected by a numerical algorithm," J. Lightwave Technol. **9**, 1493–1502 (1991).
119. N. Sugimoto, T. Shintaku, A. Tate, H. Terui, M. Shimokozono, E. Kubota, M. Ishii, and Y. Inoue, "Waveguide polarization independent optical circulator," IEEE Photon. Technol. Lett. **11**, 355–357 (1999).
120. Y. Chen, D. M. de Bruin, C. Kerbage, and J. F. de Boer, "Spectrally balanced detection for optical frequency domain imaging," Opt. Express **15**, 16390–16399 (2007).
121. A. Takagi, K. Jinguji, and M. Kawachi, "Design and fabrication of broad-band silica-based optical waveguide couplers with asymmetric structure," IEEE J. Quant. Electron. **28**, 848–855 (1992).
122. B. I. Akca, B. Považay, A. Alex, K. Wörhoff, R. M. de Ridder, W. Drexler, and M. Pollnau, "Miniature spectrometer and beam splitter for an optical coherence tomography on a silicon chip," Opt. Express **21**, 16684–16656 (2013).
123. V. D. Nguyen, N. Weiss, W. Beeker, M. Hoekman, A. Leinse, R. G. Heideman, T. G. van Leeuwen, and J. Kalkman, "Integrated-optics-based swept-source optical coherence tomography," Opt. Lett. **37**, 4820–4822 (2012).

124. G. Yurtsever, B. Považay, A. Alex, B. Zabihian, W. Drexler, and R. Baets, "Photonic integrated Mach-Zehnder interferometer with an on-chip reference arm for optical coherence tomography," Biomed. Opt. Express **5**, 1050–1061 (2014).
125. S. K. Selvaraja, P. De Heyn, G. Winroth, P. Ong, G. Lepage, C. Cailler, A. Rigny, K. Bourdelle, W. Bogaerts, D. Van Thourhout, J. Van Campenhout, and P. Absil, "Highly uniform and low-loss passive silicon photonics devices using a 300 mm CMOS platform," in *Optical Fiber Communication Conference*, p. Th2A.33 (2014).
126. H. Park, M. N. Sysak, H. W. Chen, A. W. Fang, D. Liang, L. Liao, B. R. Koch, J. Bovington, Y. Tang, K. Wong, M. Jacob-Mitos, R. Jones, and J. E. Bowers, "Device and integration technology for silicon photonic transmitters," IEEE J. Sel. Top. Quantum Electron. **17**, 671–688 (2011).
127. J. S. Orcutt, B. Moss, C. Sun, J. Leu, M. Georgas, J. Shainline, E. Zgraggen, H. Li, J. Sun, M. Weaver, S. Urošević, R. J. R. M. Popović, and V. Stojanović, "Open foundry platform for high-performance electronic-photonic integration," Opt. Express **20**, 12222–12232 (2012).
128. D. Vermeulen, Y. De Koninck, Y. Li, E. Lambert, W. Bogaerts, R. Baets, and G. Roelkens, "Reflectionless grating couplers for Silicon-on-Insulator photonic integrated circuits," Opt. Express **20**, 22278–22283 (2012).
129. H. Yun, W. Shi, Y. Wang, L. Chrostowski, and N. A. F. Jaeger, "2×2 adiabatic 3-dB coupler on Silicon-on-Insulator rib waveguides," in *Proc. SPIE*, vol. 8915, p. 89150V (2013).
130. M. R. Watts, J. Sun, C. DeRose, D. C. Trotter, R. W. Young, and G. N. Nielson, "Adiabatic thermo-optic Mach-Zehnder switch," Opt. Lett. **38**, 733–735 (2013).
131. M. Wojtkowski, V. Srinivasan, T. Ko, J. Fujimoto, A. Kowalczyk, and J. Duker, "Ultrahigh-resolution, high-speed, Fourier domain optical coherence tomography and methods for dispersion compensation," Opt. Express **12**, 2404–2422 (2004).
132. T. Bajraszewski, M. Wojtkowski, M. Szkulmowski, A. Szkulmowska, R. Huber, and A. Kowalczyk, "Improved spectral optical coherence tomography using optical frequency comb," Opt. Express **16**, 4163–4176 (2008).
133. D. Vermeulen, S. Selvaraja, P. Verheyen, G. Lepage, W. Bogaerts, P. Absil, D. Van Thourhout, and G. Roelkens, "High-efficiency fiber-to-chip grating couplers realized using an advanced CMOS-compatible Silicon-On-Insulator platform," Opt. Express **18**, 18278–18283 (2010).
134. B. Ben Bakir, A. V. de Gyves, R. Orobtchouk, P. Lyan, C. Porzier, A. Roman, and J. M. Fedeli, "Low-loss (1 dB) and polarization-insensitive edge fiber couplers fabricated on 200-mm Silicon-on-Insulator wafers," IEEE Photon. Technol. Lett. **22**, 739–741 (2010).
135. K. Shiraishi, H. Yoda, and C. S. Tsai, "A two-port polarization-insensitive coupler module between single-mode fiber and silicon-wire waveguide," Opt. Express **20**, 24370–24375 (2012).
136. S. Assefa, F. Xia, W. Green, C. Schow, A. Rylyakov, and Y. Vlasov, "CMOS-integrated optical receivers for on-chip interconnects," IEEE J. Sel. Top. Quantum Electron. **16**, 1376–1385 (2010).

137. W. Drexler and J. G. Fujimoto, *Optical Coherence Tomography: Technology and Applications* (Springer-Verlag, 2008).
138. M. Wojtkowski, "High-speed optical coherence tomography: basics and applications," Appl. Opt. **49**, D30–D61 (2010).
139. M. Dufour, G. Lamouche, B. Gauthier, C. Padioleau, and J. P. Monchalin, "Inspection of hard-to-reach industrial parts using small-diameter probes," in *Proc. SPIE*, vol. 6343, p. 63431Z (2006).
140. G. Song and K. Harding, "OCT for industrial applications," in *Proc. SPIE*, vol. 8563, p. 8563N (2012).
141. W. J. Walecki, K. Lai, A. Pravdivtsev, V. Souchkov, P. Van, T. Azfar, T. Wong, S. H. Lau, , and A. Koo, "Low-coherence interferometric absolute distance gauge for study of MEMS structures," in *Proc. SPIE*, vol. 5716, pp. 182–188 (2005).
142. W. J. Walecki, K. Lai, V. Souchkov, P. Van, S. H. Lau, and A. Koo, "Novel noncontact thickness metrology for backend manufacturing of wide bandgap light emitting devices," Phys. Status Solidi (C) **2**, 984–989 (2005).
143. D. Stifter, "Beyond biomedicine: a review of alternative applications and developments for optical coherence tomography," Appl. Phys. B **88**, 337–357 (2007).
144. A. F. Fercher, "Optical coherence tomography - development, principles, applications," Z. Med. Phys. **20**, 251–276 (2010).
145. G. Yurtsever, N. Weiss, J. Kalkman, T. G. van Leeuwen, and R. Baets, "Ultracompact silicon photonic integrated interferometer for swept-source optical coherence tomography," Opt. Lett. **39**, 5228–5231 (2014).
146. B. I. Akca, C. R. Doerr, G. Sengo, K. Wörhoff, M. Pollnau, and R. M. de Ridder, "Broad-spectral-range synchronized flat-top arrayed-waveguide grating applied in a 225-channel cascaded spectrometer," Opt. Express **20**, 18313–18318 (2012).
147. Y. Huang, K. Zhang, J. U. Kang, D. Calogero, R. H. James, and I. K. Ilev, "Noncontact common-path Fourier domain optical coherence tomography method for in vitro intraocular lens power measurement," J. Biomed. Opt. **16**, 126005 (2011).
148. U. Sharma, N. M. Fried, and J. U. Kang, "All-fiber common-path optical coherence tomography: sensitivity optimization and system analysis," IEEE J. Sel. Top. Quantum Electron. **11**, 799–805 (2005).
149. A. B. Vakhtin, D. J. Kane, W. R. Wood, and K. A. Peterson, "Common-path interferometer for frequency-domain optical coherence tomography," Appl. Opt. **42**, 6953–6958 (2003).
150. M. Zhao, Y. Huang, and J. U. Kang, "Sapphire ball lens-based fiber probe for common-path optical coherence tomography and its applications in corneal and retinal imaging," Opt. Lett. **37**, 4835–4837 (2012).
151. L. Chang, M. Dijkstra, N. Ismail, M. Pollnau, R. M. de Ridder, K. Wörhoff, V. Subramaniam, and J. S. Kanger, "Waveguide-coupled micro-ball lens array suitable for mass fabrication," Opt. Express **23**, 22414–22423 (2015).
152. K. Wörhoff, P. V. Lambek, and A. Driessen, "Design, tolerance analysis, and fabrication of silicon oxynitride based planar optical waveguides for communication devices," J. Lightwave Technol. **17**, 1401–1407 (1999).

153. W. P. Huang and C. Xu, "Simulation of three-dimensional optical waveguides by a full-vector beam propagation method," IEEE J. Quantum Electron. **29**, 2639–2649 (1993).
154. L. Chang, N. Weiss, T. G. van Leeuwen, M. Pollnau, R. M. de Ridder, K. Wörhoff, V. Subramaniam, and J. S. Kanger, "Chip based common-path optical coherence tomography system with an on-chip microlens and multi-reference suppression algorithm," Opt. Express **24**, 12635–12650 (2016).
155. S. Yun, G. Tearney, B. Bouma, B. Park, and J. de Boer, "High-speed spectral-domain optical coherence tomography at 1.3 μm wavelength," Opt. Express **11**, 3598–3604 (2003).
156. P. J. Shaw and D. J. Rawlins, "The point-spread function of a confocal microscope - its measurement and use in deconvolution of 3-D data," J. Microsc. **163**, 151–165 (1991).
157. J. L. Starck, E. Pantin, and F. Murtagh, "Deconvolution in astronomy: a review," Publ. Astron. Soc. Pac. **114**, 1051–1069 (2002).

Summary

This thesis begins with a general introduction in Chapter 1. There, the contents of this thesis are placed in the corresponding scientific context and the reader is presented with the main analysis tool that will be used and developed in the following chapters. The main goal of this thesis is to exploit the information carried by the signal measured by optical coherence tomography (OCT) to measure directional and random motion (flow, diffusion, and displacement) of a sample.

In Chapter 2 we report on the localized measurement of the longitudinal and transverse flow velocities in a colloidal suspension using OCT. We present a model for the path-length resolved autocorrelation function including diffusion and flow, which we experimentally verify. For flow that is not perpendicular to the incident beam, the longitudinal velocity gradient over the coherence detection gate causes additional decorrelation, which is described by our model. We demonstrate simultaneous imaging of sample morphology and longitudinal and transverse flow at micrometer scale in a single measurement.

In Chapter 3 we extend the results presented in the previous chapter to measure the longitudinal and the transverse flow velocity components and the diffusion coefficient simultaneously and in a single measurement. Our results on a flowing suspension of polystyrene spheres show that the flow velocity and the diffusion coefficient can be reliably estimated in a regime determined by the sample diffusivity, the local flow velocity, and the Gaussian beam waist. We experimentally demonstrate that a smaller beam waist results in an improvement of the velocity sensitivity at the expense of the precision and accuracy of the estimation of the diffusion coefficient. Further, we show that the decay of the OCT autocorrelation function due to flow depends only on the Gaussian beam waist irrespective of the sample position with respect to the focus position.

In Chapter 4 we apply the knowledge and results developed in the previous two chapters to the measurement of biofilm growth and local hydrodynamics in a microfluidic channel. Specifically, we measure independently with high spatio-temporal resolution the longitudinal flow velocity component parallel to the imaging beam and the transverse flow velocity component perpendicular to the imaging beam. Based on the measured velocities we calculate the shear-rates in the flow channel. We show the relation between the measured biofilm structure and flow velocities as biofilm growth progresses over the course of 48 hours.

In Chapter 5 we treat the issue of non-uniform lateral scanning of the probe beam in OCT. In the previous chapters we have generated two-dimensional images of a sample by scanning the probe beam using a galvanometric mirror. In that case, the lateral scan range is limited to a few millimeters. However, for certain applications, such as in dermatology, a lateral scan range in that order is not sufficient. This limitation can be lifted by scanning the OCT imaging beam by hand. By do-

ing so, the non-uniform scan velocity characteristic of hand-held scanning produces imaging artifacts and leads to a morphologically inaccurate representation of the sample. Here, we demonstrate a solution to this problem which is based on the Doppler shift carried by phase of the OCT signal. Furthermore, we demonstrate the feasibility of Doppler flow velocity measurements in underlying flow channels while laterally scanning the imaging probe with arbitrary and varying velocity. Finally, we performed centimeters-long hand-held two-dimensional imaging of skin *in-vivo*.

In Chapter 6 we report on a method to measure the height profile of non-scattering soft (biological) samples in liquid environments using a combination of optical tweezers and OCT. We measure the displacement of an optically trapped probe using OCT to quantify the height profile of a sample with nanometer resolution. The method is validated by measuring the height profile of a silicone mold of a diffraction grating with a well defined height profile. As an application example for profilometry of soft non-scattering samples we measured the height profile of a smooth muscle mouse aorta fixed cell.

In Chapter 7 we present the general conclusion from the experiments reported in this thesis and in Chapter 8 we make recommendations for future research directions.

In Appendices A-C we present three different approaches to reduce the form-factor of an OCT system based on integrated-optics. We designed, fabricated, and characterized an integrated-optics-based swept-source optical coherence tomography (SS-OCT) system in TriPleX, silicon, and silicon oxynitride technologies. An external 1300 nm swept source is coupled to the chip, which contains waveguide structures for interferometric path-length ranging. In all three technologies, we demonstrate cross-sectional OCT imaging of a multilayered tissue phantom.

Samenvatting

Dit proefschrift begint met een algemene introductie in hoofdstuk 1, waarin de inhoud van dit proefschrift geplaatst wordt in zijn wetenschappelijke context. Daarnaast wordt het belangrijkste analysemiddel geïntroduceerd, welke wordt ontwikkeld en gebruikt in de daaropvolgende hoofdstukken. Het hoofddoel van dit proefschrift is om de informatie te exploiteren die in het signaal, gemeten met optische coherentie tomografie (OCT), zit en om daarmee gerichte en willekeurige bewegingen (stroomsnelheid, diffusie, en verplaatsing) van deeltjes in een vloeistof te kwantificeren.

In hoofdstuk 2 demonstreren we gelokaliseerde metingen met OCT van de longitudinale en transversale stroomsnelheden van een colloïdale suspensie. We presenteren en valideren een model voor de padlengteopgeloste autocorrelatie functie. Ons model laat zien dat, in het geval van stromingen die niet loodrecht op de invallende bundel staan, de longitudinale snelheidsgradiënt oorzaak is van extra decorrelatie. We demonstreren gelijktijdige beeldvorming van het stromingskanaal en kwantificeren de longitudinale en transversale stroomsnelheden, alle op micrometerschaal en verkregen uit één meting.

In hoofdstuk 3 breiden we de resultaten van het vorige hoofdstuk uit, waarbij we zowel de longitudinale en de transversale stroomsnelheden als de diffusie coëfficiënt gelijktijdig uit één meting bepalen. Onze metingen op een stromende suspensie van polystyreen bolletjes laten zien dat de stroomsnelheid en de diffusie coëfficiënt betrouwbaar gemeten kunnen worden in een regime bepaald door de diffusiviteit, de lokale stroomsnelheid, en de Gaussische bundelbreedte. We tonen experimenteel aan dat bij gebruik van een kleinere bundelbreedte de snelheidsgevoeligheid verbetert ten koste van de precisie en nauwkeurigheid van de meting van de diffusie coëfficiënt. Verder laten we zien dat het tijdsverval van de OCT-autocorrelatie functie veroorzaakt door de stroomsnelheid alleen afhankelijk is van de Gaussiche bundelbreedte ongeacht de positie van het sample ten opzichte van de positie van het focus.

In hoofdstuk 4 passen we de kennis en de resultaten ontwikkeld in de vorige twee hoofdstukken toe om de groei van biofilms en de lokale hydrodynamica in microfluïdische kanalen te meten. Specifiek meten we, onafhankelijk van elkaar en met hoge tijd en ruimtelijke resolutie, de longitudinale en transversale stroomsnelheiden en structuur van de biofilm. Gebaseerd op de gemeten snelheden berekenen we de afschuifsnelheden in het stromingskanaal. We laten de relatie zien tussen de gemeten biofilm-structuur en de stroomsnelheid tijdens de groei van de biofilm gedurende 48 uur.

In hoofdstuk 5 behandelen we de ongelijkmatige beweging van een met de hand bewogen OCT-sonde. In de vorige hoofdstukken hebben we twee dimensionale OCT-beelden van een sample gegenereerd met behulp van galvanometrische spiegels. In dat geval is de laterale omvang van een OCT-scan beperkt tot enkele millimeters. Echter, voor sommige toepassingen, zoals in de dermatologie, is een scanlengte van

deze orde van grootte niet voldoende. Deze beperking kan worden opgeheven door een OCT-sonde met de hand te scannen over het sample. Als gevolg van de ongelijkmatige handbeweging ontstaat door deze beeldacquisitie wel snelheidsvariaties die beeldvormingsartefacten geven. Deze variaties resulteren in een onscherp beeld van het sample. In dit hoofdstuk demonstreren we een oplossing voor dit probleem die gebaseerd is op de Doppler verschuiving, welke gemeten wordt met de fase van het OCT-signaal. Verder, demonstreren we een tweedimensionale handmatig gemaakte scan van enkele centimeters lang van de *in-vivo* huid.

In hoofdstuk 6 beschrijven we een methode gebaseerd op een combinatie van optische pincetten en OCT om het hoogte profiel van niet verstrooiende zachte (biologische) samples in vloeibare omgevingen te meten. De verplaatsing van een optisch gevangen deeltje wordt met OCT gemeten, waardoor het hoogte profiel van een sample met nanometer nauwkeurigheid gemeten kan worden. De methode is gevalideerd met metingen op een siliconen diffractierooster met een goed gedefinieerd hoogteprofiel. Als een toepassingsvoorbeeld voor de profilometrie van zachte niet verstrooiende samples meten we het hoogteprofiel van een gefixeerde aorta-spiercel van een muis.

In hoofdstuk 7 worden de algemene conclusies van de experimenten beschreven in dit proefschrift besproken. In hoofdstuk 8 maken we aanbevelingen voor toekomstige onderzoek.

In bijlagen A-C, worden drie verschillende benaderingen om de vormfactor van een OCT-systeem te reduceren, gebaseerd op geïntegreerde optica, gepresenteerd. We ontwerpen en karakteriseren OCT-systemen die op TriPleX, silicium en siliciumoxinitride technologieën zijn gebaseerd. In alle gevallen wordt een externe lichtbron van 1300 nm gekoppeld aan de chip, die golfgeleider structuren bevat voor interferometrische padlengte metingen. In alle drie technologieën demonstreren we tweedimensionale OCT-beeldvorming met een weefselfantoom met meerdere lagen.

Portfolio

Name: Nicolás Weiss
PhD period: April 2011 - June 2016
Supervisors: Prof. Dr. A.G.J.M. van Leeuwen
Dr. J. Kalkman

Training

Activity	Year	Workload (ECTS)
Courses		
Biophotonics Summer School - University of Illinois at Urbana-Champaign	2012	3
Presentation Skills Course - IOP Photonic Devices	2012	0.5
Practical Biostatistics - Academic Medical Center	2013	1.1
Scientific Writing in English for Publication - Academic Medical Center	2013	1.5
Experimental Techniques in Fluid Mechanics - J.M. Burgerscentrum	2014	5
Oral presentations		
European Conference on Biomedical Optics, Munich, Germany	2013	1.5
LaserLab Symposium, Amsterdam, The Netherlands	2013	0.5
17th International Symposium on Application of Laser Techniques to Fluid Mechanics, Lisbon, Portugal	2014	1.5
SPIE Photonics West, San Francisco, United States of America	2014-2016	4.5
SPIE Photonics Europe, Brussels, Belgium	2014 & 2016	3
Reviewing		
Optics Letters	2013-2016	2.5
Journal of Biomedical Optics	2015	0.5
Optics Express	2013	1.0
Biomedical Optics Express	2015-2016	0.5
PLOS One	2014	0.5

Teaching

Activity	Year	Workload (ECTS)
Lecturing		
Research Practicum. Physics, 2nd year	2013-2015	1.5
Supervising		
B.Sc. project of Anna Latour on "Transversal velocimetry from speckle decorrelation in optical coherence tomography"	2012	1.0
Summer internship of Aleksandra Scisly on "Blood measurements with optical coherence tomography"	2015	1.0

Author contributions

Chapter 2
N. Weiss, T. G. van Leeuwen, and J. Kalkman, "Localized measurement of longitudinal and transverse flow velocities in colloidal suspensions using optical coherence tomography," Phys. Rev. E **88**, 042312 (2013).

Conception and design:	NW, JK, TGvL
Data/literature acquisition:	NW
Data/literature acquisition and interpretation:	NW
Drafting the manuscript:	NW
Critical revision of the manuscript:	JK, TGvL
Supervision:	JK, TGvL

Chapter 3
N. Weiss, T. G. van Leeuwen, and J. Kalkman, "Simultaneous and localized measurement of diffusion and flow using optical coherence tomography," Opt. Express **23**, 3448-3459 (2015).

Conception and design:	NW
Data/literature acquisition:	NW
Data/literature acquisition and interpretation:	NW
Drafting the manuscript:	NW
Critical revision of the manuscript:	TGvL
Supervision:	JK, TGvL

Chapter 4
N. Weiss, K. El Tayeb El Obied, J. Kalkman, R.G.H. Lammertink, and T. G. van Leeuwen, "Measurement of biofilm growth and local hydrodynamics using optical coherence tomography," Biomed. Opt. Express **7**, 3508-3518 (2016).

Conception and design:	NW, KETEO
Data/literature acquisition:	NW
Data/literature acquisition and interpretation:	NW
Drafting the manuscript:	NW
Critical revision of the manuscript:	JK, TGvL, KETEO, RGHL
Supervision:	TGvL

Chapter 5
N. Weiss, T. G. van Leeuwen, and J. Kalkman, "Doppler-based lateral motion tracking for optical coherence tomography," Opt. Lett. **37**, 2220-2222 (2012).

Conception and design:	NW, JK, TGvL
Data/literature acquisition:	NW
Data/literature acquisition and interpretation:	NW
Drafting the manuscript:	NW
Critical revision of the manuscript:	JK, TGvL
Supervision:	JK, TGvL

Chapter 6
N. Weiss and T. G. van Leeuwen, "Photonic force phase imaging," *unpublished*.

Conception and design:	NW, TGvL
Data/literature acquisition:	NW
Data/literature acquisition and interpretation:	NW
Drafting the manuscript:	NW
Critical revision of the manuscript:	TGvL, JK
Supervision:	TGvL

Appendix A
V.D. Nguyen, N. Weiss, W. Beeker, M. Hoekman, A. Leinse, R.G. Heideman, T. G. van Leeuwen, and J. Kalkman, "Integrated-optics-based swept-source optical coherence tomography," Opt. Lett. **37**, 4820-4822 (2012).

Conception and design:	VDN, NW, JK, TGvL
Data/literature acquisition:	VDN, NW
Data/literature acquisition and interpretation:	VDN, NW
Drafting the manuscript:	VDN,
Critical revision of the manuscript:	JK, NW, WB, TGvL
Supervision:	JK, TGvL

Appendix B
G. Yurtsever, N. Weiss, J. Kalkman, T. G. van Leeuwen, and R Baets, "Ultra-compact silicon photonic integrated interferometer for swept-source optical coherence tomography," Opt. Lett. **39**, 5228-5231 (2014).

Conception and design:	GY, NW, TGvL, RB
Data/literature acquisition:	GY, NW
Data/literature acquisition and interpretation:	GY, NW
Drafting the manuscript:	GY
Critical revision of the manuscript:	NW, JK, RB, TGvL
Supervision:	TGvL, RB

Appendix C
L. Chang, N. Weiss, T. G. van Leeuwen, M. Pollnau, R.M. de Ridder, K. Wörhoff, V. Subramaniam, and J.S. Kanger, "Chip based common-path optical coherence tomography system with an on-chip microlens and multi-reference suppression algorithm," Opt. Express **24**, 12635-12650 (2016).

Conception and design:	LC, NW, TGvL, JSK
Data/literature acquisition:	LC, NW
Data/literature acquisition and interpretation:	LC, NW
Drafting the manuscript:	LC
Critical revision of the manuscript:	NW, TGvL, MP, RMdR, KW, VS, JSK
Supervision:	TGvL, JSK

List of publications

Publications in this thesis

- **N. Weiss**, T. G. van Leeuwen, and J. Kalkman, "Doppler-based lateral motion tracking for optical coherence tomography," Opt. Lett. **37**, 2220-2222 (2012).
- V.D. Nguyen, **N. Weiss**, W. Beeker, M. Hoekman, A. Leinse, R.G. Heideman, T. G. van Leeuwen, and J. Kalkman, "Integrated-optics-based swept-source optical coherence tomography," Opt. Lett. **37**, 4820-4822 (2012).
- **N. Weiss**, T. G. van Leeuwen, and J. Kalkman, "Localized measurement of longitudinal and transverse flow velocities in colloidal suspensions using optical coherence tomography," Phys. Rev. E **88**, 042312 (2013).
- G. Yurtsever, **N. Weiss**, J. Kalkman, T. G. van Leeuwen, and R Baets, "Ultra-compact silicon photonic integrated interferometer for swept-source optical coherence tomography," Opt. Lett. **39**, 5228-5231 (2014).
- **N. Weiss**, T. G. van Leeuwen, and J. Kalkman, "Simultaneous and localized measurement of diffusion and flow using optical coherence tomography," Opt. Express **23**, 3448-3459 (2015).
- L. Chang, **N. Weiss**, T. G. van Leeuwen, M. Pollnau, R.M. de Ridder, K. Wörhoff, V. Subramaniam, and J.S. Kanger, "Chip based common-path optical coherence

tomography system with an on-chip microlens and multi-reference suppression algorithm," Opt. Express **24**, 12635-12650 (2016).

- **N. Weiss**, K. El Tayeb El Obied, J. Kalkman, R.G.H. Lammertink, and T. G. van Leeuwen, "Measurement of biofilm growth and local hydrodynamics using optical coherence tomography," Biomed. Opt. Express **7**, 3508-3518 (2016).

Other publications

- D. Izzo, **N. Weiss**, and T. Seidl, "Constant-optic-flow lunar landing: Optimality and guidance," J. Guid. Control Dynam. **34**, 1383-1395 (2011).
- T.J.J. van den Boom, **N. Weiss**, W. Leune, R.M.P. Goverde, and B. De Schutter "A permutation-based algorithm to optimally reschedule trains in a railway traffic network", Proceedings of the 18th IFAC World Congress, Milan, Italy, 9537-9542 (2011).

Acknowledgments

All technical and scientific work is never the product of a single individual. The research work that resulted in this PhD thesis is by no means an exception. At this point, I would like to thank the current and past members of the Department of Biomedical Engineering and Physics, my fellow co-authors, and my dear family and friends for contributing directly and indirectly to my research. I would also like to thank the members of my doctorate committee for evaluating this thesis.

Nicolás Weiss
Hilversum, October 2016.

About the author

Nicolás was born on October 30, 1984 in Montevideo, Uruguay. He received the Uruguayan and German high school diplomas in 2003 at the *Deutsche Schule Montevideo* in Uruguay. From 2004 he studied Electrical Engineering and Information Technology at the Karlsruhe Institute of Technology in Karlsruhe, Germany. Before graduating as a *Diplom-Ingenieur* in 2010 he worked as an intern at the European Space Agency in Noordwijk, the Netherlands where he worked on biomimetic optic-flow computations for optimal landing strategies. In 2010, he moved to the Delft Center for Systems and Control at Delft University of Technology where he worked briefly on model-predictive control for railway traffic optimization. In 2011, he joined the Department of Biomedical Engineering and Physics at the Academic Medical Center. The research performed in this group resulted in this PhD thesis. Nicolás lives with his partner and his two daughters in Hilversum, the Netherlands. As from July 2016, he works as a Design Engineer in the YieldStar Algorithms and Physical Modeling group at ASML.